NORTHWESTERN UNIVERSITY

Chemistry on Supramolecular Nanostructures:
Peptide Amphiphiles with Non-Covalent or Covalent-Linking Functionality

A DISSERTATION

SUBMITTED TO THE GRADUATE SCHOOL
IN PARTIAL FUFILLMENT OF THE REQUIREMENTS

for the degree

DOCTOR OF PHILOSOPHY

Field Of Chemistry

by

Lorraine Hsu

EVANSTON, IL

December 2008

ABSTRACT

Chemistry on Supramolecular Nanostructures: Peptide Amphiphiles with Non-Covalent or Covalent-Linking Functionality

Lorraine Hsu

In this work several self-assembling PA systems containing covalent-linking functionalities have been investigated. These covalently linkable PAs were designed to probe the supramolecular structure by covalent capture of the nanofibers and also improve the mechanical stiffness of the gel-material. The diacetylene motif was the main functional group investigated because of its topochemical reaction and colorimetric change as a useful indicator of polymerization. The syntheses, characterization and application of diacetylene PAs are discussed in Chapter 3. These molecules were observed to successfully polymerize, turning an intense blue color suggesting there is ordering within the nanofibers, while still maintaining its nanofiber morphology. Varying PA molecules change the PDA spectroscopic signal, suggesting differences in PA packing within a nanofiber. It was possible therefore to characterize molecular packing differences within a nanofiber using the PDA as a colorimetric probe. By oscillatory rheology, gels that were polymerized showed increased stiffness. Because of their enhanced stiffness, it was possible to microfabricate for the first time patterned structures in PA-based materials, performed by Dr. Alvaro Mata.

Another photo-reactive functional group, coumarin, was chosen for its reversible chemical reaction and potential biological use as an anti-cell proliferative agent. Photoirradiation reactions of the coumarin PA system were not found to be 100% reversible regardless of where the coumarin molecule was synthetically placed on the PA. SKBr-3 breast cancer cells were

cultured in a coumarin PA-coated well to investigate the PA's potential anti-proliferative effects. Compared to free 7-hydroxycoumarin, coumarin PAs show at least a 5-fold increase in cytotoxicity compared to free coumarin.

Another chemical strategy to build larger macroassemblies from the bottom-up is to include noncovalent interactions located at the periphery of the PA nanofibers. For this purpose PAs containing the nucleobases (adenine or thymine) were synthesized without covalent-linking functionality. Nucleobase interaction was observed by CD spectroscopy including adenine–thymine base-pairing when mixing the two complementary PAs. Microscopy of the PAs as individual or mixed systems showed significant bundling of the nanofibers. These nucleobase PA systems could be developed for further applications as oligonucleotide binding agents. Nucleobase PAs were found to interact with polyadenylic acid (PolyA). Microscopy of the thymine PA and the PolyA mixture also showed bumpy fiber morphologies, suggesting that the biopolymer may be wrapping itself around the individual nanofibers.

Acknowledgements

Although a thesis represents the individual's contributions, its contents and very existence could not have been possible without the help, discussions, funding, friendships, and guidance I have received from numerous people while being a part of the Chemistry Department at Northwestern. To start, I would like to thank my advisor, Samuel I. Stupp, for giving me the opportunity to freely explore my own Ph.D. projects and always supporting them with his own ideas. I would also like to thank my thesis committee: Frederick D. Lewis and SonBinh T. Nguyen. To Professor Lewis, thank you deeply for my summer research experience and being a kind mentor during my Ph.D. candidacy. To Professor Nguyen, thanks for becoming a part of my committee last minute. I also thank Annelise E. Barron for being in my original committee.

Due to the interdisciplinary content of my research, I would like to thank my research contributors whom are experts in the fields I am not: Michelle Seitz in the Shull lab did compression testing on my materials. Dan Carvajal also in the Shull lab for running drop shape analyses on my materials. Dr. Alvaro Mata, a postdoc in the Stupp lab, made 3D micropatterns from my materials for cell studies. A number of current and past Stupp individuals also deserve thanks for discussions and tutelage: Dr. Liang-Shi Li, currently a professor at Indiana University, was the most inspirational officemate I ever had. Dr. Mustafa Guler, now an assistant professor at Bilkent University, showed me how peptide synthesis was done specifically with our peptide amphiphiles. I also thank: Dr. Albert Hung, now at IBM and still running more than any sane person should, for his work on the SASE methodology and FT–IR help; Dr. Hongzhou Jiang, currently at Western Digital, for teaching me AFM instrumentation; Stephen Soukasene for the

TEM discussions and training; Ian Tevis for re-demonstrating the SASE technique and letting us borrow your Wii; Dr. Jen Klare for providing metal coated substrates and Dr. Josh Goldberger for giving me hands-on experience regarding photolithography and clean room protocol.

Graduate school can be a frustrating environment, and having these friends whom were also active research contributors, were absolutely vital in keeping my sanity. These people will forever have my friendship and deepest gratitude. I thank: David Stone, my best friend, for always being around in whichever world I occupied- words cannot express my degree of appreciation; Chung-Yan Koh, apparently my 'other' self with eerily similar lives, for important biological contributions involving my research as well as the musical snobbery and hilarious discussions of the politically incorrect; Dr. Krista L. Niece, now at Luna Innovations, for her exemplary work on bioactive PAs and constant emails of encouragement. Dr. Liam Palmer, the for his immense help with my manuscript editing, mentoring, and guidance as well as keeping his sense of humor while putting up with our antics. My lunch crew (also including Wei-Wen Tsai, Dr. Yves Ruff, and most recently Dr. Rie Wakabayashi)- my favorite part of the day. And of course Sharon Jacknow for being a 'mother of the lab' which is in no way a trivial task- I truly appreciate everything you have done for me, your kind company, and keeping our lab functional.

For funding, I thank NSF–MRSEC for their fellowship opportunities and NIH funding. Regarding facilities usage, I thank: Keck facility and its manager Katie Favale for training and assistance; ASL, now IMSERC- especially Dr. Yuyang Wu for his NMR help; EPIC and its manager, Dr. Shuyou Li for TEM usage and assistance; NIFTI for AFM usage; Keck II and its manager, Dr. Xingqi Chen for FT–IR usage and assistance; and the IBNAM Chem Core labs for HPLC usage.

Finally I would like to thank my friends and family outside of work for making the effort to poke me once in awhile to be sure I was still alive. To my closest friends: Annie Bosler, Sarah Hoffman, Seung Yun Lee, Patricia Wu, Linda Wu- love you guys. To Amy, the best barista at the Starbucks I frequented throughout my graduate career and reliable stimulant provider- thank you for the never-ending sugar rush and friendly smile. And a large thanks to my supportive family: My mother and father, Ling and Mark C. Hsu, as dedicated, admirable individuals and parents; my sister and brother, Ann and Darren; my brother-in-law, Jason, and my new nephew, Devin. I am fortunate to have this family; of course, my thesis is dedicated to them.

List of Abbreviations

AFM	atomic force microscopy
Ala (A)	alanine
Arg (R)	arginine
Asp (D)	aspartic acid
Boc	*t*-butoxycarbonyl
CD	circular dichroism
Cys (C)	cysteine
DCM	dichloromethane
Dde	1-(4,4-dimethyl-2,6-dioxocyclohex-1-ylidene)ethyl
DIPC	diisopropylcarbodiimide
DMAP	4-dimethylaminopyridine
DMF	dimethylformamide
DMHS	dimethylhexylsilyl
DMHSCl	dimethylhexylsilyl chloride
DNA	deoxyribonucleic acid
DPTS	4-(dimethylamino)pyridinium-4-toluenesulfonate
DSP	dithiobis(succinimidyl propionate)
EDCI	1-ethyl-3-(3-dimethylaminopropyl)carbodiimide
EtOH	ethanol
Fmoc	9-fluorenylmethoxycarbonyl
Gly (G)	glycine
GPC	gel permeation chromatography
HBTU	2-(1H-benzotriazole-1-yl)-1,1,3,3-tetramethylaminium hexafluorophosphate
HMPB	4-hydroxymethyl-3-methoxyphenoxybutyric acid
hMRSC	human mesenchymal stem cell
HOBt	*N*-hydroxybenzotriazole
HPLC	high performance liquid chromatography
HPLC	high performance liquid chromatography
Ile (I)	isoleucine
IR	infrared
LDA	lithium diisopropylamine
Leu (L)	leucine
Lys (K)	lysine
MALDI	matrix-assisted laser desorption ionization
MBHA	methylbenzyhydrylamine
MeOH	methanol
$MgSO_4$	magnesium sulfate
MI	maleimide

List of Abbreviations (cont.)

MIC	Minimum inhibitory concentration
Mtt	4-methyltrityl
NaH	sodium hydroxide
NaPi	sodium phosphate
NH_4OH	ammonium hydroxide
NMR	nuclear magnetic resonance
NPA	nucleobase peptide amphiphile
OBz	*O*-benzyl
PA	peptide amphiphile
Pbf	2,2,4,6,7-pentamethyldihydro-benzofuran-5-sulfonyl
PDA	polydiacetylene
PDMS	polydimethylsiloxane
PM-IRRAS	polarization modulation-infrared reflection-adsorption spectroscopy
PNA	peptide nucleic acid
PTA	phosphotungstic acid
SASE	sonication-assisted solution embossing
SCK	shell-crosslinked knedels
Ser (S)	serine
SPPS	solid phase peptide synthesis
tBu	*t*-butyl
t-BuLi	tert-butyl lithium
TEA	triethylamine
TEM	transmission electron microscopy
TFA	trifluoroacetic acid
TFE	trifluoroethanol
THF	tetrahydrofuran
TIPS	triisopropylsilane
Trp (W)	tryptophan
Trt	trityl
Val (V)	valine
VE	vinyl ether

“Time for fun!”

To my family and mom's food

Table of Contents

List of Figures

Chapter 3	Diacetylene Peptide Amphiphiles	Page

Chapter 5	Peptide Amphiphiles with Complementary Hydrogen Bonding Motifs	Page

List of Tables

Chapter 1: Introduction and Background

1.1 Supramolecular Chemistry

Supramolecular chemistry was first described by Jehn-Marie Lehn as "chemistry beyond the molecule,"[14] which is defined as multi-molecular systems that rely on the organization of molecules through non-covalent forces.[15-17] It has become an area of great interest because of its relevance in several interdisciplinary fields such as biology, chemistry, physics, and material science as well as the interfaces between them. When addressing the bottom-up synthetic challenges chemists face, supramolecular chemistry offers additional means towards the synthesis of ordered, large scale macromolecular assemblies. Nature has been the inspiration behind many synthetic supramolecular systems and the ability to control molecular assembly has permitted the creation of new materials,[18] some of which also have stimuli-responsive properties.[19-21] Although progress has been made since the establishment of this field, many questions and challenges still remain for these complex systems regarding characterization limitations, structure control, and structure–function relationships.

1.1.1 Self-Assembly

Self-assembly is the spontaneous reorganization of molecules through non-covalent interactions to form highly-ordered supramolecular structures.[22, 23] These non-covalent interactions (Table 1.1) include hydrogen bonding,[24, 25] van der Waals, hydrophobicity,[26] Coulomb's forces, π-π stacking,[27, 28] and metal-ligand interactions.[29-31] Although these forces are individually weak, the summation of these interactions brings the overall assembled system to a lower energy state, resulting in organized supramolecular structures.[28, 32]

Table 1.1 Strength of several non-covalent forces in gas phase[4] and effective distance of non-covalent forces.

Molecular Interaction	Strength (kJ mol^{-1})	Distance
covalent bond	100 – 400	1 – 2.5 Å
metal-ligand	0 – 400	1 – 3 Å
Coulomb	< 250	difficult to assess
hydrogen bond	10 – 65	2 – 4 Å
π–π	0 – 50	3 – 4 Å
Van der Waals	< 5	difficult to assess

In nature, these interactions have evolved to yield complex, functional architectures comprised of relatively simple building blocks such as amino acids, sugars, and nucleobases. Non-covalent forces play key biological roles in structure stabilization, molecular recognition for cellular communication, and data storage. Recent findings also show a number of diseases stemming from the unwanted self-assembly of proteins such as the formation of amyloid aggregates,[33] which further emphasizes the importance of understanding correct macromolecular folding. As biological assemblies continue to be demystified using crystallographic analyses, scientists have been able to design and synthesize artificial supramolecular assemblies by strategically designing molecules that will form the predicted non-covalent interactions.

1.1.2 Nanostructures in Aqueous Conditions

A number of water soluble, natural building block derivatives have become universal for synthesizing supramolecular nanostructures. Amino acids and its derivatives are commonly used to mimic protein secondary structures such as α-helices, β-sheets, and other helical structures. For other hydrogen bonding motifs, nucleobases and various derivatives are commonly used for

complementary donor-acceptor recognition. There has been much research done on biopolymers including the synthesis of various DNA analogues, PNA being the one of the more popular derivatives due to its greater base-pairing sensitivity than DNA while still maintaining the double helix conformation.[34] Bilayer lipid surfactants have also been synthesized, typically containing a hydrophobic tail and a charged head group. These small molecules self-assemble into sandwich-like layers by exposing its charged head group to the solvent and burying the hydrophobic alkyl tails between either hydrophilic sides. From these building blocks, zero, one, and two dimensional nanostructures have been made including micelles,[35] nanofibers,[13, 36] nanotubes,[3, 37] helices,[8] tapes,[38] vesicles,[1] as well as three dimensional networks (Figure 1.1).

One of the ultimate applications for aqueous supramolecular nanostructures is to seamlessly reintroduce the material back into a biological system with the goal of reprogramming a specific process or function. The first step towards this considerably complex objective, is to understand the self-assembly process which, as Lehn eloquently addressed, can be divided into several stages: i) the molecular recognition of the individual molecules, ii) the 'growth' of the hierarchical structure, iii) equilibrium of the final assembly, and iv) the application of the assembly towards the desired target for molecular communication and future reactivity.[39] The challenges of making functional, supramolecular nanostructures equivalent to that of nature's will not occur anytime soon, but ongoing research and improving instrumentation (i.e. throughput, resolution) will continue to bring us closer towards our goal.

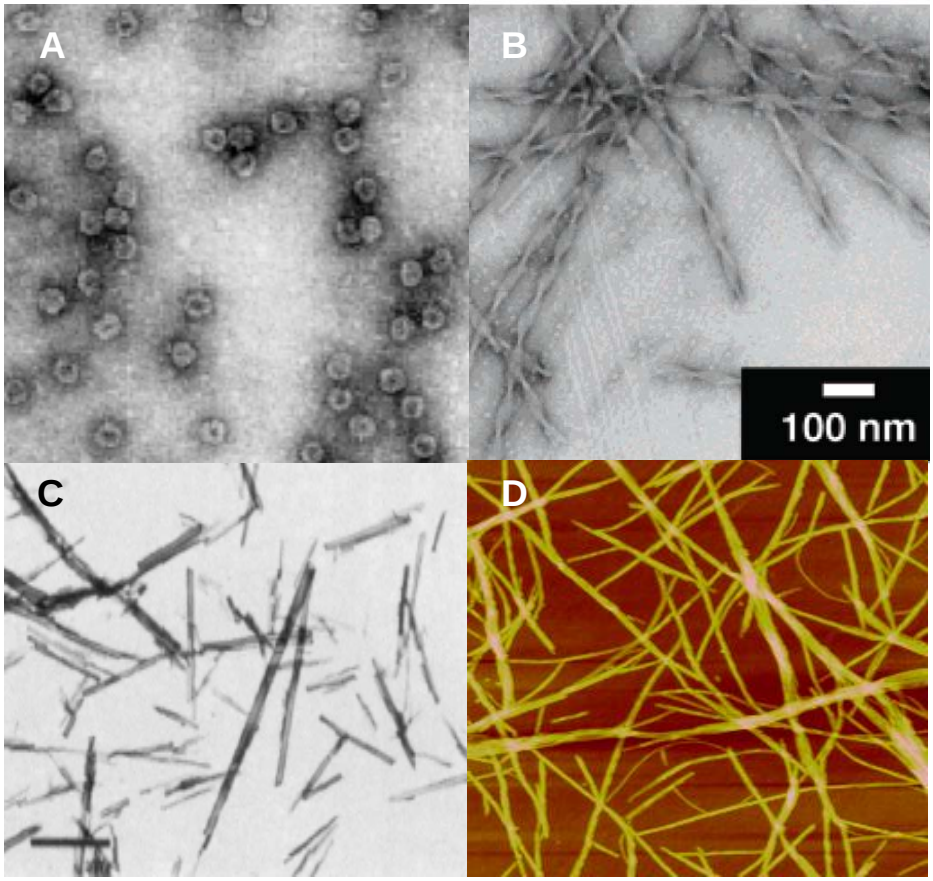

Figure 1.1. Examples of bionanostructures: **A**) vesicles[1] from a virus cage (~28 nm) **B**) helices[8] from PAs containing a lipid tail **C**) nanotubes[11] (scale bar: 1 μm) from a peptide-only amphiphile and **D**) nanofibers from PAs containing a conjugated lipid tail (5 μm image).[13]

1.2 Covalent Linking of Supramolecular Structures

Supramolecular nanostructures are dynamic systems, since they are only held together by non-covalent forces. This can make characterization and controlled organization of multi-assemblies difficult as these assemblies are sensitive and can reversibly disassemble depending on solvent, temperature, time, and concentration. As an immediate solution, some macromolecular systems have been designed to include covalent-linkages post self-assembly. By adding covalent bonds, the supramolecular system then becomes i) structurally 'trapped' and easier to characterize, ii) more robust from a materials perspective, and iii) more robust from a structural perspective as growing hierarchical architectures of increasing complexities become the new objective.

When characterizing a supramolecular structure, covalent trapping is a prevalent methodology in biology, particularly with protein structure elucidation.[40] Cysteines are commonly introduced into proteins to observe whether crosslinking occurs, providing 3D spatial information of how the protein is folded.[41] Additional structure-function studies with the crosslinked protein are also done using mutated amino acids to determine which amino acids play a role in molecular recognition of the target molecule or protein folding. Bifunctional crosslinkers,[42] such as dithiobis(succinimidyl propionate) (DSP),[43, 44] are also used to determine protein-protein associations as well as photocleavable crosslinkers.[45]

A common approach of enhancing the mechanical properties of materials includes the addition of covalent-linkers. This is common in epoxy resin formulas which involve the curing of films or adhesives. Although this procedure is more common for non-assembling systems,[46] it is also possible for supramolecular structures so long as the general self-assembled structure is

maintained.[47] It has been shown that polymerization of self-assembled polymers on a substrate will further rigidify the material.[48] Wooley et al. have demonstrated that crosslinked self-assembled micelles are able to maintain their general structure after the interior core has been degraded, forming hollow shells.[5] The main concern when polymerizing supramolecular structures is disrupting their morphology, further emphasizing the importance of choosing an appropriate linker.

In our pursuit of synthesizing large complex systems, there are currently few examples of self-assembled systems stable enough to further build upon them without introducing covalent linking functionalities. DNA has often been touted as a potential engineering material and molecular machine by utilizing base-pairing recognition to form micrometer-scale patterns. It has been suggested and shown that DNA patterns can be used as scaffolds for additional molecular recognition systems.[2] There are even fewer examples of self-assembled systems that have been

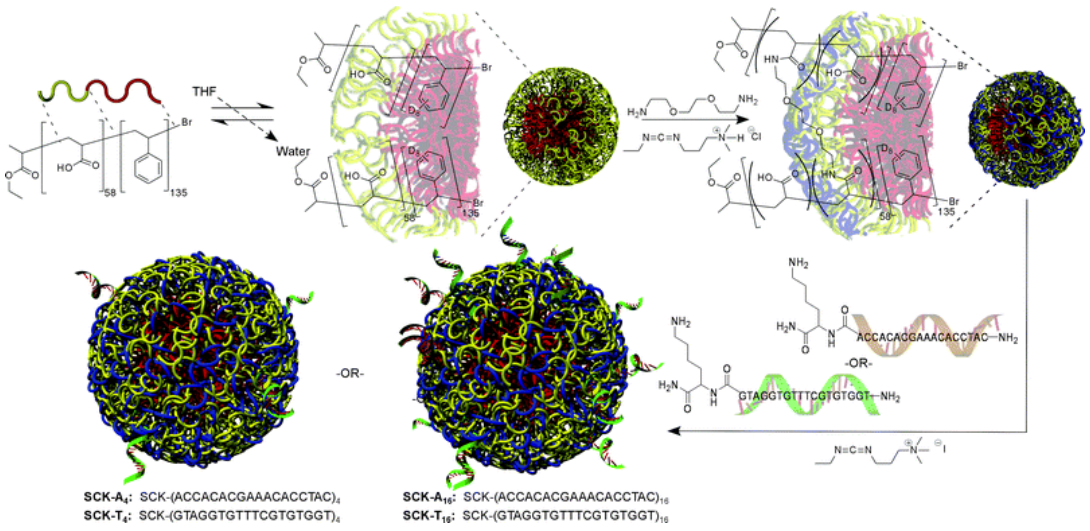

Figure 1.2. An example of self-assembled, then crosslinked systems with additional functionalization. Shown is a schematic of PNA conjugated SCK nanoparticles.[5]

crosslinked for stabilization followed by additional functionalization. Shell crosslinked knedel-like (SCK) nanoparticles functionalized with PNA single strands is an example of such a system; these nanoparticles are able to recognize its complementary counterpart, forming large aggregated structures[49, 50] (Figure 1.2). From this discussion, we hope to introduce covalent linking functional groups into our supramolecular systems needed to help elucidate the supramolecular structure as well as improve the mechanical integrity of the nanomaterial.

1.3 Complementary Hydrogen Bonding in Supramolecular Systems

Hydrogen bonding is necessary in the three dimensional structures of biological systems, providing both molecular recognition and directionality.[51] Greater selectivity between molecules can be achieved by including multiple hydrogen donor and acceptor substituents on one molecule, with DNA base pairing being the most well-known example of complementary hydrogen bonding. Adenine-thymine and guanine-cytosine base pairs are examples of double and triple hydrogen bonding motifs systems, respectively. DNA base pairs or their analogues are the most commonly adapted hydrogen bonding motifs in synthetic assemblies in order to achieve

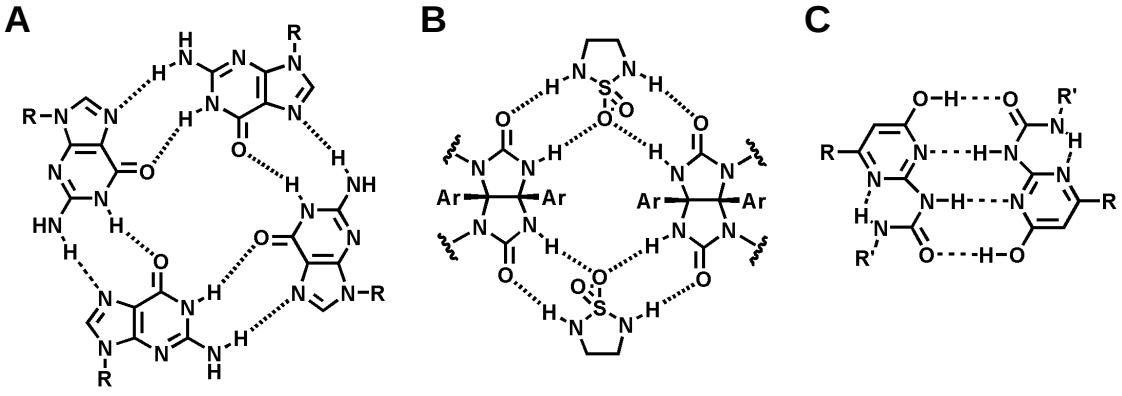

Figure 1.3. A few examples of complementary multi-hydrogen bonding systems. **A**) guanine quadruplex[2] **B**) sulfamide-urea complex[7] **C**) ureidopyrimidone dimer.[10]

a similar degree of sensitivity in molecular recognition.[10, 52] Other well-characterized complementary hydrogen bonding systems include melamine-cyanuric acid complexes,[7, 53] uriedo-pyrimidone dimers,[54] sulfamide-urea complexes,[55] amongst others (Figure 1.3).[11, 56-58] Complementary hydrogen bonding motifs will be important in the design and self-assembly of larger supramolecular materials for its sensitive molecular recognition and binding affinity.

1.4 Peptide Amphiphiles: Structure Types, Self-Assembly, and Function

Peptidic amphiphiles comprise of a large class of molecules which, by definition, contain hydrophobic and hydrophilic segments.[37, 59, 60] Under aqueous conditions, these molecules reassemble to minimize interfacial energies incompatible with molecular segments or solvent molecules. The study of self-assembling peptide-based amphiphiles can be divided into three categories being: i) peptide-only molecules, ii) peptidic block co-polymers, and iii) derivatized peptides (Figure 1.4). Peptide-only amphiphiles include cyclic peptides,[61] short cationic and anionic surfactant-like peptides,[12, 62-64] and β-sheet forming peptides.[65-67] These molecules rely on both polar and apolar amino acids to form their amphiphilic segments. The second category includes polypeptides and copolymers which are synthesized by either ring-opening polymerization or more currently, living polymerization of α-amino acid-*N*-carboxyanhydrides.[11, 67, 68] Derivatized peptides include typically peptidic molecules containing a hydrophobic addition such as single or double alkyl tail units. Depending on molecular design, all of these molecules have shown to form different architectures including spheres,[69] cylinders,[70-72] twisted cylinders,[36] among others.[9, 73]

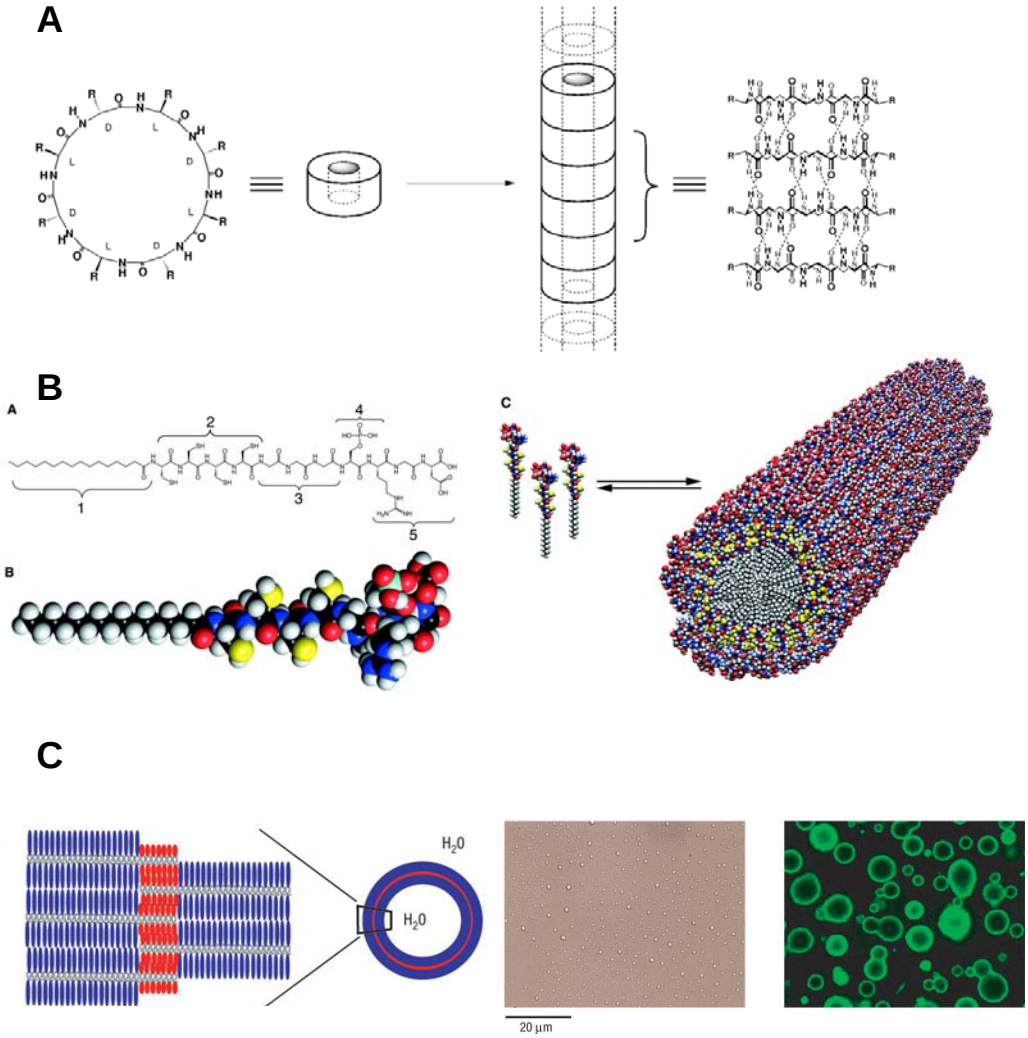

Figure 1.4. A few examples of the subclasses of peptide amphiphiles: **A**) Peptide-only amphiphile. Shown is a schematic of a nanotube assembly from *d*,*l*-peptides.[3] **B**) Derivatized peptide amphiphile containing an alkyl tail. Shown is a schematic of a nanofiber assembly.[9] **C**) Polypeptide. Shown is the self-assembly of a diblock copolypeptide.[12]

In this thesis, the focus will be on a class of derivatized peptides containing alkyl hydrophobic segments, which was discovered in our group and able to form high-aspect-ratio cylindrical nanofibers.[74] This nanostructure formation is due to the initial hydrophobic collapse followed by intramolecular β-sheet formation. At appropriate concentrations (0.1–2 wt%) and solvent conditions, these one-dimensional nanofibers can form self-supporting gels; changes in pH or screening salts help eliminate net charge repulsion in the PA molecules further favoring self-assembly.[6] Previous work by Jiang et al.[75] and Paramonov et al.[76, 77] have shown the β-sheets within the nanofiber tend to align parallel to its *z*-axis, but dynamic behavior such as PA molecules exchanging between nanofibers particularly when addressing mixed PA systems are experimentally non-trivial to probe. The general design of our peptide amphiphile (PA) structure is robust and will form cylindrical nanofibers even with changes in peptide sequence and the hydrophobic segment. This tolerance has allowed the synthesis of many PA molecules with varying bioactive epitopes and chromophores as well as different molecular architectures of the peptide[78, 79] all of which form nanofibers and self-supporting gels.

Due to the biocompatibility and biodegradability of most peptide amphiphiles, they have yielded promising applications as self-assembling materials for drug delivery, *in vivo* imagining,[78] and as bioactive scaffolds for cell signaling.[79] Peptide amphiphiles containing short bioactive epitopes such as RGDS and IKVAV, have demonstrated positive responses as bioscaffolds for cellular adhesion and the support of neuronal adhesion and outgrowth, respectively.[80] Heparin-binding PA nanofibers have also shown enhanced angiogenesis when compared to other PAs, free heparin, and control systems.[9] PAs offer the advantage of anchoring the desired epitope to the self-assembled nanofiber, so that locally high densities of the epitope

are presented in order to achieve the desired cellular response. The ongoing research in our group continues to expand the biological uses of these PA materials towards stem cell differentiation, cancer therapy, and other chronic diseases. In doing so, it is equally important to continue the structural and mechanical investigations of these self-assembled materials. The importance of these investigations will be further addressed in the subsequent chapters.

1.5 Objective and Summary of Research

As previously mentioned, supramolecular chemistry offers the potential of creating multi-system assemblies beyond zero and one dimensional structures. In this thesis, we introduce a new generation of peptide amphiphiles containing either covalent-linking groups or complementary hydrogen bonding motifs with the objectives of i) stabilizing the supramolecular nanofibers for structural characterization, ii) developing rigid self-supporting gels for bioapplications, and iii) forming higher-ordered macrostructures. Although quantitative characterization of these supramolecular constructs remains challenging, some structural insight can be gleaned from relative comparisons through indirect probing and comparisons with other similar peptide amphiphiles.

This thesis project originated from attempts to probe the internal structure of the nanofiber using a standard, non-crosslinkable peptide amphiphile eventually followed by initial attempts in synthesizing peptide amphiphiles with covalent-linking motifs as discussed in Chapter 2. Several PAs containing a tryptophan amino acid located in different regions of the PA molecule were synthesized in order to monitor its fluorescence anisotropy. The findings supported the original hypothesis that PAs of branched architectures did not pack into nanofibers

as efficiently as PAs with linear architectures. The extent of structural information obtained from the tryptophan PA system was limited and within the series, biological applications of the PAs were limited due to the fragility of the self-supporting gel. The first attempts in synthesizing covalently linkable peptide amphiphiles is discussed in this chapter. Covalent-linking motifs such as acrylates, vinyl ethers, and maleimides were used; however these functional groups did not work for a variety of reasons. Either the peptide amphiphiles would precipitate after polymerization or the functional group was not compatible with the coupling chemistry during solid phase peptide synthesis resulting in very low yields.

Although previous covalent-linking attempts were not successful, the introduction of the diacetylene motif, discussed in Chapter 3, was successful. The topochemical nature of diacetylene polymerization is well-known in solid state conditions;[6, 74] in order for polymerization to occur, the spatial and geometric orientations are very specific. Polymerization of the peptide amphiphiles was easily indicated by the clear to blue-purple colorimetric change, suggesting higher internal ordering of the PAs than previously believed. Interestingly, the polydiacetylene also displayed a circular dichroism (CD) signal, showing it was affected by chiral induction from the β-sheet. Additional diacetylene peptide amphiphiles were synthesized to prove that polymerization also occurs within PAs of different peptide sequence and length. CD spectra comparisons between the diacetylene PAs did show significant differences in intensity and band signature; while it is nontrivial to deconvolute the meaning of the spectral differences, these observations further emphasize the differences in structural packing between different PA nanoassemblies. The polymerization also increased the rigidity of the resulting self-supporting gel, enabling the micropatterning of various textures done in collaboration with Dr.

Alvaro Mata. This was the first example of creating patterned substrates using peptide amphiphiles. These patterns of varying nano- and micro-textured surfaces were then used to study cellular behavior, also done in collaboration with Dr. Alvaro Mata.

In Chapter 4, the introduction of the coumarin functional group into the peptide amphiphile was specifically designed with the objective of creating a reversible sol-gel material by utilizing the reversible coumarin dimerization reaction. Two coumarin PAs were synthesized, with the coumarin located either in the hydrophobic segments of the molecule or on a peptidic side chain. Crosslinking of both PAs was successful, however the crosslinking and uncrosslinking reactions never went to completion regardless of the concentration, solvent, or time of irradiation. The irreversibility of the reaction may be correlated to the crosslinked-constructs inhibiting any further reactions from occurring. It was interesting to observe that photo-induced crosslinking destroyed the morphology of the nanofibers, resulting in clusters of spherical aggregates. Because coumarin is also known for its biological uses, for example, as an anti-cell proliferation agent, coumarin PAs were also cultured on SKBr-3 cancer cells and were surprisingly found to be cytotoxic whereas the control PA without the coumarin molecule seemed to increase cancer cell proliferation. Continuing experiments include culturing other non-cancer cell lines in the presence of coumarin PA and the control PA to see whether the cytotoxic effect is found throughout multiple cell types.

As another approach towards designing large, self-assembling, multi-component structures, Chapter 5 describes two peptide amphiphiles that were synthesized to include complementary hydrogen bonding using either an adenine or thymine motif. CD spectroscopy shows nucleobase interactions of both homogenous and 1:1 mixed solutions of the two PAs.

Micrographs show the peptide amphiphiles maintain their nanofiber morphology with increased bundling of adjacent nanofibers in parallel orientation likely due to the fiber's peripheral hydrogen bonding propensities compared to non-nucleotide-containing PAs. Binding studies of each PA in the presence of polyadenylic acid (PolyA) also showed the PolyA to interact with both adenine- and thymine-containing PA nanofibers. TEM microscopy of the thymine PAs in the presence of PolyA, interestingly showed bumpy fiber-like nanostructures, which may be the PolyA coating the individual nanofibers. Ongoing investigations of this system also include gel binding assays of the PolyA/PA mixtures as well as mechanical testing using oscillatory rheology.

This thesis encompasses several different peptide amphiphile systems designed to form either covalent attachments or complementary hydrogen bonds. With covalently linkable PAs, we have been able to achieve the previously stated objectives by indirectly probing the interior structure of the nanofiber and also create mechanically improved gels resulting in the first ever production of PA micropatterns. The synthesis of PAs containing complementary hydrogen bonds also showed promise in building higher-ordered macromolecular structures by forming larger bundles of nanofibers. The propensity for nucleobase interaction between nanofibers also extends towards oligonucleotides, making these nucleobase-PA constructs applicable as DNA or RNA binding scaffolds.

Chapter 2: Probing the Internal Structure of Peptide Amphiphilic Nanofibers: The Development of Covalently Linkable Peptide Amphiphile Systems

The interest in attaching covalent linking functional groups to the PA structure stemmed both from early attempts to elucidate the interior structure of the PA nanofiber and the desire to generate materials with controllable mechanical stability. This chapter discusses the probing of the PA internal structure which led to the construction of covalently linkable PAs. Although the initial synthetic attempts in several covalently linkable PAs were not successful, the design and synthesis are still important to document here when considering future covalently linkable systems.

2.1 Introduction: Prior Studies of the PA Nanofiber Interior and Crosslinking Attempts

The first peptide amphiphile synthesized in the Stupp lab exhibited both crosslinking and nanofiber-forming capabilities, containing four consecutive cysteines with the sequence: C_4G_3S(P)RGD with a palmitic tail at the *N*-terminus[81, 82] (Figure 2.1). The rationale of this peptidic molecular design was to covalently capture the self-assembled nanofiber and enable biomineralization using acidic amino acids as well as incorporating an RGD moiety for cell adhesion. PA gelation was pH dependent, resulting in gelation below pH 4 and disassembly of the gel above pH 8; however, after the addition of 10 mM iodine to crosslink the cysteine thiols, the gel remained intact even at a pH greater than 8 suggesting increased stability of the material. This was the first and only successful example of covalently linking PAs until recently. However, there was limited structural and mechanical characterization from this work, which

invited further investigations of these PA systems.

Recently, there has been some insight on the general structure of the nanofiber without molecular labeling. The stability of the PA nanostructure significantly is known to rely on hydrophobic collapse of the alkyl tail and β-sheet formation. Recent infrared spectroscopy

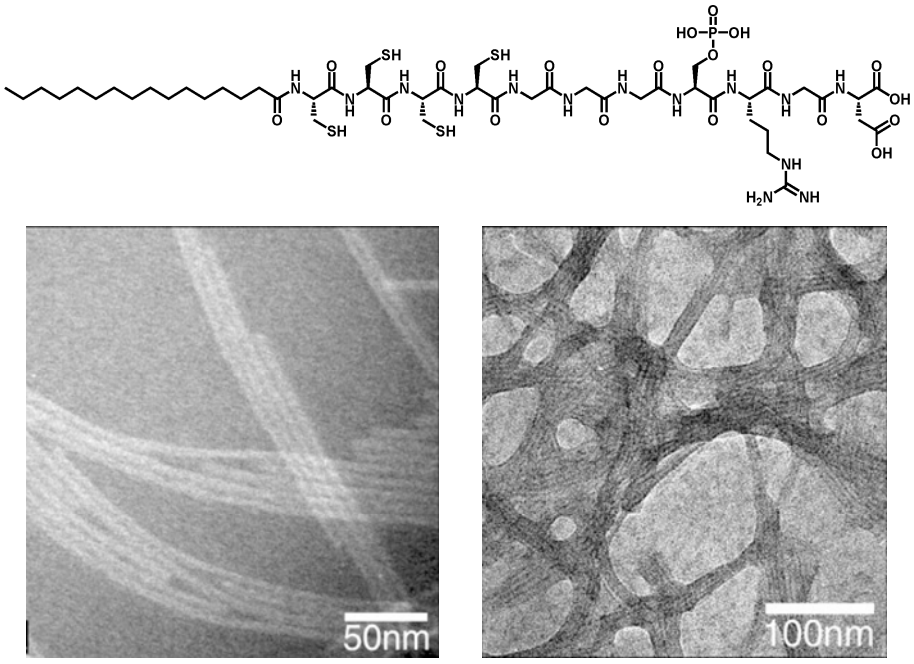

Figure 2.1. PA containing cysteine crosslinkers. (**Top**) The sequence is $C_4G_3S(P)RGD$ with a palmitic tail at the N-terminus. TEM images are shown of uncrosslinked fibers (**Left**) and crosslinked fibers (**Right**). Crosslinking was done by exposing the solution to 10 mM of iodine.

studies revealed the orientation of β-sheets to be parallel to the z-axis of the nanofiber.[83] Jiang et al. monitored the IR intensity of amide bands characteristic of the β-sheets by polarization modulation-infrared reflection-absorption spectroscopy (PM-IRRAS) on films of dry nanofibers to show that branched PAs, which have an additional peptidic arm stemming from the parent sequence, exhibited a lower degree of internal order than linear PAs, which have no peptidic side-chain modifications. The PM-IRRAS bands of the methyl peaks in the alkyl tails buried

within the nanofiber also followed the same trend observed with the amide bands, leading to the suggestion that there is correlation between the degree of ordering of the β-sheets and the hydrophobic core. Paramonov et al. also showed for their set of sequences that the four amino

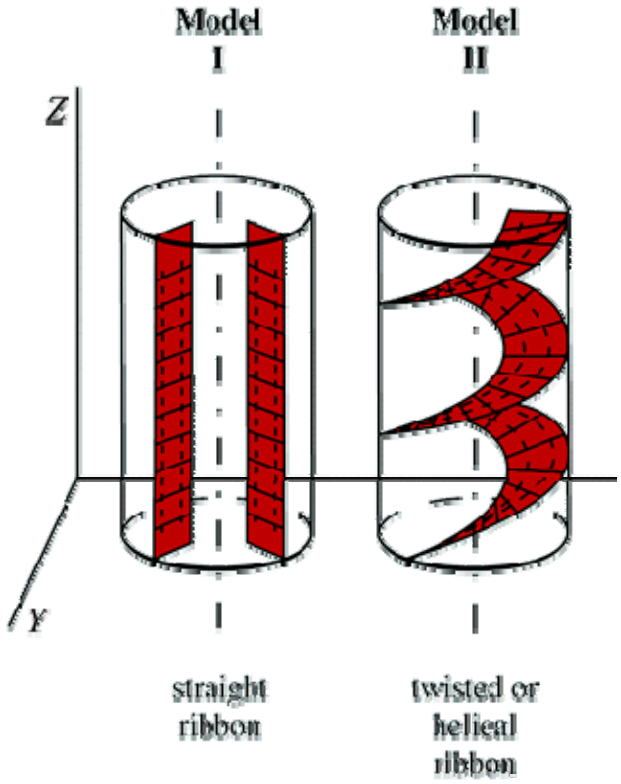

Figure 2.2. Proposed schematic of β-sheet orientation within a PA nanofiber.[6]

acids closest to the nanofiber core have the greatest impact in determining the formation of nanofibers by forming β-sheet hydrogen bonds and also proposed that the β-sheets were oriented either parallel to the long axis of the nanofiber or in a helical conformation with similar net orientation (Figure 2.2). Using systematic modifications of each PA synthesized, they also found that amino acids further away from the nanofiber core were not as important in stabilizing the nanostructure. While the findings from both examples are important, the spectra obtained were

from dried nanofiber films and may differ from PA structures in solution. Also, additional systematic studies using amino acids beyond alanine and glycine for linear PAs are needed, as both amino acids have weaker β-sheet forming propensities than many of the sequences used for biological studies in our group[84] (Table 2.1).

Other systems were also developed to probe the interior structure of the PA by including fluorophores with the PA system. Tovar et al. used Stern–Volmer quenching studies to show that the peptidic segment of the PA remained well solvated regardless of the chromophore location; however, those chromophores located more towards the nanofiber core did exhibit a reduced response in the presence of aqueous quenchers.[85] Another fluorescence study by Guler et al. investigated the PA encapsulation of free pyrene, which showed the importance of nanostructure morphology required to uptake and solubilize hydrophobic small molecules.[86] Encapsulation of the pyrene molecule occurred, as observed by excimer formation, only with well-packed nanofibers that formed β-sheets. Understanding the interior packing of PA nanofibers and solvent accessibility is important when considering the potential use of PA materials as drug release scaffolds.

Additional work that probes the PA structure is presented in the next section, investigating a series of PAs containing tryptophan chromophores positioned at different areas on the molecule. The rotational freedom of chromophores on each PA is measured by fluorescence anisotropy. From these findings, the degree of rotation freedom the chromophore has on the PA can be correlated to the rotational flexibility of a bioactive epitope in a similar environment which is important when designing bioactive materials.

Amino Acid	$\Delta\Delta G$[81] (kcal mol^{-1})	$\Delta\Delta G$[82] (kcal mol^{-1})	$\rho\beta$[87]
Ile	-0.56	-1.0	1.57
Phe	-0.55	-0.86	1.23
Val	-0.53	-0.82	1.64
Trp	-0.48	-0.54	1.24
Leu	-0.48	-0.51	1.17
Cys	-0.47	-0.52	1.07
Lys	-0.41	-0.27	0.73
Ala	-0.35	0.00	0.79
Gly	0	1.2	0.87

Table 2.1. Calculated β-sheet propensities for several amino acids. Values were obtained from three sources.

2.2 A Structural Study of PAs with Branched or Linear Architectures Containing Tryptophan

When designing bioactive materials containing epitopes, it is imperative to consider the presentation of the epitopes on the material substrate because molecular signaling occurs through binding recognition events. To ensure the epitope on a PA nanofiber is not buried or inaccessible for molecular signaling, fluorescence anisotropy is a useful tool to determine its rotation freedom. Fluorescence anisotropy measurements of several PAs with either a linear or branched architecture were taken to compare the accessibility of bioactive sequences using tryptophan chromophores.

The series of PA molecules synthesized and characterized were designed based upon the previous sequences used for the biotin-avidin binding study, in order to see if the anisotropy data would correlate. Six different PAs were synthesized (Figure 2.3), each containing a palmityl tail, a six amino acid β-sheet forming region of XXXAAA (X = G or L), a tryptophan chromophore, and a bioactive epitope sequence (RGDS). PAs **1** and **2** have linear architectures while PAs **3–6** have branched architectures, in which a lysine residue was utilized as the branching point. It should be noted that RGDS is a well-established bioactive epitope known to bind to integrin receptors for cell adhesion activity.[88] The single tryptophan chromophore was either placed before or after the RGDS epitope for both linear and branched PA architectures to monitor any changes in its rotational freedom, thereby gaining structural insight about the relative molecular packing between the 6 PA sequences. These PAs were synthesized using Fmoc-SPPS and orthogonal protecting groups, necessary to build the asymmetric branches on PAs **3–6** and for the final resin cleaving (Section 2.8 for experimental details.) The formation of self-supporting

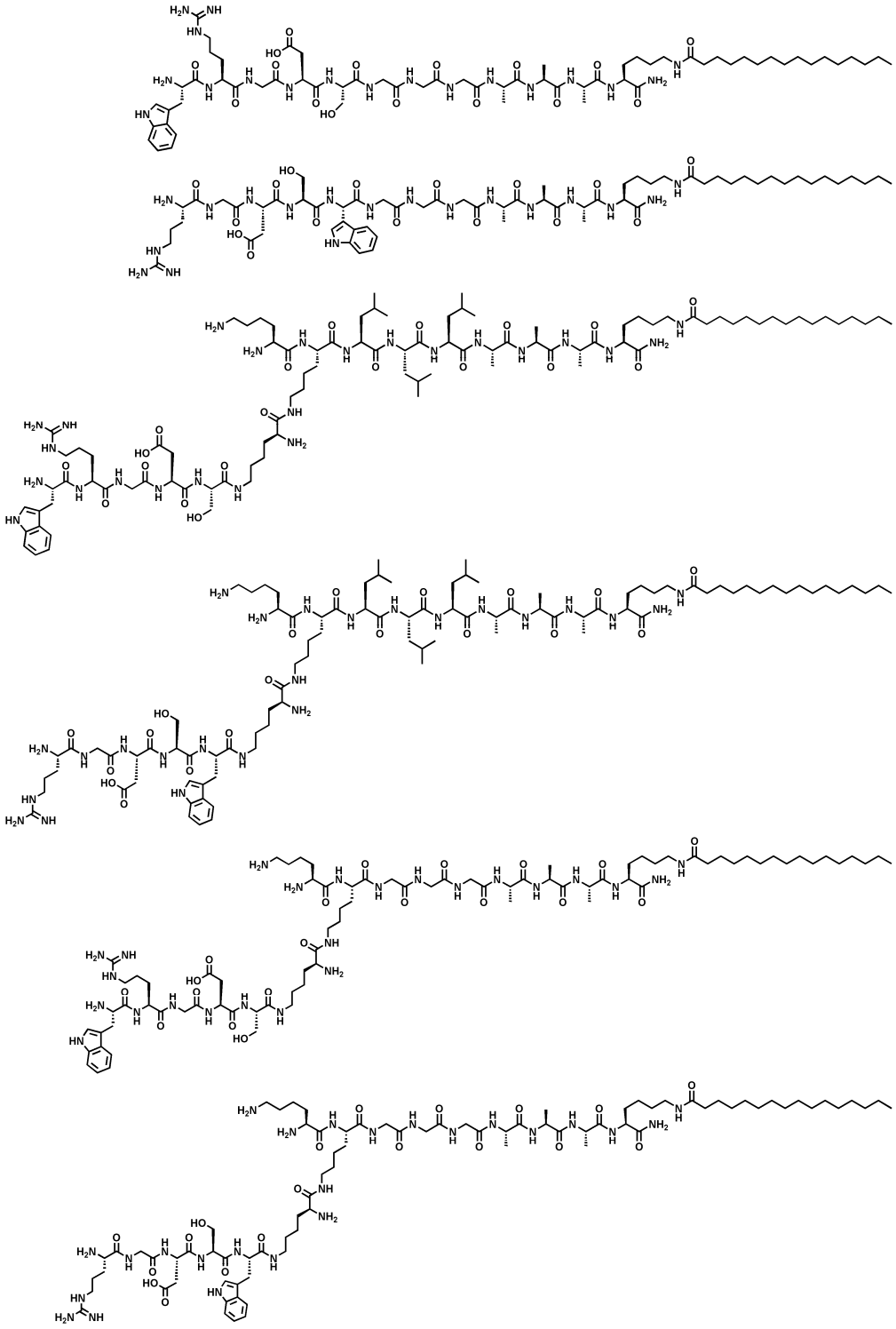

Figure 2.3. PAs containing tryptophan residues. PAs **1** and **2** have linear architectures. PAs **3–6** have branched architectures. PAs **1**, **3**, and **5** have the tryptophan at the terminal end of the molecule. PAs **2**, **4**, and **6** have the tryptophan after the RGDS epitope.

gels of the PAs **1–6** was possible at a minimum of 2 wt% when placed in a base chamber of ammonium hydroxide vapors for a few minutes. By microscopy, after a ten-fold dilution, high-aspect ratio nanofibers (Figure 2.4) were observed with diameters of approximately 7–11 nm and microns long in length. The presence of nanofibers suggests the existence of hydrogen-bonded secondary structures which was investigated using circular dichroism (CD) spectroscopy. Figure 2.5 shows a strong negative CD signal for all six PAs ranging with negative maxima at 210–215 nm. Classical β-sheets are known to exhibit a negative CD signal at 215 nm,[89] whereas unfolded or lesser structured β-sheets will show a shifted signal, as observed in PAs **1**,**2**, **5**, and **6**.[90] The observed shifting is not surprising for the four PAs that have the AAAGGG peptide sequence, given the low β-sheet forming propensities of alanine and glycines (Table 2.1). The negative band observed around 200 nm for PAs **5** and **6** also suggests the presence of random coil structures. The AAALLL sequence of PAs **3** and **4** should display a stronger β-sheet, which can be observed in the CD signal that closely resembles a classic β-sheet spectrum as shown in Figure 2.5, demonstrates a CD signal most closely resembling a classic β-sheet spectra within the PA series. Because β-sheet hydrogen bonding helps facilitate nanofiber formation and glycines are known to destabilize β-sheet secondary structures in proteins,[91, 92] from this work it appears PAs **3** and **4** would make the most structurally stable nanofibers. It is believed that structurally stable nanofibers will result in mechanically robust, however the correlation between β-sheet forming propensities in PAs and improved mechanical robustness is still being investigated within our group.

The difference in mechanical stiffness of PAs **1–4** was observed and quantified by oscillatory rheology. Strain amplitude sweeps were done for each PA sample in order to determine the linear viscoelastic region of the material followed by frequency sweep

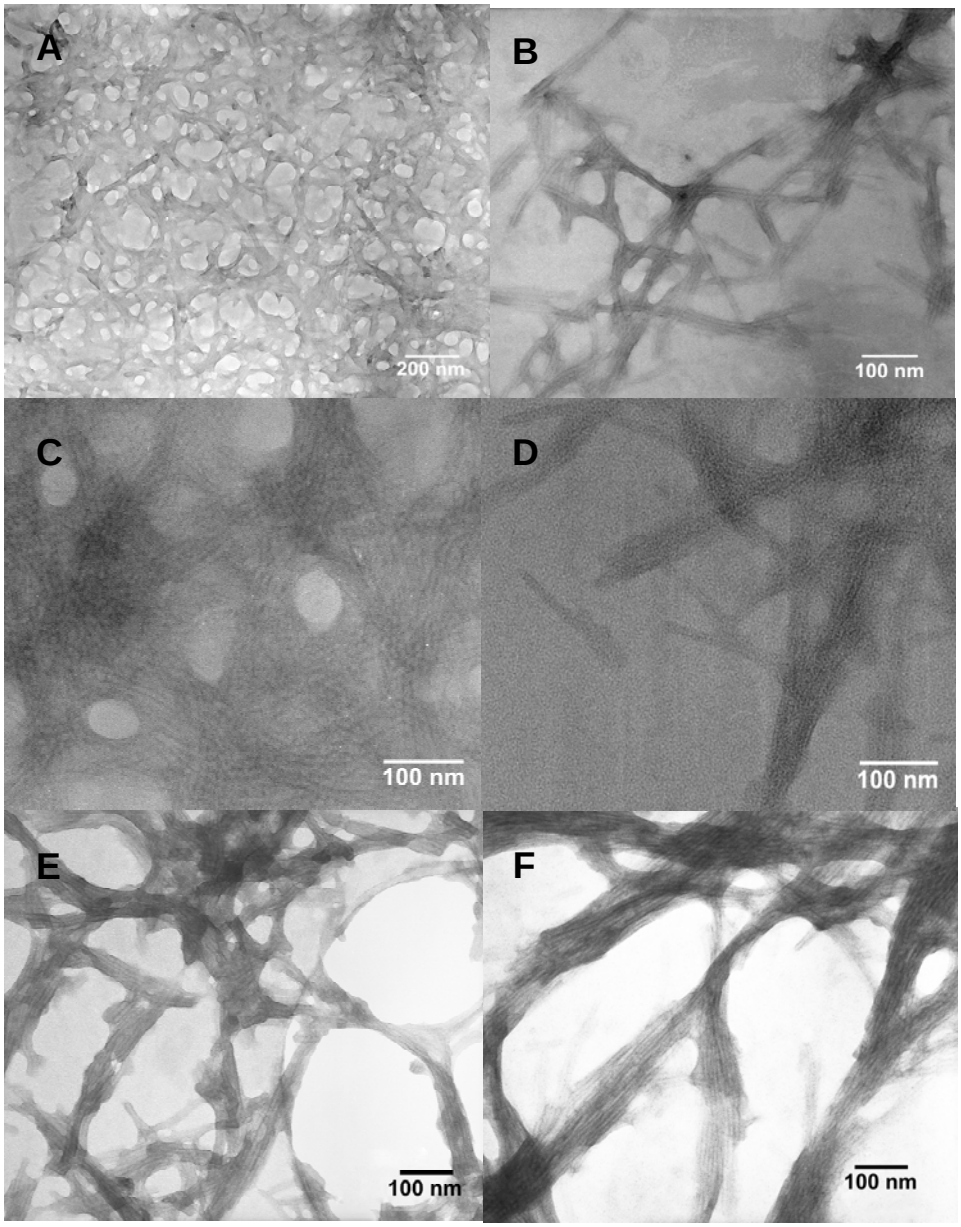

Figure 2.4. TEM micrographs of PAs **1–6** as A–F, respectively. Samples were negatively stained with 2% PTA. Samples were prepared from 0.1 wt% solutions.

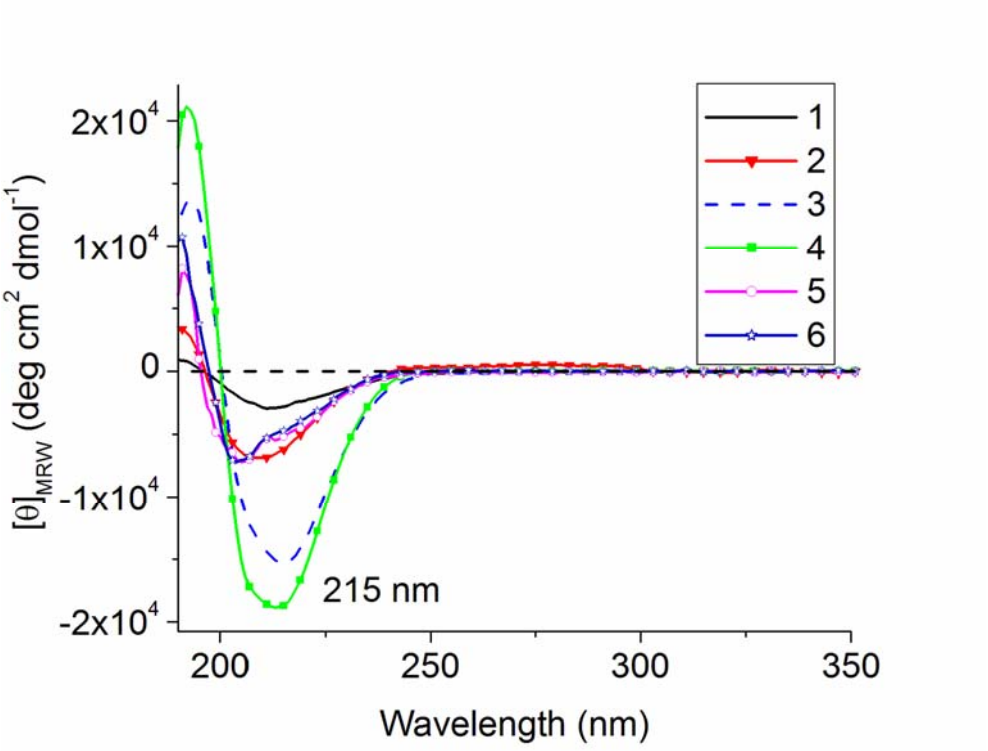

Figure 2.5. CD spectra of PAs **1–6** as 20 μM solutions with 100 mM NaPi.

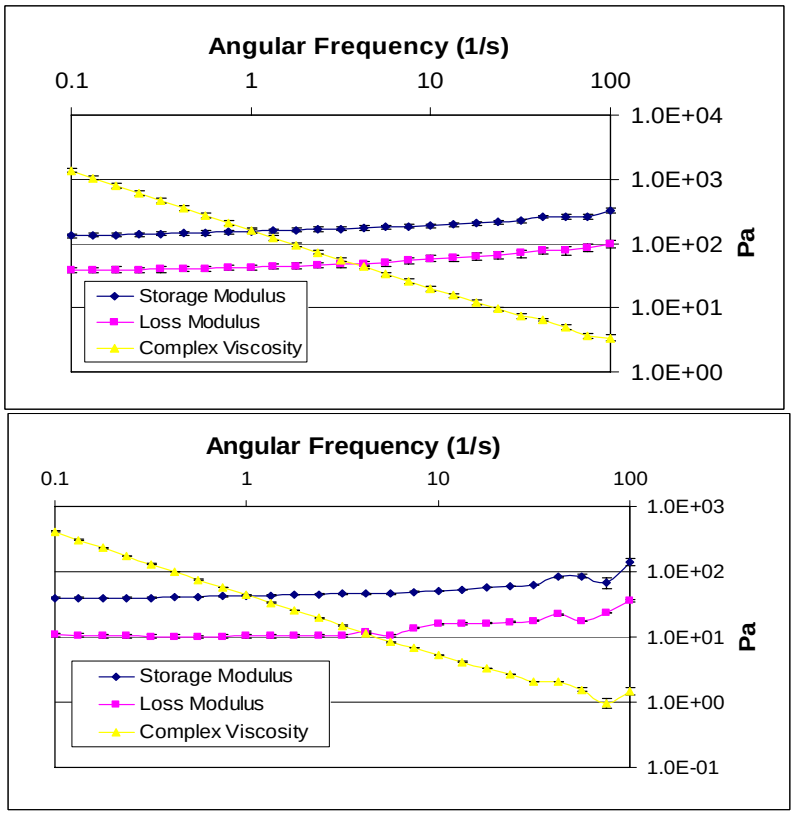

Figure 2.6. Frequency sweep of rheology data for **A**) PA **2** and **B**) PA **4** at 2 wt%. Amplitude strain was 3%.

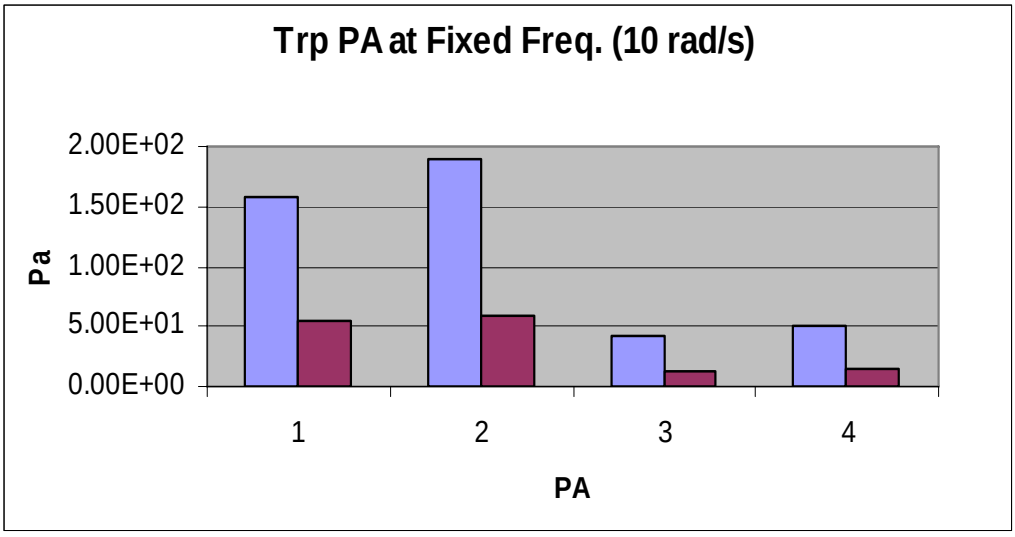

Figure 2.7. Rheology data of PAs **1–4**. Left bar (blue) is the storage modulus (G); right bar is the loss modulus (G").

measurements to record the storage (G) and loss moduli (G"). For all of the PA frequency sweeps, G' > G" at all points. A gel is defined as a material whose elastic modulus is at a non-zero equilibrium, as is shown in all of the studied PAs (Figure 2.6). More importantly, Figure 2.7 shows a moduli comparison of PAs **1–4** at a representative frequency point of 10 rad s^{-1} and immediately noticeable is the three-fold higher storage moduli of the linear PAs (**1** and **2**) compared to the branched PAs (**3** and **4**). It is postulated that the linear architecture allows better packed nanofiber formation and network formation than branched architectures, resulting in stiffer bulk materials.

Steady-state fluorescence anisotropy measurements were done to measure the relative degree of free rotation of the tryptophan chromophore for the PA series as shown in Table 2.2.

Table 2.2. Fluorescence anisotropy data of PAs **1–6** and free tryptophan.

Molecule	Fluorescence Anisotropy
1	0.33 ± 0.04
2	0.15 ± 0.04
3	0.13 ± 0.05
4	0.13 ± 0.06
5	0.16 ± 0.03
6	0.06 ± 0.03
Free Tryptophan	0.02 ± 0.01

$$\textbf{Eq. 1} \qquad r = \frac{I_{\parallel} - I_{\perp}}{I_{\parallel} + 2I_{\perp}}$$

Calculations for the anisotropy values, *r*, were calculated using Equation 1 where 'I' is the intensity either parallel or perpendicular to the incident polarization. The difference in anisotropy of the tryptophan chromophores relatively indicates how tightly the nanofibers are packed. The higher the anisotropy value, the more rotationally restricted is the chromophore.[93] In comparison to free tryptophan in solution, all of the PAs have higher anisotropy values due to the self-assembled nanofibers restricting the rotation of the PA tryptophan. PA **1** displays the highest anisotropy value, suggesting the packing of this linear PA restricts the tryptophan rotation more than its branched counterparts, PAs **3** and **5**, where the chromophore is exposed to the periphery of the nanofiber. However, no significant difference is observed between linear and branched PAs where the chromophore is buried before the RGDS epitope. This could be due to loose molecular packing by having the bulky tryptophan residue buried within the linear PA (2) instead of being towards the nanofiber periphery, as well as PA **2** having a weak β-sheet forming region. There appears to be no significant differences between the anisotropy values of the branched PAs regardless of its differences in β-sheet residues. The lack of significant difference between these branched PAs is somewhat surprising, as one would expect the PA with the stronger β-sheet forming residues to pack more efficiently. It is known that the rotational motion of the chromophore should increase the further it is located from a rigid substrate, and it is possible that in this particular series of PAs, the chromophores are all far enough away from the packed nanofiber core to show similar degrees of rotational freedom and anisotropy values.

In summary, a series of PAs containing a tryptophan residue were characterized by spectroscopy, microscopy, and rheology. Although the CD data showed not all PAs having classical β-sheet signals, all displayed fiber formation by microscopy. Rheology data showed linear PA gels to be stiffer than branched PAs, possibly due to more efficient molecular packing and network fiber formation. Fluorescence anisotropy measurements monitoring the rotational freedom of the tryptophan chromophore suggest the accessibility of the bioactive epitope was found to favor branched PAs and that the packing of the nanofiber is most likely dependent upon not only the sequence by the molecular shape of the molecule.

2.3 Molecular Design Considerations for Covalent-Linkable Peptide Amphiphiles

From the series of peptide amphiphiles containing chromophores previously discussed in Section 2.2, it was decided the next series of PAs would contain covalently linkable functional groups in order to further elucidate PA self-assembly and improve its bulk mechanical integrity. The design of covalently linkable PAs included several initial considerations: i) the initial PA architectures to study, ii) the best method of covalent linking, iii) the optimal location of the covalently linkable functional group, and iv) the consideration of possible applications.

The general PA structure as discussed in previous sections was maintained including the usage of alanine and leucine residues for the β-sheet region due to their prior success in β-sheet formation and nanofiber self-assembly (see Section 2.2). There were many options when selecting appropriate covalent linking methods which were divided into the categories of either crosslinkers or polymerizing functional groups. Both approaches seemed viable so long as the covalent linking did not require the extensive use of additives, so reactions involving

photopolymerization and photocrosslinking were considered more than others. Placement of the covalently linkable functional group with the PA molecule was varied to optimize comparison and solubility purposes. The targeted applications include the current uses of PA gels as bioactive scaffolds for tissue culture and regeneration. The stiffness of bioscaffolds is well documented to influence cellular differentiation and proliferation.[94, 95] The added covalent-linkable units on the PAs could potentially yield additional control over the mechanical stiffness of the PA scaffolds, allowing better tailoring of these bioscaffolds towards specific cell types.

2.4 Covalently Linkable Peptide Amphiphiles: Acrylamides

The initial attempts of synthesizing polymerizable PAs involved the incorporation of an acrylamide on to the *N*-terminus of the PA during solid phase peptide synthesis. Covalent linking of through radical polymerization generates polyacrylamide commonly used in molecular biology for gel electrophoresis and also as aqueous thickeners.[96, 97] The incorporation of acrylamides in SPPS had been demonstrated before in literature,[98] and at the time, appeared as a straightforward method to obtain acrylamide-PAs for future polymerization reactions.

The first synthetic endeavor was the synthesis of the branched PA **7** (Figure 2.8), consisting of a Leu-Leu-Ala-Ala β-sheet region and lysine residues for solubility. The branched architecture was initially used, since previous structural probing of the nanofiber suggested branched PAs to have a less packed periphery, which should enable the acrylamide sites to be more accessible for polymerization. Acryloyl chloride in DCM for 30 minutes was the final coupling step before the final cleaving step with the 95% TFA cleaving cocktail. This coupling for future SPPS syntheses was repeated using varying molar equivalents of the acryloyl chloride

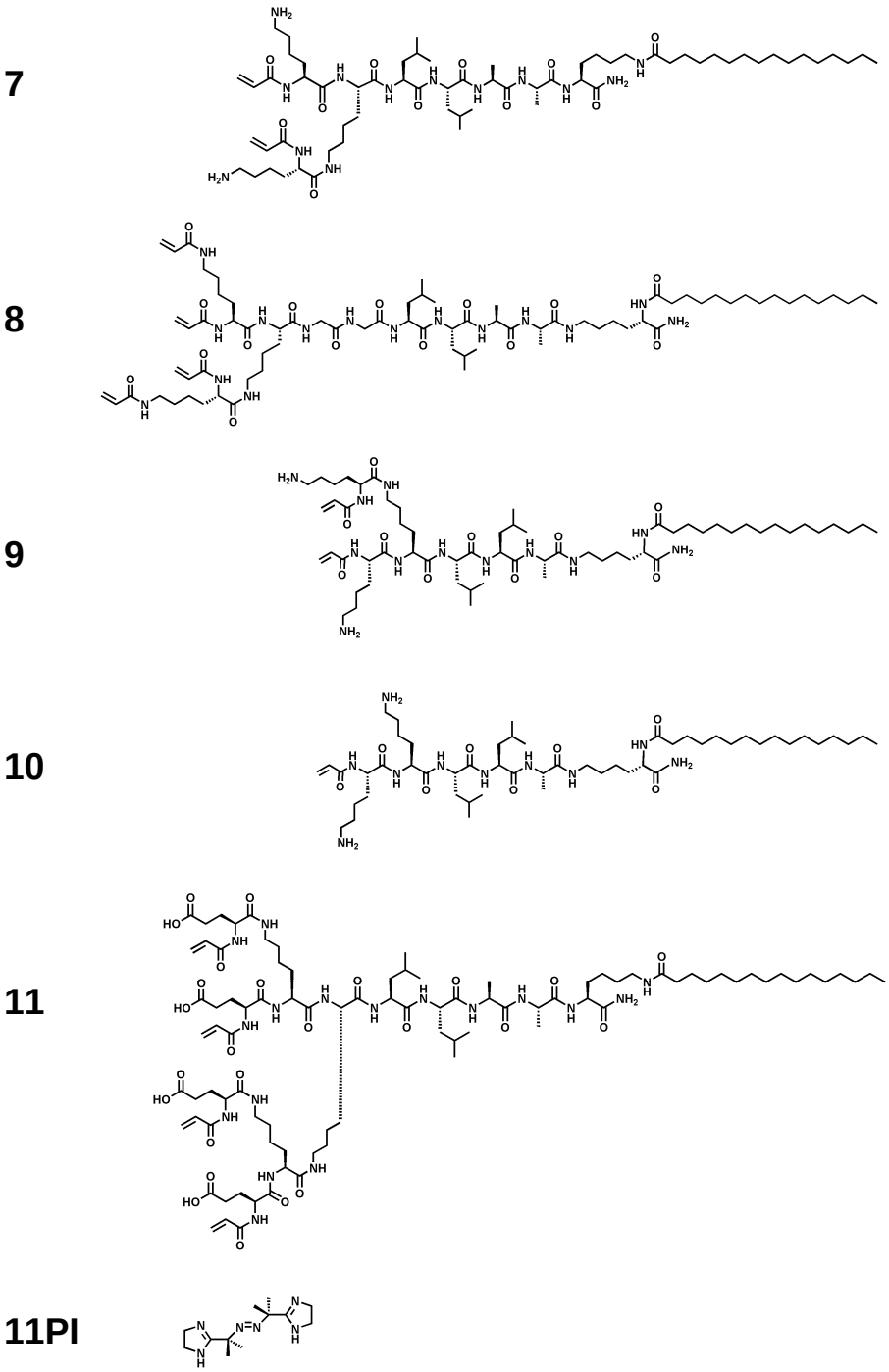

Figure 2.8. PAs containing acrylamide functional groups. All PAs except **10** have a branched architecture. It should be noted that PAs **8–10** have the palmitic tail on the α-amine based upon synthetic limitations from using HMPB MBHA resin. **11PI** is the photoinitiator (VA-044) used to polymerize **11**.

in combination with different mild bases to scavenge any generated HCl, but the mass spectrometry results after cleaving showed no product mass (M^+_{calc}: 1244.69). There was concern for side reactions from the harsh cleaving conditions, hence the solid support was changed to HMPB MBHA resin, which requires only mild acidic cleaving conditions.

PAs **8–10** were synthesized using HMPB MBHA resin and cleaving using a 5% TFA cleaving cocktail. A Gly-Gly spacer was added in conjunction with the branching architecture for PA **8**, to allow flexibility for the peripheral amino acids and still allow β-sheet organization of the interior amino acids. The synthesis was successful, but the PA was unable to form gels up to 4 wt% most likely due to poor self-assembly from inefficient packing of the flexible glycine spacer and the bulky branched head group. The synthesis of PAs **9** and **10** were attempted in order to decrease the number of acrylamide groups and simplify synthesis, but coupling of the acryloyl chloride never yielded in the desired product by mass spectrometry.

The formation of PAs **7–10** may have been inhibited by the side reaction between the nucleophilic ε-amine of the lysine and one of the adjacent acrylamide groups, leading to the sequence modification of replacing the terminal lysine residues with glutamic acids. PA **11** was synthesized to have terminal glutamic acids further functionalized with acrylic acid. Mass spectrometry of the crude material showed presence of the product (M^+_{calc}: 1869.24; M^+_{obs}: 1869.42) as well as the presence of at least two additional peaks 55+ mass units apart which correlates to the coupling of extra acrylic molecules. The purification of this molecule by HPLC was difficult due to the numerous byproducts with similar masses, resulting in yields too low to attempt polymerization after purification. Polymerization of the crude PA **11** was attempted using a water soluble photoinitiator, VA-044 (**11PI**, Figure 2.8) following the manufacturer's

protocol. The radical polymerization reaction resulted in insoluble precipitate and mass spectrometry still showed the PA monomer, but no other obvious masses attributable to successful polymerization. Other characterization attempts such as GPC also did not give conclusive evidence of polymerization.

Because the polymerization of PA **11** only led to insoluble precipitates, it was decided acrylamide reactions were not well suited these aqueous supramolecular systems. The other lesson learned was the importance of placing the covalent linking functional group within the nanofiber for solubility purposes. Furthermore, this keeps the periphery of the nanofiber available for the presentation of bioactive epitopes.

2.5 Covalently Linkable Peptide Amphiphiles: Acrylate Synthesis

The acrylate functional group was selected since acrylate polymers are ubiquitous in the synthesis of transparent, robust materials and have also been incorporated into polymeric hydrogels[99] for potential drug delivery applications.[100] The reaction occurs by radical polymerization typically with the addition of an initiator. The synthesis of PAs containing the acrylate motif was not successful, however the synthetic strategies will be briefly discussed in this section.

The target molecule consisted of a PA with an alkyl acrylate tail, first requiring the synthesis of the modified lipid tail. The protocol for the synthesis of 12-acryloyloxydodecanoic acid was adapted from Karino et al. in their synthesis of copolymers with alkyl side chains.[101] 12-Hydroxydodecanoic acid was reacted with TEA and acryloyl chloride in DCM at -30°C followed by an unsuccessful attempt to precipitate the product under acidic conditions (Figure

2.9). Purification of the precipitate by column chromatography still yielded only starting material and another product that could not be identified by ^{1}H NMR. It was discovered that recrystallization of the crude product in MeOH resulted in pure product, but the isolated yield was too low to continue to the next step (<1%). Scaling up of the reaction also resulted in the intermolecular reaction between the carboxylic acid and the alcohol of two starting material molecules as well as attachment of the acryloyl group, byproduct **2.2**. Acrylate synthesis was also tried using acrylic acid by carbodiimide coupling. The crude NMR showed the presence of both products and byproducts, but the desired product could not be isolated by column chromatography. Similarly, coupling using DPTS and DIPC[73] also yielded no product as observed by NMR.

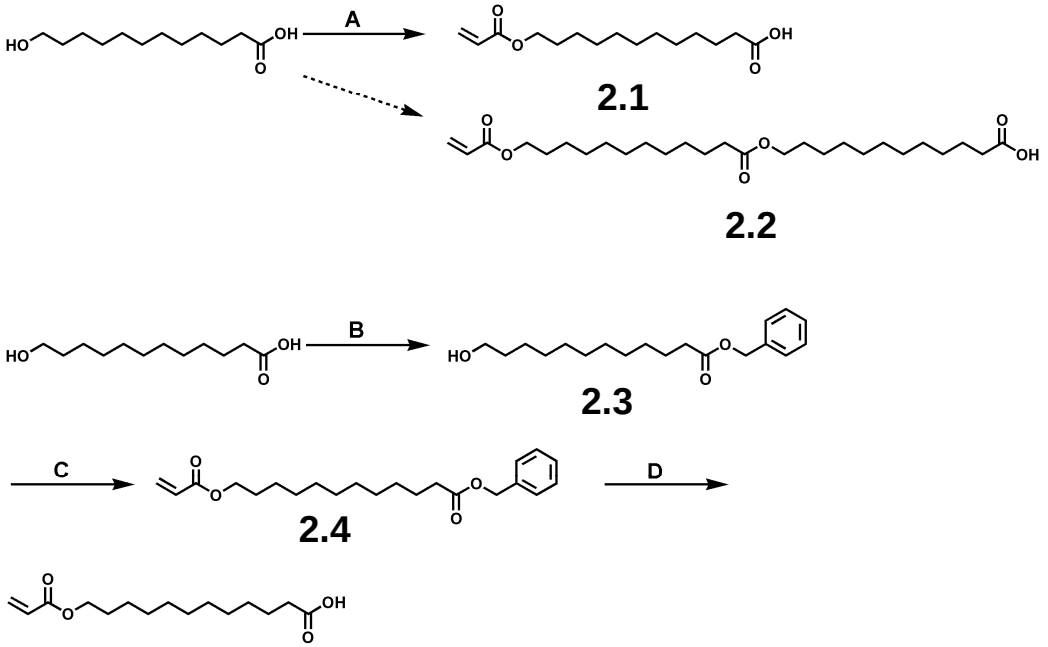

Figure 2.9. Synthetic routes towards **2.1**. Synthesis towards **2.1** using conditions **A**) TEA, acryloyl chloride, DCM, -30°C, 21 h, also resulted in **2.2**. A different approach was attempted using conditions **B**) BnBr, K_2CO_3, 72°C; **C**) TEA, acryloyl chloride, DCM, 0°C, 30 min; **D**) K_2CO_3, THF/H_2O, rt. **2.4** was synthesized, but the final deprotection step was not possible.

The low yields and difficult purification led to carboxylic acid protection strategies, initially with a *t*-butyl protection group. Coupling of *t*-butyl alcohol using carbodiimide chemistry yielded undesired protection of the terminal alcohol group as well as the acid. The acid was instead protected with a benzyl group (**2.3**) in good yield followed by reaction with acryloyl chloride (**2.4**) resulting in a 48% yield after column chromatography. The benzyl group was chosen to allow a mild deprotection method found using potassium carbonate instead of the typical protocol of hydrogenation over Pd/C, which would destroy the acryloyl group. Unfortunately, the deprotection under those conditions did not work and the benzyl group could not be removed without potentially affecting the acryloyl group. No other synthetic strategies were attempted, but these studies emphasized the importance of finding a protecting group on the acid easier purification, fewer byproducts, and higher yields.

2.6 Covalently Linkable Peptide Amphiphiles: Vinyl/Sorbyl Ether and Maleimide Synthesis

As previously mentioned, there is limited knowledge regarding interfiber exchange of PA molecules, due to the difficulty of probing individual molecular behavior within a supramolecular construct. The mixing of two PA molecules has been theoretically examined[102] to form localized, charge-dependent patterns on the surfaces of the nanofibers. Although the mixing of PAs have been briefly looked at experimentally,[103] the degree to which phase separation occurs or the heterogeneity a nanofiber may have is still unclear. To help increase the mixing factor, there was the idea of incorporating two different polymerizing functional groups that favor the formation of alternating copolymers, one each into two different PAs that would

eventually be mixed. Analysis of the polymer–PA product, could not only result in the development of new materials, but also help answer the questions regarding the extent of PA mixing within a nanofiber.

Polymerizations of donor–acceptor monomers to form alternating copolymer systems can occur through the formation of charge-transfer complexes when irradiated, resulting in free radical polymerization.[104, 105] One of the most well-studied donor–acceptor alternating copolymer systems consists of the vinyl ether (VE) monomer as the donor, and an *N*-substituted maleimide (MI) monomer as the acceptor.[106, 107] This reaction does not require a photoinitiator and begins from photoirradiation of the maleimide,[108-111] resulting in hydrogen abstraction from one of the two monomers, producing free radicals. Due to the donor–acceptor character of the polymerization, the radical of the electron-rich VE alkyl will only react with the electron-poor MI monomer. Studies have also shown propagation to occur through the homopolymerization of an acceptor–donor ([MI–VE]) complex, resulting in the growth of an alternating MI–VE copolymer. It is known that homopolymerization of MI can occur, however an excess of VE monomer was shown to completely suppress this.[112] The incorporation of each monomer into the PA is discussed in this section. Similar to the target molecule for the acrylate alkyl tail (section 2.5), both VE and MI monomers will be incorporated into an alkyl tail suited for SPPS synthesis.

2.6.1. Vinyl Ether/ Allyl Ether Synthesis

Synthesis of the vinyl ether alkyl tail (**2.5**) was attempted following similar protocols[113, 114] by reacting an acetaldehyde enolate, formed from the cycloreversion of THF, with 11-bromoundecanoic acid. Initial attempts involved enolate formation using *t*-butyllithium (Figure

2.10). The *in situ* formation of the enolate seemed promising due to the yellow coloration of the solution, but the ^{1}H NMR spectrum with peaks showed only starting material with no resonance for the desired vinyl group. After several unsuccessful attempts, LDA was used instead of *t*-BuLi with similar results. Protection of the acid prior to the enolate chemistry with a

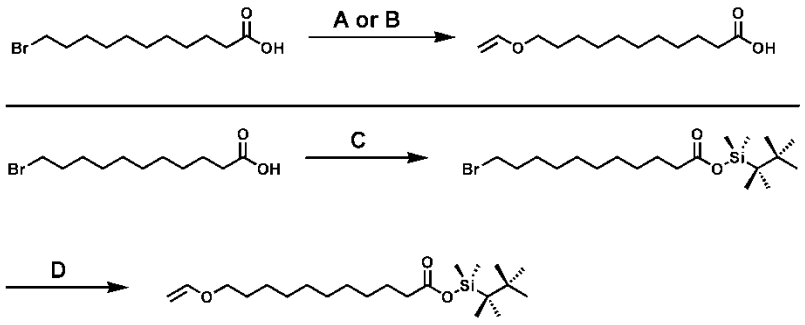

Figure 2.10. Synthetic routes towards vinyl ether alkyl tail **2.5**. Synthesis towards **2.5** using conditions **A**) *t*-BuLi, acetaldehyde, and THF to form the enolate *in situ,* added at -75°C **B**) LDA, acetaldehyde, THF to form the enolate *in situ*, added at -75°C. Unsuccessful attempts led to the protection strategy of the acid group prior to enolation using conditions **C**) imidazole, DMHSCl, DMF, 48 h, 30°C yielding **2.6**. Enolation reaction **D**) same as conditions **A** or **B**

dimethylhexylsilyl (DMHS) protecting group (**2.6**) also did not yield in the desired product. It is not clear why the reaction did not proceed as intended, but the enolate may have been too unstable and short-lived for its reaction with the bromoalkyl acid. Instead of synthesizing a vinyl ether, it was decided the synthesis of an allyl ether may be less unstable and yield more success.

Allyl ether monomers, like vinyl ethers, have also shown copolymerization with maleimide monomers.[80, 115-117] The synthesis of **2.7** first involved methyl protection of the acid (**2.8**) followed by addition of allyl bromide and sodium hydride (Figure 2.11). The product (**2.9**) was extracted by column chromatography in DCM with a yield of 3%. Hydrolysis of the methyl

ester protecting group was possible only in very low yield. This section of the VE–MI project was disappointing, as the synthesis was challenging and the product yields were too low to consider continuing large-batch syntheses that would be needed for PA synthesis with the VE alkyl tail.

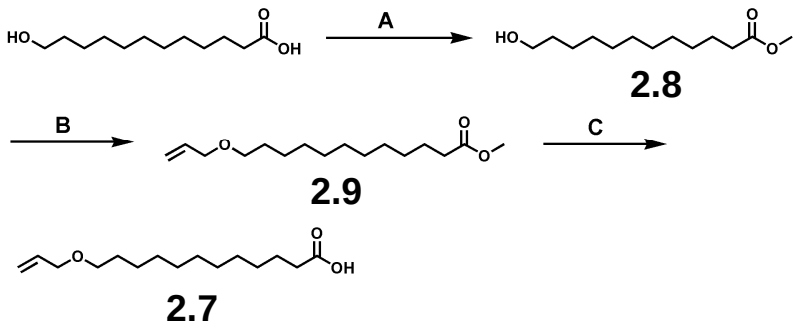

Figure 2.11. Synthesis of allyl ether alkyl tail **2.7**. **A**) MeOH, EDCI, rt **B**) allyl bromide, NaH, THF, 0°C **C**) LiOH, MeOH, 0°C.

2.6.2 Maleimide Synthesis

The synthesis of an *N*-maleimide alkyl tail (**2.10**) could be completed in two steps from commercially available materials using literature procedures[118] (Figure 2.12). The first step involved ring opening of the maleic anhydride by the primary amine of 12-aminododecanoic acid (**2.11**). The product was recrystallized with isopropanol and water with a 61% yield. The second step involved closing ring-closure using acetic anhydride and sodium acetate. The solution was extracted using ether and the crude product was dried *in vacuo*. Purification through recrystallization in hexanes gave a final yield of 53%. It is noted that initial work up attempts by silica gel chromatography (ethyl acetate/hexanes) followed by recrystallization with more apolar solvent mixtures yielded in product with significantly lower isolated yields.

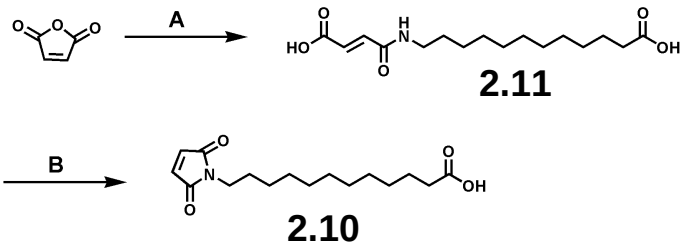

Figure 2.12. Synthesis of maleimide alkyl tail **2.10**. **A**) 12-aminododecanoic acid, glacial acetic acid, rt **B**) acetic anhydride, sodium acetate, 1 h, 90°C.

PA synthesis using Fmoc SPPS was used to synthesize the maleimide-containing PA. The sequence Lys-Lys-Leu-Leu-Ala-Lys was attached to the maleimide alkyl tail and purified by HPLC. Mass spectrometry of the product showed the mass of 979.43 (M^{+}_{calc}: 976.3). Although the synthesis of the maleimide PA was possible, the copolymerization project was not continued due to the difficulties in synthesizing the allyl ether counterpart.

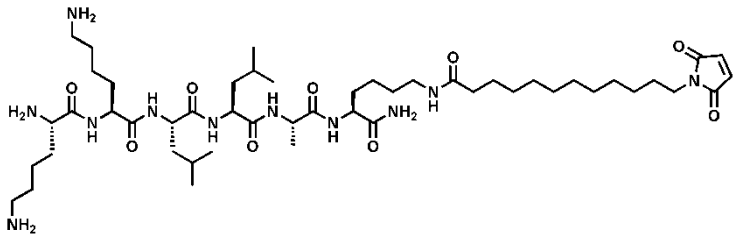

Figure 2.13. Structure of the maleimide PA, synthesized by Fmoc SPPS.

2.7 Conclusions

In summary, the investigations regarding the internal structure of the PA have shown linear PA nanofibers, in general, to exhibit reduced epitope presentation. The series of tryptophan PAs have also shown increased restricted rotational freedom of molecules the further

they are placed within the nanofiber, particularly for linear PA architectures. Although much structural information has been gleaned from chromophore-tagged PAs, covalent trapping of these supramolecular systems may also yield structural information.

Covalent-linking of PA nanofibers is desired not only for structural characterization, but also for the development of materials with greater mechanical integrity. Initial attempts to incorporate acrylamides resulted in precipitation of the PA. This emphasized the importance regarding the placement of covalent-linking functional groups; the future designs of covalent-linking PAs have their reactive motifs buried within the PA nanofiber. The syntheses of acrylate and vinyl ether systems proved challenging, with yields too low to continue on to SPPS. Although the maleimide PA was synthesized successfully, the absence of its vinyl ether or allyl ether PA counterpart prevented further progress on the alternating copolymerization studies. Since the termination of these projects, more promising functional groups have been discovered and successfully incorporated into PA nanofibers. These systems will be discussed in the following chapters.

2.7 Experimental

2.8.1 Materials

All amino acids and resins were purchased from Novabiochem Corporation (San Diego, CA), AnaSpec Corporation (San Jose, CA), and Advanced ChemTech (Louisville, KY). Acryloyl chloride was purchased from Sigma-Aldrich (St. Louis, MO) and distilled before use. The photoinitiator, VA-044, was purchased from Wako Pure Chemical Industries, Ltd. (Richmond, VA) and used as provided. All other reagents and solvents for peptide synthesis

were purchased from Sigma-Aldrich or Mallinckrodt (Hazelwood, MO) and used as provided. NMRs were taken using Varian Inova 500 NMR (500 MHz for ^{1}H; 120 MHz for ^{13}C) spectrometer (Palo Alto, CA).

2.8.2 Synthesis

All PAs were manually synthesized by Fmoc solid-phase peptide synthesis using orthogonal protecting strategies in 0.10 to 0.40 mmol scales. All peptide amphiphiles contain a C-terminal amide group using Rink Amide MBHA resin or HMPB MBHA resin. The resin was initially swelled for 30 min in dichloromethane (DCM). Deprotection of the Fmoc protecting groups was done using 30% piperidine in dimethylformamide (DMF). All protected amino acids were activated using 4 equivalents of the amino acid, 4 equivalents of 2-(1H-benzotriazole-1-yl)-1,1,3,3-*N,N,N',N'*-tetramethyluronium hexafluorophosphate (HBTU), and 6 equivalents of diisopropylethylamine (DIEA) in DMF. The coupling cocktail was added to the resin beads after approximately 2 min of activation followed by at either 2–12 hours of coupling, depending on coupling difficulty.

When using Rink Amide MBHA resin, the first amino acid coupling was Fmoc-Lys(Mtt)-OH followed by deprotection of the Mtt protecting group using a 5% trifluoroacetic acid (TFA) cleaving cocktail consisting of TFA, triisopropylsilane (TIPS), and water (95:2.5:2.5, respectively) diluted in DCM. Subsequent to the Mtt deprotection, coupling of the alkyl tail or a derivative was done using a similar coupling method as previously described. It should be noted that the coupling cocktail for alkyl tails and derivatives was dissolved in a 1:2 mixture of DCM:DMF. Cleaving of the PA from the resin, including any acid labile protecting groups, was

done using the TFA cleaving cocktail (TFA, TIPS, water in a ratio of 95:2.5:2.5) for 2–3 hours at room temperature.

For syntheses using HMPB MBHA resin, the first amino acid coupled was Fmoc-Lys(Dde)-OH (6 equiv) in a mixture of dry DCM and DMF with 3 equivalents of DIEA and DCC were added. The activation reaction proceeded for 20 min at 0°C followed by filtration of the precipitate. After *in vacuo* removal of DCM, additional DMF and DMAP (0.1 equiv) was added to the coupling solution. The coupling solution was added to the resin and allowed to react for 9 h. After Fmoc deprotection using previously described conditions, coupling of the alkyl tail or a derivative was done using a similar coupling method as previously described. Following the alkyl coupling, deprotection of Dde was done using 2% hydrazine in DMF for 20 min. Cleaving conditions for HMPB MBHA resin was using 5% TFA cleaving cocktail in DCM for 5 min, repeated 3 times.

Monitoring of each deprotection and coupling reaction was typically done with a Kaiser test, testing for the presence of free primary amines by sacrificing a few resin beads. In the present of free amines, a blue/purple color change is observed; a negative test displays no color change (yellow). Three individual solutions are combined for the Kaiser test being: A) ninhydrin (5%, w/v) in ethanol (EtOH), B) phenol (4:1, w/v) in EtOH, and C) potassium cyanide (2%, v/v, of a 1 mmole/liter aqueous solution) in pyridine. A 1:1:1 volume ratio of each of the three solutions are added to the few beads, the sample is agitated, and placed in a sand bath heated to 120°C for 1 min. The sample color is then observed for the presence of free amines.

Following the PA cleavage and collection of the mother liquor, separated from the resin, the volume of the solvent is reduced *in vacuo*. Cold ether is added to the viscous solution,

yielding an off-white to white precipitate. The precipitate was collected by centrifugation and washed several times with cold ether, followed by drying under nitrogen gas. All PAs were purified by preparatory high performance liquid chromatography (HPLC) in a water/acetonitrile gradient containing 0.1% v/v TFA using an Atlantis C_{18} RP column (Waters Corporation, Milford, MA). HPLC fractions were collected and identified by mass spectrometry followed by lyophilization of the desired fraction. Analytical HPLC, using an Atlantic C_{18} RP column, was utilized to also confirm the purity of the compound afterwards coupled with mass spectrometry by an ABI Voyager DE Pro MALDI-TOF (Applied Biosystems, Foster City, CA) or an Agilent ESI spectrometer (Santa Clara, CA). All samples were stored in dry conditions until use.

Polymerization of PAs

PA solutions were sparged in an air-tight flask for 30 min with nitrogen gas. 0.01 mmol VA-044 (**7PI**) was dissolved in sparged Milli-Q water (18.2 Ω). The half life of the photoinitiator is labeled to be 10 h in H_2O at 44°C. To PA (1 mmol) was added the VA-044 solution, activating the reaction at 45°C. Reaction times ranged from a 1–9 h Resulting precipitate was collected and characterized by mass spectrometry.

12-Acryloyloxydodecanoic acid (2.1). To a round bottom with 12-hydroxydodecanoic acid (1.0 g, 4.62 mmol) was added TEA (1.5 equiv, 6.93 mmol) and dry DCM. While stirring, acryloyl chloride (1.1 equiv, 5.08 mmol) was slowly added over 15 min. The reaction continued at -30°C for 21 h. The solution was filtered and quenched with water. 1M NaOH in 2 mL water was added dropwise at 0°C and the solution was stirred for 45 min. The pH was adjusted to 1 using 1M HCl followed by complete removal of the solvents. The precipitate was recrystallized

by MeOH yielding a white product (~6 mg, <1%). ^{1}H NMR (500 MHz, $CDCl_3$): δ 6.40 (d, *J* = 17.5 Hz, 1H), 6.12 (dd, *J* = 10.5 Hz, 1H), 5.81 (d, *J* = 10.5 Hz, 1H), 4.14 (t, *J* = 6.5 Hz, 1H), 4.05 (t, *J* = 6.5 Hz, 1H), 2.29 (t, *J* = 7.5 Hz, 2H), 1.64 (m, 4H), 1.27 (br s, 14H).

Benzyl 12-hydroxydodecanoate (2.3). To a round bottom of 12-hydroxydodecanoic acid (0.5 g, 2.31 mmol), potassium carbonate (1 equiv) and benzyl bromide (1 equiv) was added. The reaction continued at 72°C for at least 24 h. An acid wash was followed by DCM extraction and dried with $MgSO_4$. The product was collected after rotary evaporation yielding a white solid (0.70g, 99%). ^{1}H NMR (500 MHz, $CDCl_3$): δ 7.36 (m, *J* = 3.0 Hz, 5H), 5.13 (s, 2H), 3.66 (t, *J* = 7.0 Hz, 2H), 2.37 (t, *J* = 7.5 Hz, 2H), 1.66 (qn, *J* = 7.0 Hz, 2H), 1.58 (qn, *J* = 6.5 Hz, 2H), 1.28 (br s, 14H).

Benzyl 12-acryloyldodecanoate (2.4). TEA (1.3 equiv) was added to benzyl 12-hydroxydodecanoate (0.465 g, 1.52 mmol) in dry DCM. Acryloyl chloride (5 equiv) was slowly added and the reaction continued for 30 min at 0°C. The solution was washed in brine and the organic fraction was dried with $MgSO_4$. Purification was done running a silica gel chromatography (3% MeOH in DCM). The product was collected after rotary evaporation yielding a white solid (0.26 g, 48%). ^{1}H NMR (500 MHz, $CDCl_3$): δ 7.37 (m, *J* = 5.5 Hz, 5H), 6.41 (d, *J* = 17.5 Hz, 1H), 6.14 (dd, *J* = 10.0, 1H), 5.82 (d, *J* = 10.5 Hz, 1H), 5.13 (s, 2H), 4.16 (t, *J* = 6.5 Hz, 2H), 2.37 (t, *J* = 7.5 Hz, 2H), 1.66 (m, *J* = 7.5 Hz, 4H), 1.28 (br s, 14H).

Dimethylhexylsilyl 11-bromoundecanoate (2.6). Imidazole (2.5 equiv, 0.64 g) and DMHSCl (1.2 equiv, 0.89 mL) in DMF was added to 11-bromoundecanoic acid (3.77 mmol, 1.0 g). The reaction was allowed to stir for 48 h at 30°C. The product was extracted from DCM and the solvent was removed *in vacuo*. The reaction went to equivalency and no purification was done yielding a white solid (1.53 g, quantitative). ^{1}H NMR (500 MHz, $CDCl_3$): δ 3.39 (t, *J* = 7.0 Hz, 2H), 2.16 (t, *J* = 7.5 Hz, 2H), 1.63 (qn, *J* = 7.0 Hz, 2H), 1.45 (at, *J* = 7.0 Hz, 2H), 1.28 (at, *J* = 6.0 Hz, 2H), 1.15 (br s, 10H), 0.75 (m, 15H), 0.17 (s, 6H).

Methyl 12-hydroxydecanoate (2.8). 12-hydroxydodecanoic acid (1.0 g, 4.623 mmol) was added with anhydrous MeOH and EDCI (1.5 equiv, 1.33 g) in DCM. The reaction ran at room temperature overnight. The reaction went to equivalency and no purification was done yielding a white solid (0.99 g, quantitative). ^{1}H NMR (500 MHz, $CDCl_3$): δ 3.67 (s, 3H), 3.41 (t, *J* = 6.5 Hz, 2H), 2.31 (t, *J* = 7.5 Hz, 2H), 1.85 (q, *J* = 7.5 Hz, 2), 1.62 (at, *J* = 6.0 Hz, 2H), 1.42 (at, *J* = 6.0 Hz, 2H), 1.29 (br s, 12H).

Methyl 12-(allyloxy)dodecanoate (2.9). Methyl 12-hydroxydodecanoate (0.1 g, 0.43 mmol) was added with allyl bromide (1.2 equiv) and NaH (2 equiv). The reaction went 12 h at 0°C. Organic fractions were extracted from a DCM/water wash and the solvent was removed by rotary evaporation. The crude product was purified by silica gel chromatography using a hexane/ethyl acetate mobile solvent (4:1 ratio, respectively) and the solvent from the collected fractions were removed via rotary evaporation yielding a white solid (~ 4 mg, 3%). ^{1}H NMR (500 MHz, $CDCl_3$): δ 5.92 (m, 1H), 5.28 (d, *J* = 17 Hz, 1H), 5.18 (d, *J* = 10.5 Hz, 1H), 3.97 (d, *J*

= 5.5 Hz, 2H), 3.68 (s, 3H), 3.43 (t, *J* = 7.0 Hz, 2H), 2.32 (m, 2H), 1.62 (m, 4H), 1.56 (br s, 14 H).

***N*-(12-dodecacarboxy)maleamic acid (2.11).** To a round bottom was added maleic anhydride (2.0 g, 20.4 mmol), 12-aminododecanoic acid (1 equiv, 20.4 mmol), and glacial acetic acid (~30 mL). The reaction went for 12 h at room temperature. The precipitate was filtered, washed with water, and recrystallized in an isopropanol/water mixture yielding a crystalline white powder (3.87 g, 61%). ^{1}H NMR (500 MHz, DMSO): δ 6.37 (d, *J* = 15 Hz, 1H), 6.22 (d, *J* = 15 Hz, 1H), 3.15 (dd, *J* = 8.5 Hz, 2H), 2.16 (t, *J* = 9.5 Hz, 2H), 1.44 (m, 4H), 1.23 (br s, 14H). ESI: M^+ calculated: 299.4; M^+ observed: 300.3.

***N*-(12-dodecacarboxy)maleimide (2.10).** Acetic anhydride (24 mL), sodium acetate (0.5 g), and **2.11** (1.5 g, 4.8 mmol) was reacted for 1 h at 90°C. The solution was washed in 5% sodium bicarbonate solution and 1M HCl, followed by triplicate ether extractions. Solvent was removed via rotary evaporation. The solid was recrystallized with hexane yielding a white powder (0.75 g, 53%). ^{1}H NMR (500 MHz, $CDCl_3$): δ 6.69 (s, 2H), 3.51 (t, *J* = 9.0 Hz, 2H), 2.34 (t, *J* = 7.5 Hz, 2H), 1.62 (m, 2H), 1.57 (m, 2H), 1.26 (br s, 14H). ^{13}C NMR (125 MHz, $CDCl_3$): δ 180.2, 171.2, 134.3, 38.1, 34.3, 29.6, 29.5, 29.4, 29.2, 29.3, 28.7, 26.9, 24.9.

2.8.3 Instrumentation

CD and Fluorescence Spectroscopy

CD spectra were obtained by using a model J-715 Jasco CD spectrometer and 1 cm cell path lengths. All samples were measured at room temperature at a concentration of 20 μmol with 100 mM NaPi, from 400–190 nm.

Fluorescence polarization experiments were done at room temperature on an ISS PC1 spectrofluorometer using the standard right-angle configuration. Excitation and emission monochromator slits were set to 16 and 8 nm, respectively. The tryptophan chromophore was excited at 280 nm. The g-factor bias was minimal and not included in the calculations.

Transmission Electron Microscopy

All samples were prepared from a 1.0 wt% gel diluted ten-fold and deposited on to a carbon coated copper grid (SPI Supplies, West Chester, PA). 1–3 μL of the diluted PA solution was placed on the carbon grid and allowed to sit for 3 min followed by wicking of any excess solution. Staining was done with 2% phosphotungstic acid (PTA) in water for 1–5 min with the grid placed carbon side down on a droplet of the staining solution, followed by wicking of any excess staining solution. After a brief wash in water, the TEM samples were air-dried at room temperature for at least 3 h before imaging. A Hitachi H-8100 TEM instrument was used with an acceleration voltage of 200kV.

Rheology

The mechanical stiffness of PAs was quantitatively measured by using oscillatory rheology using a Paar Physica Modular Compact Rheometer (MCR) 300 (Graz, Austria). All gel samples were prepared by mixing a PA sample 1:1 with a 200 mM NaPi buffer on the stage of

the rheometer at room temperature (20°C), and before measurement, allowed to rest for 10 min in a humid chamber to prevent water evaporation. A 25 mm parallel plate configuration was used with a 0.5 mm gap. Before each frequency sweep, a strain amplitude sweep was done from 3% to 100% to determine the linear viscoelastic region of the gel, which is the region the rheological properties of the samples are independent of the applied strain. The frequency sweep parameters were 100–0.1 rad s^{-1} using a strain amplitude of 3%. The storage (G') and loss (G") were recorded and all experiments were done in triplicate at the minimum.

Gel Permeation Chromatography

GPC was done on a Waters 515 GPC using THF solvent. Wavelengths 220 and 240 nm were monitored in 35 min programs run at room temperature.

2.8.4 Supplementary

Table 2.3. Mass spectrometry values of purified PAs **1–6**.

PA	Mass Expected	Mass Observed
1	1369.61	1368.49
2	1369.61	1367.77
3	1922.45	1919.90
4	1922.45	1923.09
5	1754.13	1753.42
6	1754.13	1756.34

Table 2.4. Mass spectrometry values of crude PAs **7–11**.

PA	Mass Expected	Mass Observed
7	1244.69	n/a
8	1466.89	1468.13
9	1173.62	n/a
10	991.40	n/a
11	1869.24	1869.42, 1923.10, 1077.77, 2032.09

Chapter 3: Diacetylene Peptide Amphiphiles

The incorporation of diacetylene motifs into the PA molecule, the first successful polymerizable PA in the lab, is discussed in this chapter. The introduction of this functional group within the alkyl tail of the PA molecule allows polymerization to occur within the nanofiber resulting in a colorimetric change visible by eye and monitored by spectroscopy. This chapter discusses the utility of the polydiacetylene motif as an indirect sensor for probing the interior PA nanofiber structure as well as improving the mechanical integrity of the PA material.

3.1 Introduction and Background

The polydiacetylene polymerization reaction was first discovered as a solid state reaction, yielding highly conjugated backbones. The polymerization reaction requires positioning of the atoms in a crystalline lattice with little displacement before and after the reaction, also known as a topochemical reaction.[119-122] The reaction proceeds via covalent bond formation between the C1 and C4 carbons of the diacetylenes, resulting in an eye-yne conjugated backbone (Figure 3.1). In aqueous environments, these polymers often appear red or blue colored, indicating two different degrees of conformational order from the conjugated chain, with the blue coloring indicating the most order in the conjugated π-system.[123-128] Charych[129] and Jelinek[130] have utilized polydiacetylenes (PDA) as chromatic sensors in lipid-like vesicles to detect lipid-analyte binding. Tirrell and co-workers incorporated diacetylenes into the alkyl tails of peptide amphiphiles to create polymerized vesicles[131-137] and Langmuir-Blodgett films[138] as sensitive solution-based biosensors. In the studies by Tirrell et al., cell-protein attachment disrupts the

diacetylene film or vesicle, inducing an observable color change from blue to red. Diacetylene-derivatized alkyl tails have also been contained in other self-assembling systems that form twisted nanostructures.[139, 140] Peptide amphiphiles containing diacetylenes that self-assemble into nanoribbons have also been used in magnetic alignment studies to demonstrate macroscopic

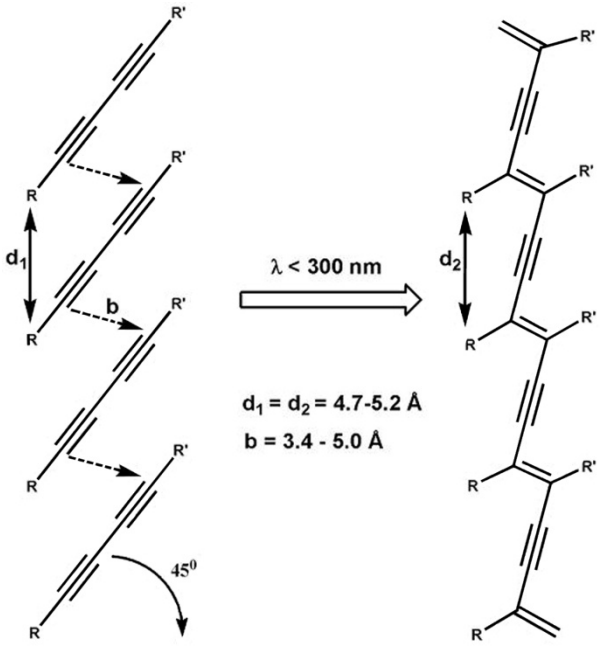

Figure 3.1. Diacetylene polymerization reaction resulting in an ene-yne conjugated chain.

ordering of the peptidic nanostructures.[118, 120] In general, the colorimetric sensitivity of the polydiacetylene conjugation, has recently become popular for biosensing and the monitoring of supramolecular structural changes.[129]

The work presented here will be incorporating diacetylene motifs into the hydrophobic alkyl segment. The polymerization of various peptide amphiphiles are studied, using polydiacetylene as a probe for the nanofiber's internal structure as well as a strategy to obtain

novel material properties. A series of diacetylene PAs composed of different sequences and length was synthesized to compare the polydiacetylene spectral differences in various PA nanofiber environments as well as differences in mechanical stiffness.

3.2 Comparison of Two Polydiacetylene PA Architectures: Linear and Branched

The synthesis of two PAs shown in Figure 3.2 contains a diacetylene functional group within a C_{25} alkyl tail. The peptide sequence of PA **12** has the linear architecture sequence of Lys-Lys-Leu-Leu-Ala-Lys-($OC_{25}H_{40}$), whereas PA **13** contains an additional lysine residue, creating its branched architecture: Lys-Lys(Lys)-Leu-Leu-Ala-Lys-($OC_{25}H_{40}$). The comparison between linear and branched PA architectures has been investigated before (see Chapter 2), suggesting branched PAs have reduced nanofiber density and increased solvent accessibility compared to its linear PA counterpart. If these observations are also consistent in diacetylene

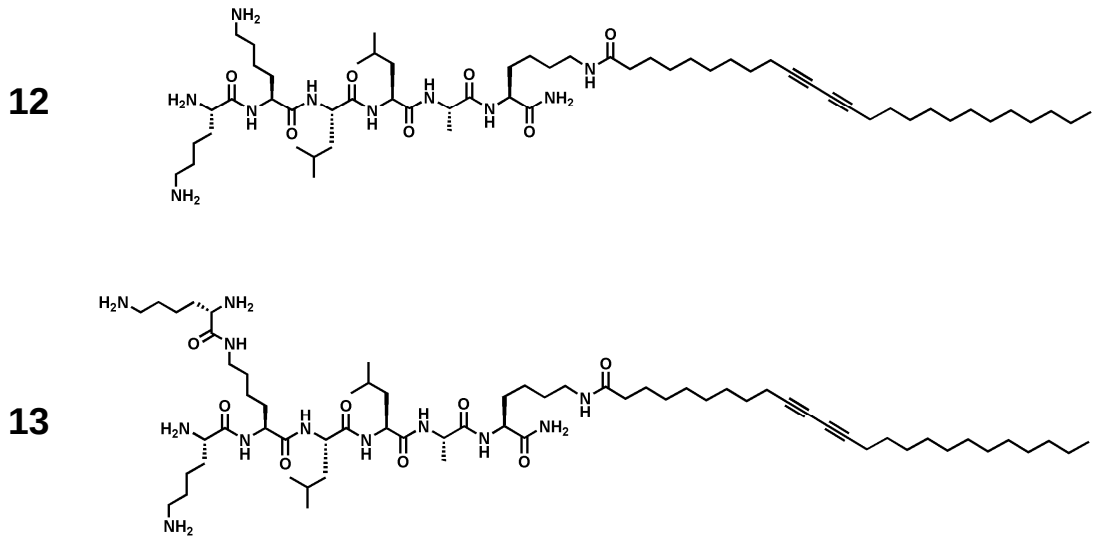

Figure 3.2. Diacetylene PAs: Linear PA (**12**), Branched PA (**13**).

PAs, one should observe reduced polymerization efficiencies for the branched PAs nanofibers.

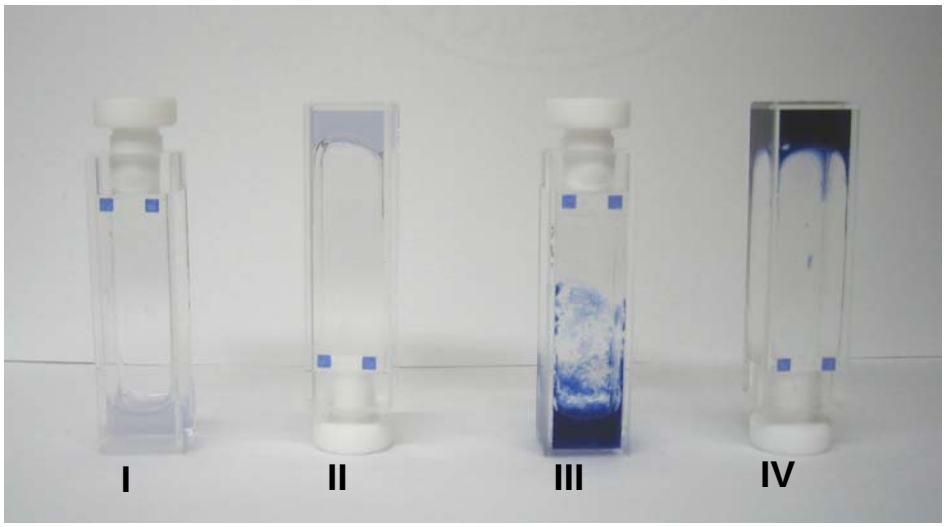

Figure 3.3. Linear PA samples from left to right: (**I**) PA solution without irradiation, (**II**) gelled PA without irradiation, (**III**) PA solution with irradiation, (**IV**) gelled PA with irradiation. Samples were irradiated for two minutes in this image. Nonirradiated samples will occasionally appear tinted blue possibly either due to polymerization from stray light or thermal excitation.

Both linear PA **12** and branched PA **13** form gels at concentrations of 2.0 wt% in water when exposed to ammonia vapor from an ammonium hydroxide solution in a sealed chamber for several minutes. Gelation occurs due to the presence of the hydroxide base, which screens the net charges on the PA molecule, encouraging nanofiber self-assembly by hydrogen bonding and hydrophobic collapse. Photoirradiation at 256 nm was performed on samples either before or after gelation. Both PA samples resulted in the well-known colorimetric change associated with diacetylene polymerization, from a colorless to an intense blue color (Figure 3.3). As seen in cuvette III in Figure 3.3, photoirradiated samples without exposure to gelation conditions also polymerize, indicating that PA aggregates exist even in solution without net charge neutralization. The irradiation of PA solutions changes color to a dark blue-purple, whereas

irradiation of the gel results in an intense blue color (IV in Figure 3.3). The blue-purple color suggests the presence of both conformationally disordered (red) and ordered (blue) states in the PDA backbones formed. Irradiation of the branched PAs under the same conditions resulted in similar color changes. After polymerization, the PA gels also appeared more mechanically robust relative to nonirradiated gels. From these initial observations, both linear and branched PAs seemingly have sufficient internal order to support the topotactic polymerization of diacetylenes in their hydrophobic core. Since diacetylene polymerization is a topotactic reaction, the color change due to backbone conjugation can be correlated to the degree of molecular ordering in the reactive assemblies. This degree of ordering should be compromised by high curvatures in nanostructures, and in fact the blue color indicative of long effective conjugation lengths was not observed in spherical micelles by several systems.[141] For nanostructures with planar assemblies, such as large bilayer vesicles (70–150 nm) seen in work by Tirrell et al.,[142, 143] a blue color following diacetylene polymerization was observed. It is therefore interesting that in our nanoscale cylindrical assemblies with high curvature (5–8 nm) photoirradiation results in an observed blue color. This suggests a high degree of internal order in the cylindrical nanostructures formed by the βPAs studied here.

3.2.1 Spectroscopic Analysis of Nanofibers

As previously mentioned, polydiacetylenes (PDAs) show colorimetric changes switching between blue to red when their conjugated backbones are perturbed from ordered to less ordered conformations, respectively. External factors such as temperature and solvent can perturb the

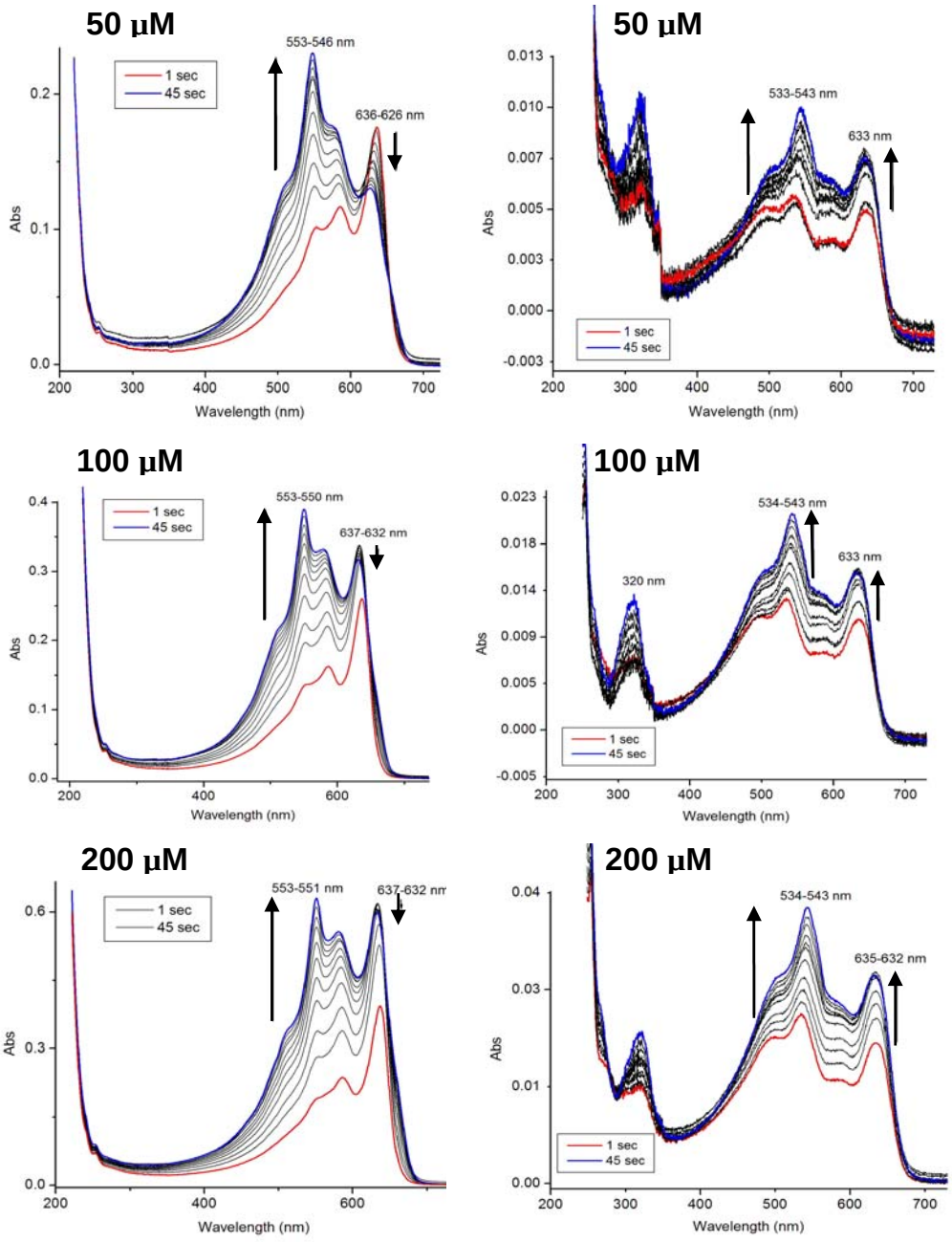

Figure 3.4. Time-dependent UV spectroscopy of linear (**left**) and branched (**right**) PAs at varying concentrations. Samples were monitored in 5 s time-intervals. for 45 s. The spectra also show data of 1 and 3 s after irradiation.

polydiacetylene backbone. We utilized UV−vis spectroscopy and CD to monitor diacetylene absorption bands differences within a series of PA molecules after irradiation.

PA solution concentrations of 50, 100, and 200 μM were monitored by UV−vis absorption for a total of 45 s as shown in Figure 3.4. For the spectra of both **12** and **13**, two major absorption peaks are observed near 530 nm and 630 nm, representing the red and blue states, respectively, which we attribute to two the two different PDA conformation states. The band observed at 550 nm for PA **12** appears to be mostly attributed to the red state with superpositioning of the 585 blue band causing a slight shift to longer wavelengths compared to the 540 band observed for PA **13**. The presence of ordered and disordered states in both the linear and branched PA spectra is clearly revealed in these spectra. After several seconds of continued irradiation, the intensity of the blue state band decreases and that of the red state band increases. Ultimately, even as samples continued to be irradiated for a total of 2 min, the rapid decrease of the band at 630 nm tends to be coupled with the growing band at 550 nm. The increase of the red state at 550 nm suggests that the continued polymerization of the polydiacetylenes results in an increased level of disorder in the polymer backbones formed. This has also been observed in monolayers reported by Evans et al.[144] demonstrating that extended UV exposure time decreases the effective conjugation length of PDA chains. It should be noted that similar absorption changes with irradiation was observed for PA gels that were diluted to the concentrations stated at the beginning of this section. Compared to linear PA **12**, the UV−vis spectra of branched PA **13** show significantly lower absorption. Because both PAs are known to self-assemble into fibers, this suggests that diacetylene alkyl tails in the branched PA nanofibers are less efficiently ordered to support diacetylene polymerization. At lower intensities, a band at

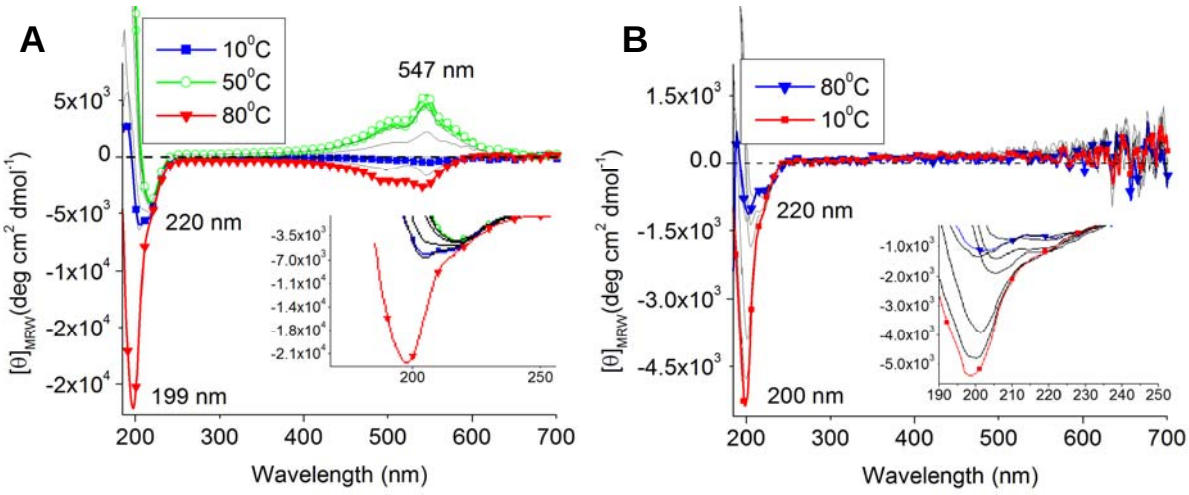

Figure 3.5. Temperature-dependent CD spectroscopy of linear PA **12** before (**A**) and after (**B**) irradiation. Samples were monitored from 80°C–10°C and irradiated for 2 min.

320 nm can be observed in the branched PA, which we assign potentially as an exciton absorption peak as characterized by Weiser and co-workers.[145] The reduced order of the branched PA is believed to be the result of less efficient packing within the nanostructure due to the steric crowding from the branched peptidic segment.

Temperature-dependent CD experiments were initially performed to ensure that the β-sheet structures, which help drive PA nanofiber formation, were still present after photoirradiation. The β-sheet band at 220 nm was observed both before and after irradiation, implying that polymerization does not completely disrupt the hydrogen-bonded structures (Figures 3.5 and 3.6). Even at 80°C, the 220 nm band is still present, although markedly reduced in intensity. Random-coil bands are also observed at 200 nm possibly due to limited PA aggregation from the low concentration used (100 μM).

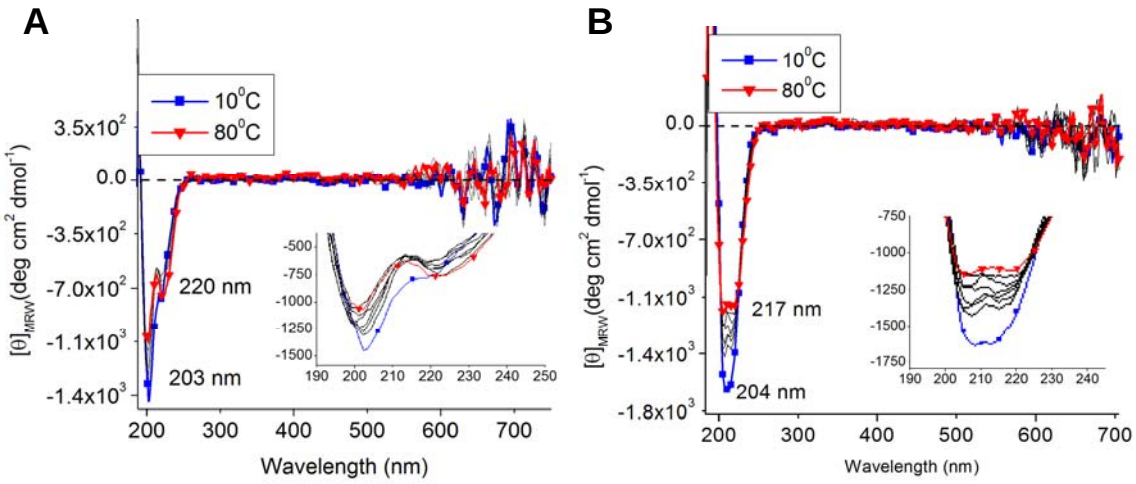

Figure 3.6. Temperature-dependent CD spectroscopy of branched PA **13** before (**A**) and after (**B**) irradiation. Samples were monitored from 80°C–10°C and irradiated for 2 min.

Interestingly, a polydiacetylene PA band at 547 nm was observed in photoirradiated samples of PA **12**. (Figure 3.5B) This was not expected as this portion of the molecule is not intrinsically chiral. Deb and co-workers have also shown that hydrogen-bonded, achiral assemblies containing the PDA do not display a CD signal, but substitution of chiral side groups result in an induced polydiacetylene CD signal.[146] Figure 3.5 shows temperature-dependent CD spectra of non-irradiated and irradiated PA solutions at 100 μM concentrations. The signal of 547 nm was not detected in the non-irradiated samples and correlates with the formation of the PDA in the core of the nanofibers. Further analysis of the CD spectrum (Figure 3.5B) shows the PDA band changes sign at 80°C from its maximum negative intensity to a positive intensity at 50°C, then decreasing again to a negative intensity at 10°C. While the interpretation of the unusual CD signals in the PDA region is still unclear, this may result from the spectral combination of exciton coupling from the diacetylene poymer[147] combined with the induced CD

signal from the adjacent β-sheets. It should be noted that β-sheets are known to twist naturally in a helical fashion[139] causing a chiral induction upon the PDA backbone. The chirality of the PDA region is expected to depend more on the chemical sequence of the β-sheet than the overall peptide length, assuming a longer sequence does not disrupt the self-assembled β-sheets within the nanofiber. Coincidentally, the preferred distance between diacetylene monomers is similar to the distance between hydrogen bonds of parallel β-sheets (~ 5 Å). Mori et al. have studied polymerization of diacetylene monomers using a β-sheet template showing that the polymerization occurs parallel to the hydrogen bonds.[148] The strong CD band at 547 from the irradiated linear PA not only shows that the PDA is in a chiral environment, but suggests that the β-sheets are twisted within the nanofibers. Also, the induced chiral structure of the conjugated backbone is not in immediate proximity to the β-sheets, confirming that structural ordering can extend even to the alkyl tail.

For branched PA **13** there is no observable CD signal for the PDA backbone. (Figure 3.6) This observation together with the low UV−vis absorbance intensity shows a clear structural difference between the interior core of the branched (**13**) and linear (**12**) PA assemblies. The packing geometry of the branched PA inhibits the polymerization reaction. Figure 3.7 shows an idealized model of the PDA (red) backbone following the twisting of the β-sheet (blue).

The CD signal changes observed at 547 nm for the polymerized PA nanofibers suggest a structural relationship between the PA β-sheets and the polydiacetylene. At 80°C, when the β-sheet is destabilized and partly denatured, the PDA conformation appears to change as evidenced by a change from a positive CD signal at room temperature to a negative CD signal, implying structural reorganization with the PA assemblies. Unlike the spectrum of the nonirradiated PA,

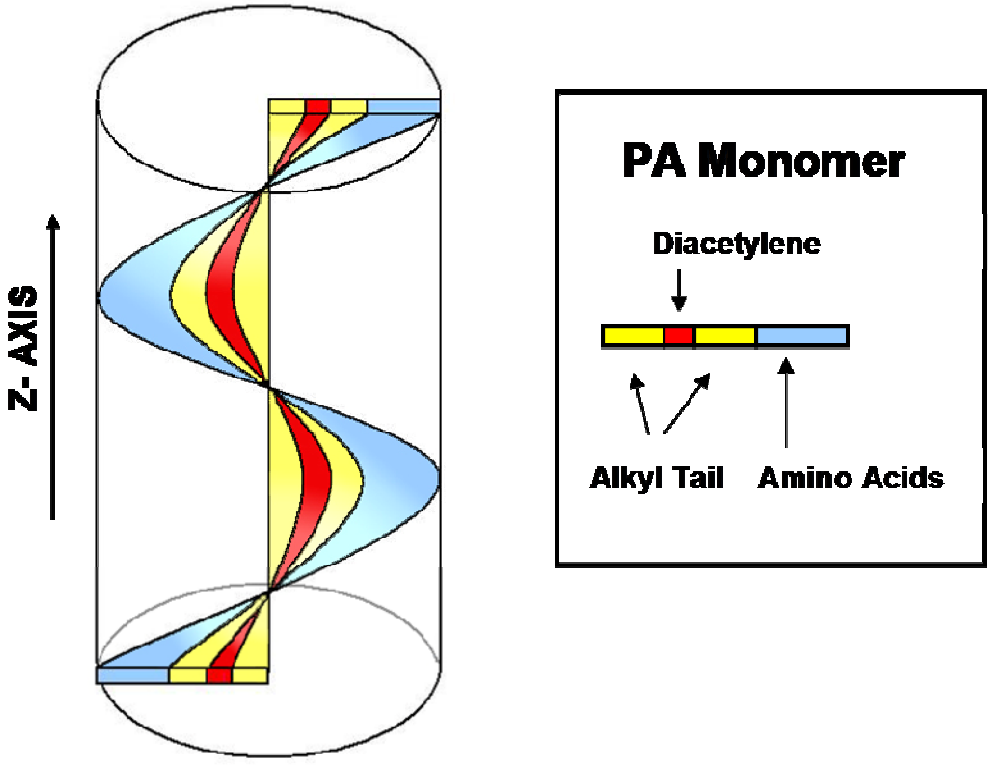

Figure 3.7. A proposed three-dimensional model of the PA nanofiber. Polymerization of the diacetylene (red) occurs along the *z*-axis of the fiber following the directionality of the beta-sheet (blue).

which shows a diminished random-coil signal, the irradiated PA spectrum shows the random-coil signature from peptidic segments to be dominant at high temperatures. The presence of the random-coil at high temperatures for the irradiated samples is possibly due to the PDA polymer preventing the reorganized PA structures from disassembling. As the temperature decreases, the hydrogen bonds of β-sheets re-form and the PDA conformation adjusts to accommodate the β-sheet structure. As samples are cooled, the sign of the CD signal at 547 nm also changes. The reason for this sign reversal is not clear, but one may speculate that the details of β-sheet structures (e.g., the nature of peptide folding) after heating and then cooling to room temperature may be different. The annealed nanofibers containing conjugated backbones may be equilibrated to a new internal structure in which β-sheets and PDA establish a different chiral environment. The dominance of β-sheet structures in the nanofiber assemblies at room temperature is clear as their CD signal at 220 nm becomes more prominent at lower temperatures. Interestingly, temperature-dependent CD experiments of the branched PA **13** showed no significant different before and after irradiation. Both β-sheet and random-coil bands at 220 and 200 nm, respectively, were present at high temperatures for both irradiated and nonirradiated branched PA spectra.

3.2.2 Microscopic Imaging

TEM was performed on both PA **12** and **13** before and after irradiation to observe morphological changes. The micrographs are shown in Figures 3.8 and 3.9. Both samples are composed of long nanofibers with diameters in the range of 5 to 8 nm. There was no detectable change in their diameters before and after irradiation, indicating that the topochemical reaction

does not alter fiber morphology. Additional micrographs were taken on polymerized linear PAs at pH 2, 4, 7, 10, and 12. Polymerization of 1 wt% samples at all of these pH values resulted in blue colored materials. TEM images of the nanostructures showed similar diameters in the range of 5 to 8 nm and morphologies for all of the samples. (PA **12** in Figure 3.10)

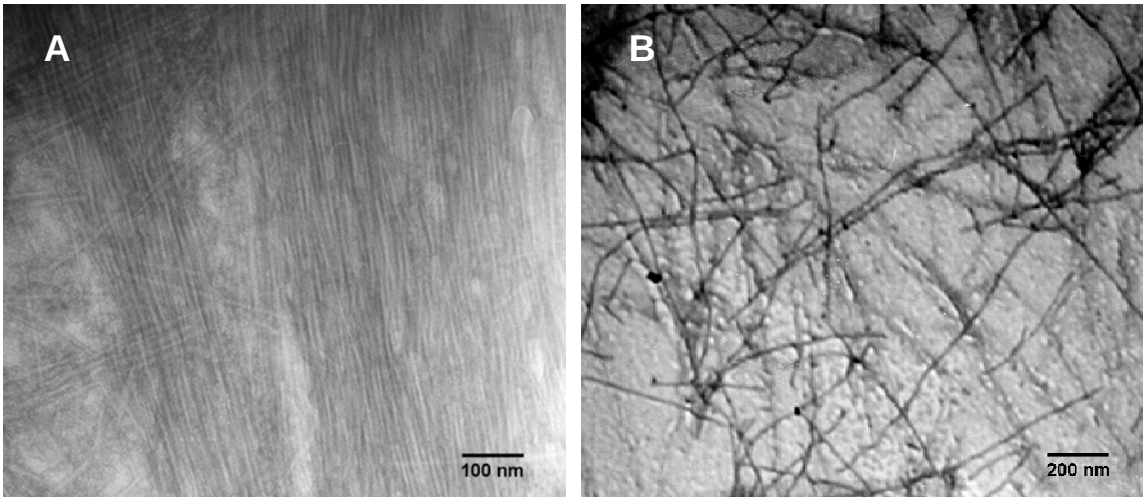

Figure 3.8. TEM images of linear PA **12**: nonirradiated (**A**) and irradiated (**B**). Samples were stained with phosphotungstic acid for approximately 1–3 min. Irradiated samples were exposed (256 nm) for 2 min.

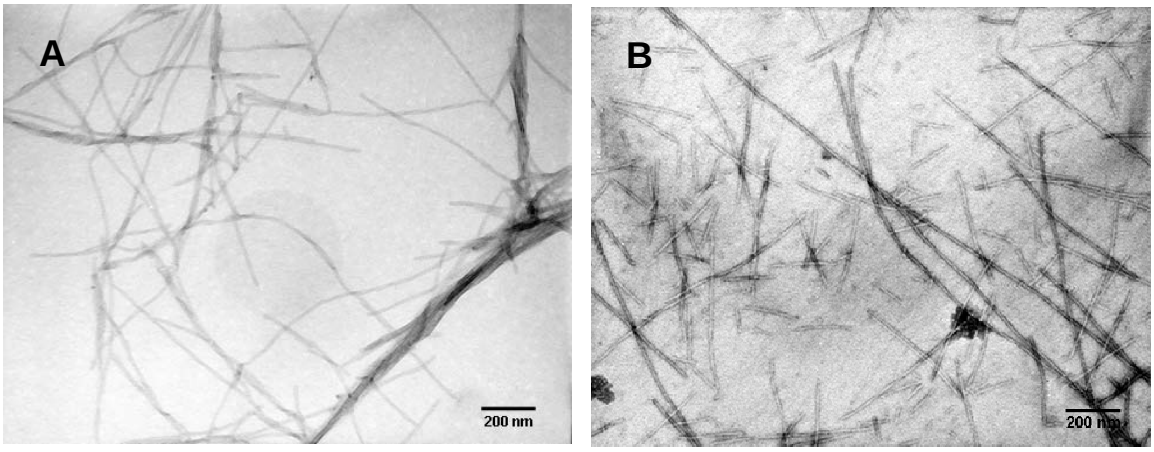

Figure 3.9. TEM images of branched PA **13**: nonirradiated (**A**) and irradiated (**B**). Samples were stained with phosphotungstic acid for approximately 1–3 min. Irradiated samples were exposed (256 nm) for 2 min.

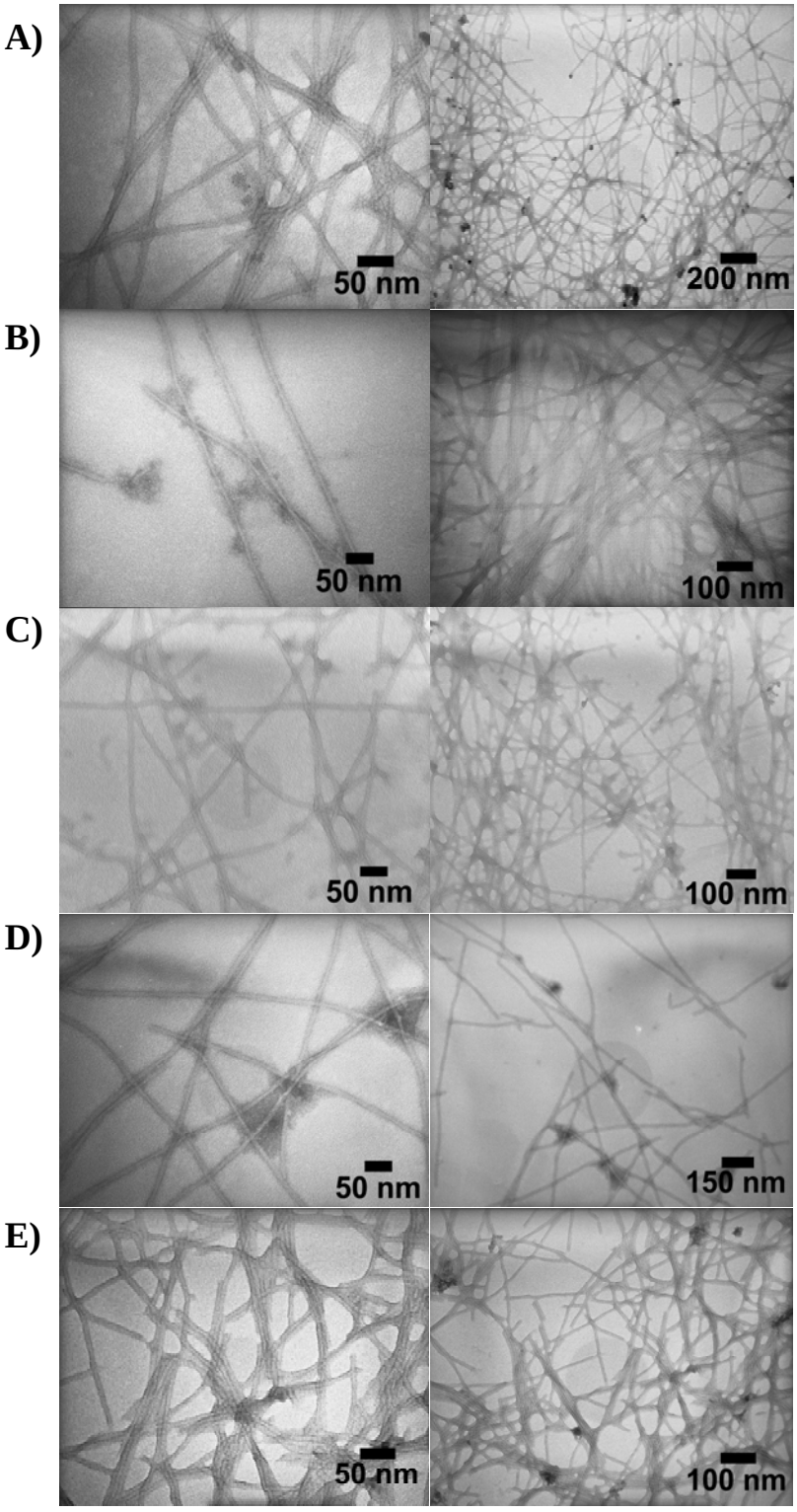

Figure 3.10. TEM of Linear PA **12** at varying pHs. (**A**) pH 2 (**B**) pH 4 (**C**) pH 7 (**D**) pH 10 (**E**) pH 12.

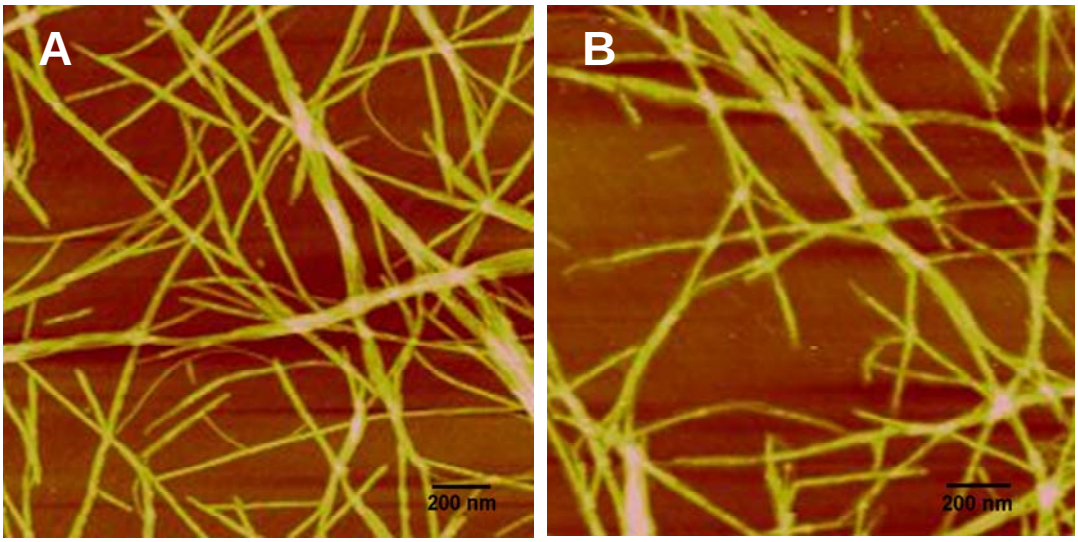

Figure 3.11. AFM height profiles of linear PA **12** nonirradiated (**A**) and irradiated (**B**). Samples were drop-casted and imaged on silicon substrates after 2 min of irradiation.

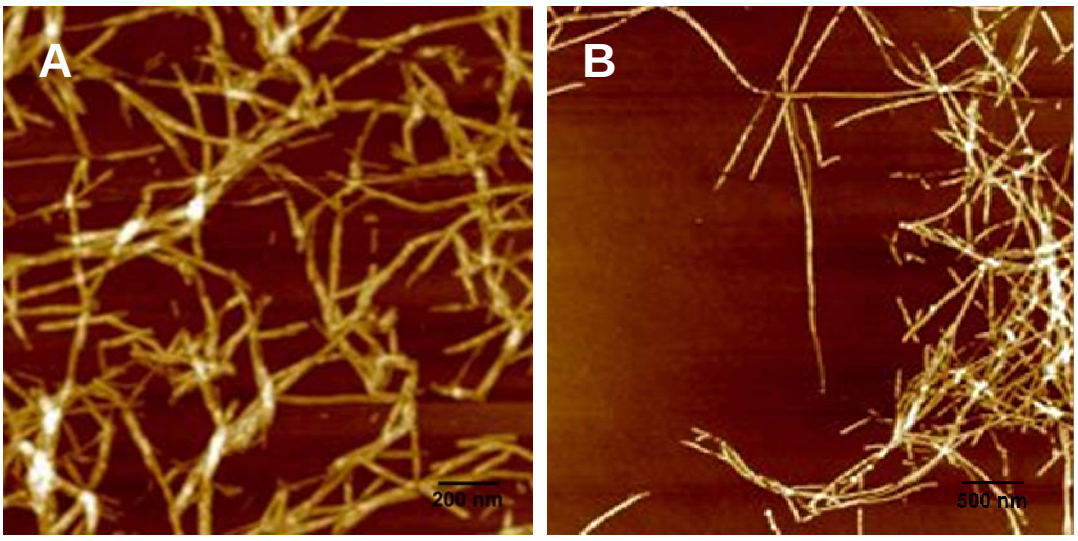

Figure 3.12. AFM height profiles of branched PA **13** nonirradiated (**A**) and irradiated (**B**). Samples were drop-casted and imaged on silicon substrates after 2 min of irradiation.

Atomic force microscopy (AFM) was also used to examine the nanostructure morphology. The AFM of PA **12**, both irradiated and non-irradiated, revealed nanofibers with heights of approximately 5 nm and microns in length (Figure 3.11). In the images of the PA **13**, (Figure 3.12) nanofibers were also observed before and after photoirradiation. Although both formed fibers, the nanofibers of PA **13** compared to PA **12** appeared more aggregated with shorter fibers possibly due to less efficient packing among PA molecules which may affect nanofiber stability.

3.3 A Brief Comparison of Polydiacetylene PA Nanofibers

The initial studies on the diacetylene polymerization demonstrated the success of polymerizing both linear and branched PA architectures as well as the usefulness of having the PDA act as a structural probe within a PA nanofiber. The polymerization efficiency monitored by UV−vis shows significantly better polymerization for linear PAs than branched PAs due to greater internal ordering which suggested the importance of the peptide sequence. Therefore we investigated changes in: i) a different β-sheet forming region or ii) having the same β-sheet segment, but a different sequence length. In these studies, diacetylene polymerization is utilized as an indirect method to observe the structural nanofiber packing differences between PAs with different sequences. This degree of structural analysis with our PA nanofibers has not been done until now. It should also be noted that a portion of this work was contributed by Jaime Stasiorowski, a summer assistant working in our lab through the NSF−RET program..

3.3.1 β-Sheet Formation and Diacetylene Polymerization

As previously shown, the packing of a linear PA nanofiber which is dictated by hydrophobic collapse and β-sheet formation appears to create a chiral environment for

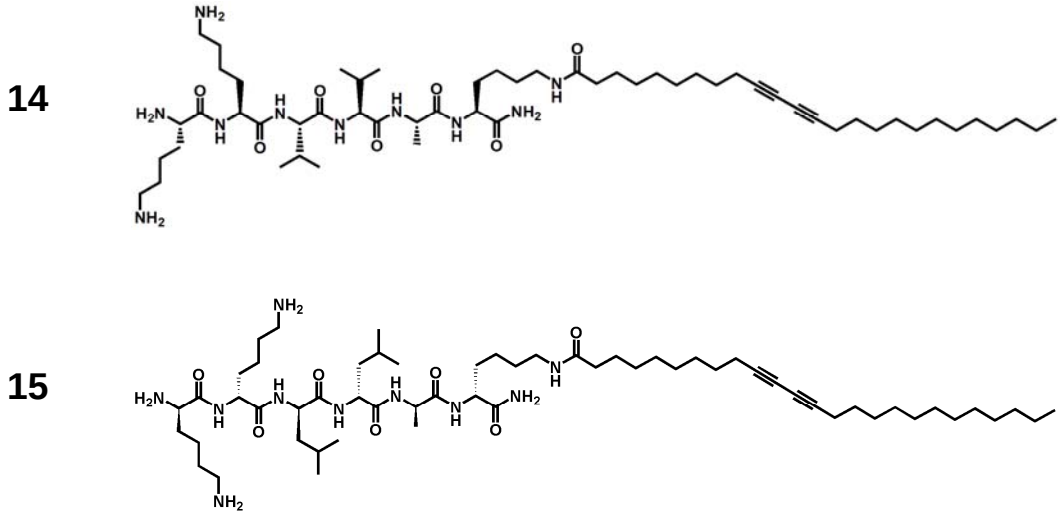

Figure 3.13. Diacetylene PAs containing the β-sheet sequence: Val-Val-Ala (**14**) or *d*-Leu-*d*-Leu-*d*-Ala (**15**).

polymerization of diacetylenes, observed by CD. The β-sheet sequence of those PAs consisted of Leu-Leu-Ala, which prompted the query of whether polymerization would occur in all linear peptide amphiphiles. To better understand the relationship between the PDA and its nanofiber environment, PA **14** and **15** were synthesized containing a different β-sheet region Val-Val-Ala or *d*-Leu-*d*-Leu-*d*-Ala, respectively (Figure 3.12). PA **15** is the right-handed isomer of PA **12**.

Both PAs form self-supporting gels when exposed to basic conditions at 1 wt%. When photoirradiated, the PA gels immediately became dark blue and prolonged irradiation resulted in a dark blue-purple gel, also observed with the diacetylene PAs described previously. This suggests that the interior of these relatively short peptide sequences of these PAs are ordered enough to facilitate the diacetylene reaction. Time-dependent UV−vis spectroscopy monitoring the PDA absorption showed the presence of both red and blue PDA conformation phases at 553

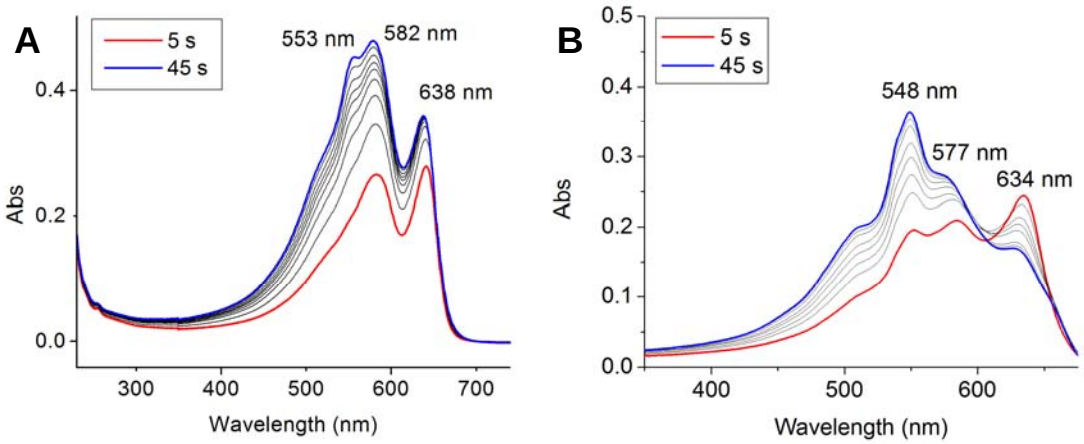

Figure 3.14. Time-dependent photoirradiation of diacetylene PAs containing the β-sheet sequence: **A**) Val-Val-Ala (**14**) or **B**) *d*-Leu-*d*-Leu-*d*-Ala (**15**) by UV–vis spectroscopy.

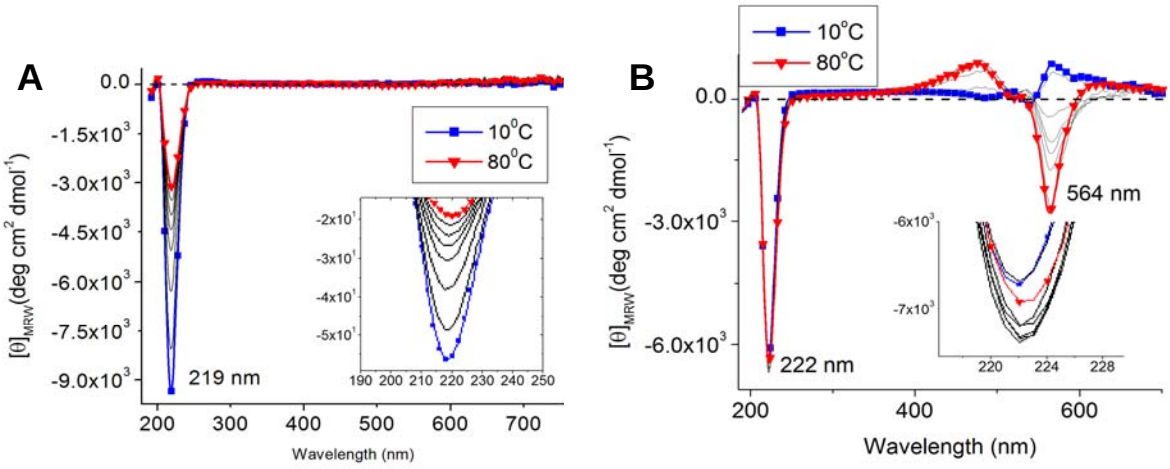

Figure 3.15. Temperature-dependent CD spectra of PA **14** at 200 μM. **A**) non-irradiated sample. **B**) 2 min irradiated sample from 10–80°C.

nm and 638 nm, respectively (Figure 3.14). With prolonged irradiation, the blue phase at 638 nm is shown to decrease with continual increase of the red phase, also observed in previous diacetylene PAs. Although both samples are at 100 μM, the differences in the relative peak shape between PA **14** and **15** demonstrate the sensitivity of the PDA reaction as well as the different PDA backbone conformations present in the solutions. It should be noted that if the solution samples are aged and unintentionally polymerized by ambient light, the samples will show similar band peaks, but the intensities will be inconsistent compared to unaged samples. To maximize these sample consistency, the samples were always prepared and photoirradiated immediately prior to experimentation.

Temperature-dependent CD of PA **14** and **15** showed no PDA signal of non-polymerized samples, as expected. After 2 min of photoirradiation, PA **14** exhibited a strong, broad PDA signal at 550 nm (Figure 3.15B). Upon heating, the CD signal becomes inverted, changing sign, also observed in previous work with PA **12** while the β-sheet signal at 220 nm remains relatively unchanged. When the sample is cooled and reheated, the same trend is observed. This change of CD signal with temperature is possibly due to the changes in PA aggregation and bundling. A recent finding by Weiss et al.[149] also showed similar inversion of PDA CD spectra as the aggregation states of their oligopeptide-polymer polydiacetylene system changed. In their system, trifluoroacetic acid is used to disperse their helical aggregates, which is monitored by CD and microscopy. When comparing the CD β-sheet signal of the polymerized versus non-polymerized with increasing temperature (Figure 3.15A), the secondary structure is less sensitive to temperature when the PDA is present, demonstrating enhanced thermal stability. The CD spectrum of PA **15** (Figure 3.16) also shows a similar signature to PA **14** however at a much

greater intensity. Because it is a PA comprised of *d*-amino acids, the nanofiber's β-sheets have a positive signal at 217 nm. The CD intensity of the polymer is also significantly greater than the β-sheet. The decrease of the 217 nm band at higher temperatures may be attributed to the chiral-induced polymer destabilizing the β-sheet.

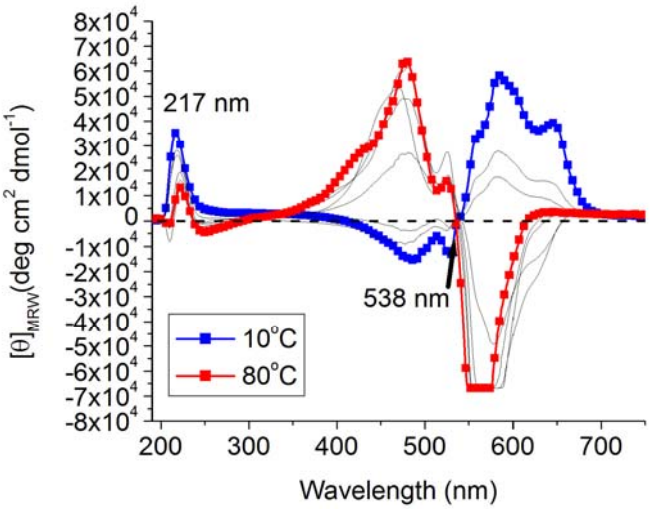

Figure 3.16. Temperature-dependent CD spectra of PA **15** after 2 min photoirradiation from 10–80°C.

As previously stated, varying salt concentrations in a PA solution could likely result in a different PDA conformation after polymerization. Between two different synthetic batches of PA **14**, there was a significant difference in the CD spectrum, but not the UV–vis spectra (Figure 3.17). This was initially surprising, as to why one batch would yield a PDA CD signal (Figure 3.17B), but not the second batch after multiple repeated experiments and molecular confirmation. Following the recent work by Weiss and co-worker, they demonstrated the addition of TFA appeared to suppress the CD signal of the PDA supramolecular systems. This

provided one explanation regarding our contradicting observations, since some TFA salts can remain in the sample after resin cleavage and post work-up. Fluorine NMR did show the presence of TFA in both samples, however there was significantly more TFA in the second batch than the first. For future experiments, dialysis of the PAs or the use of TFA scavengers should be tested.

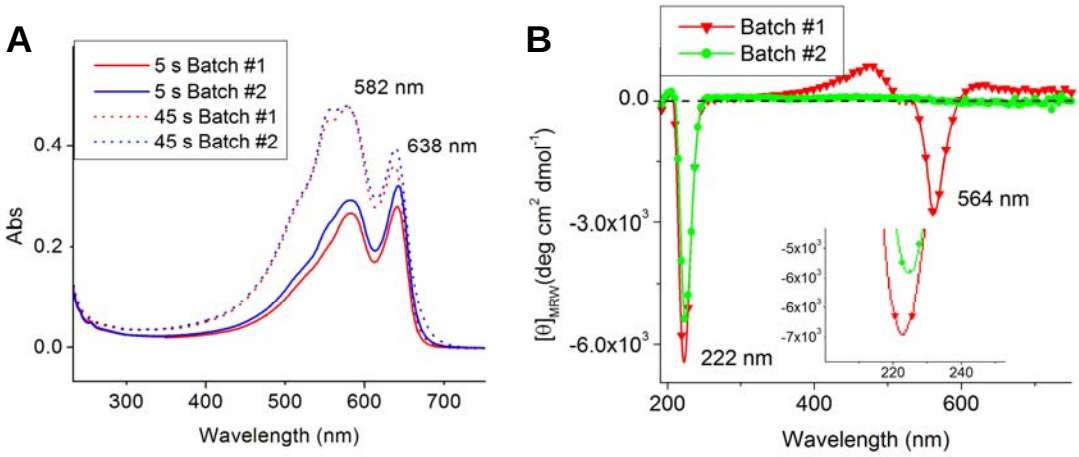

Figure 3.17. Overlay of 2 synthetic batches of PA **14**. **A**) UV−vis spectrum overlay of batch 1 and 2 after two time-points of photoirradiation. **B**) Overlay of CD spectra of PA **14**, batch 1 and 2, after 2 min photoirradiation at 80°C.

AFM microscopy showed no change in the heights or morphologies of PA **14** and **15** before and after photoirradiation. This coincides with previous diacetylene PA observations, reinforcing the fact that the reaction is topotactic (Figure 3.18). Occasional bumps and textures can be observed on the fibers, but they do not appear to be consistently helical or to have regular periodicity.

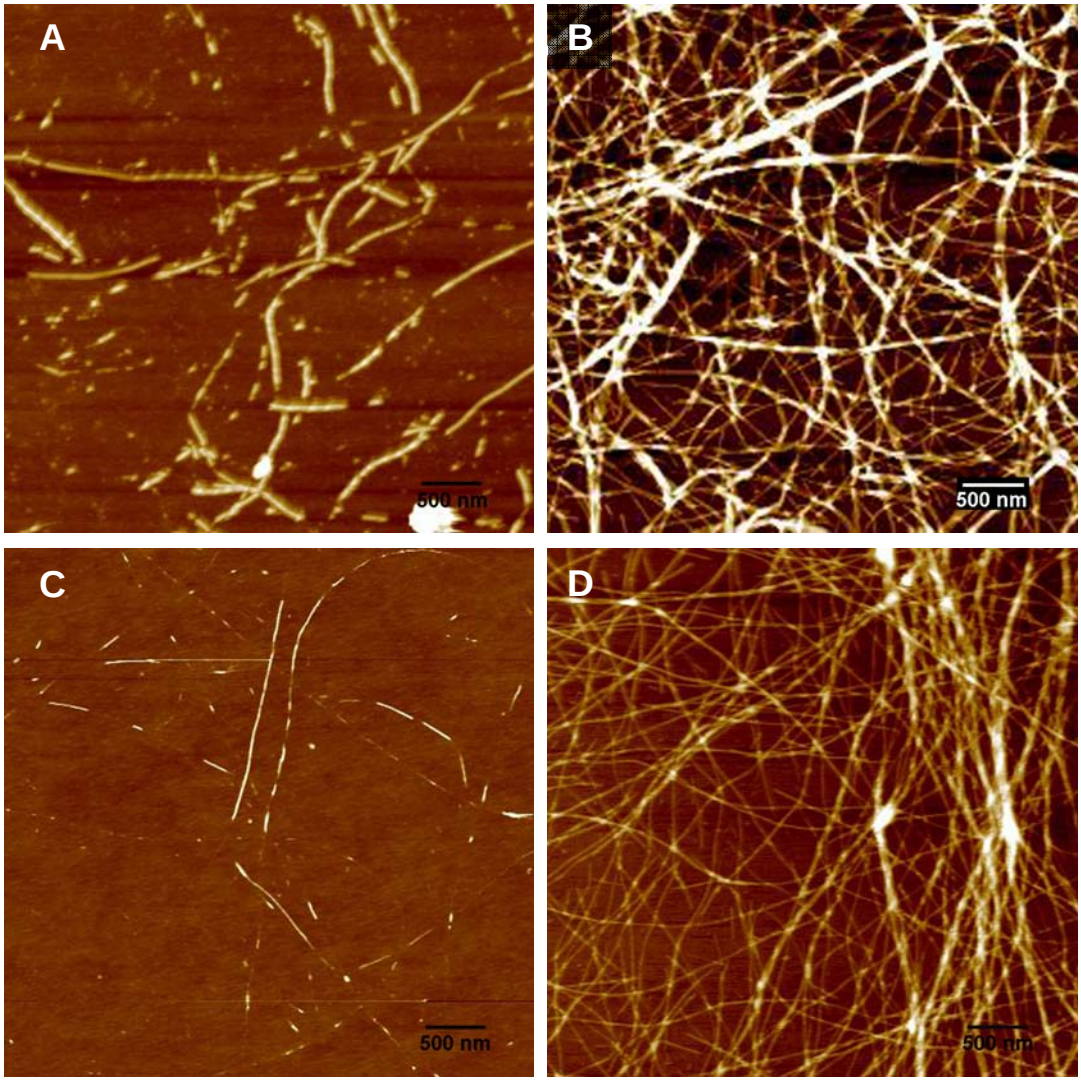

Figure 3.18. AFM of PA **14 A**) non-irradiated and **B**) irradiated. PA **15 C**) non-irradiated and **D**) irradiated. Samples were diluted from a 1 wt% gel and drop-casted on to a clean silicon substrate. Images **A**,**C**, and **D** were taken by Jaime Stasiorowski.

3.3.2 *Sequence Length and Diacetylene Polymerization*

Varying residues within the β-sheet segment has been shown to permit diacetylene polymerization with some variations in the relative peak intensities, suggesting the PA interior structure to be changeable and complex. We also investigated the effects of varying the length of the peptide sequence while maintaining the β-sheet forming sequence and alkyl tail for comparison purposes. PA **16** was synthesized containing the extended sequence (Figure 3.19), Arg-Gly-Asp-Ser-Gly with a Leu-Leu-Ala β-sheet region analogous to PA **12**. As a proof-of-concept, this extended sequence was chosen to be a bioactive epitope, commonly used to induce cellular adhesion.

The addition of residues in a self-assembled PA increases the opportunities for further secondary structure formation as well as increased steric repulsion between the added residues. The addition of enough peripheral residues will perturb the β-sheet and the internal ordering of the PA nanofiber. UV−vis spectroscopy of PA **16** shows the PDA spectrum monitored after every 5 s of photoirradiation. Compared to the previous linear PA molecules analyzed in this chapter, PA **16** shows a nearly three-fold decrease in absorption intensity, which is interpreted

16

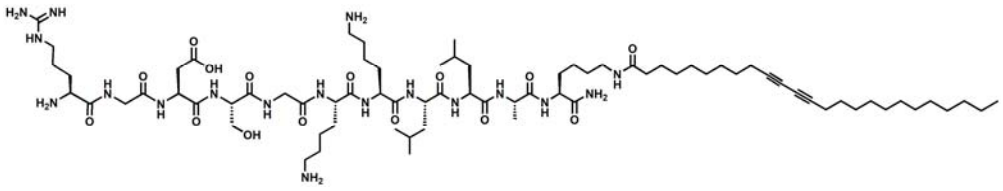

Figure 3.19. Diacetylene PA **16** with the sequence, RGDSGKKLLAK with a diacetylene alkyl tail.

as reduced polymerization efficiency. Photoirradiation of PA **16** was also monitored in methanol to observe whether further disruption the β-sheet would affect the polymerization efficiency (Figure 20B). In methanol, photoirradiation of the solution led to formation of a pink solution, also indicated in UV–vis spectrum by the diminished presence of the blue phase band at 634 nm as well as a two-fold reduced absorption intensity compared to photoirradiation in water. The decrease in absorption intensity and red phase band having the greatest intensity (~540 nm) suggests a more disordered, less polymerizable nanofiber.

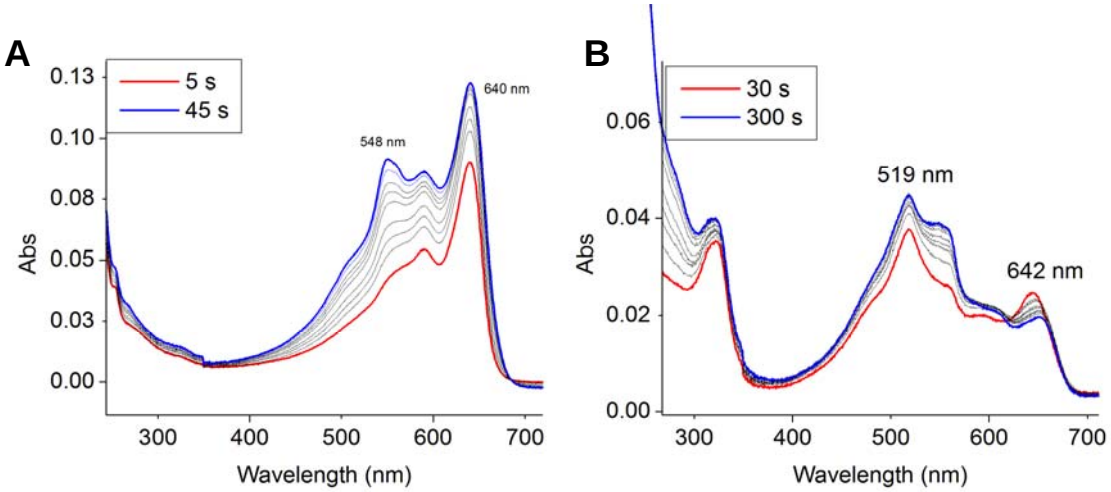

Figure 3.20. UV–vis spectra of PA **16** at 100 μM concentrations in **A**) water and **B**) methanol. Photoirradiation of the samples were done in five second increments followed between each spectrum measurement.

The CD spectra of PA **16** in either a water or methanol solvent were also monitored. Without irradiation, only the β-sheet band at 220 nm was observed. Because the initial PDA intensity at 100 μM was minimal the concentration was increased to 200 μM (Figure 2.21).

Similar to the trend observed in the UV−vis data, the PDA CD signal is reduced compared to previously observed linear PA signals in water. In methanol, it was interesting to see that although the β-sheet band at 227 nm was weaker than the fiber assembly in water, the PDA signal intensity remained relatively similar between the two solvents. Conformation of the

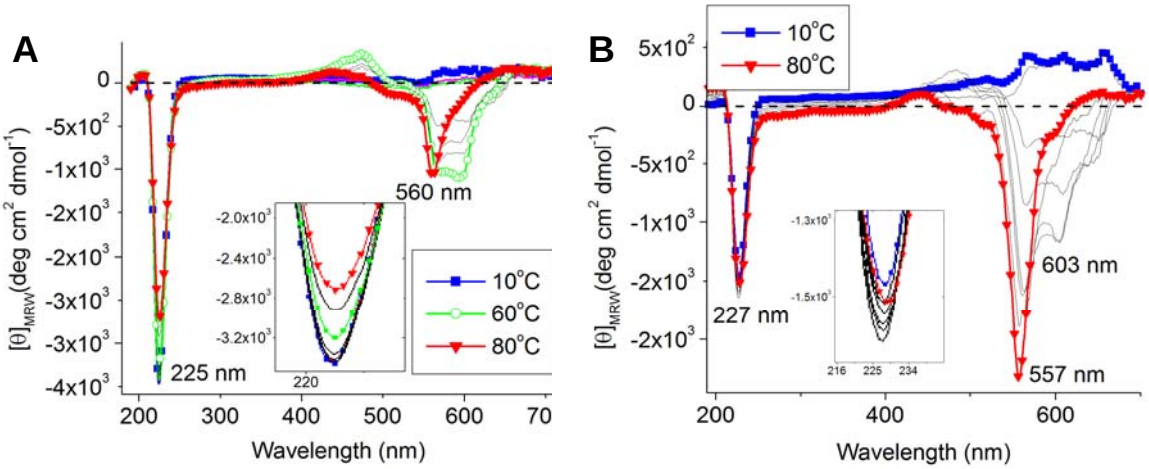

Figure 3.21. Temperature-dependent CD spectra of PA **16** at 200 μM concentrations in **A**) water and **B**) methanol. Spectra were collected in 10 degree increments from 10–80°C.

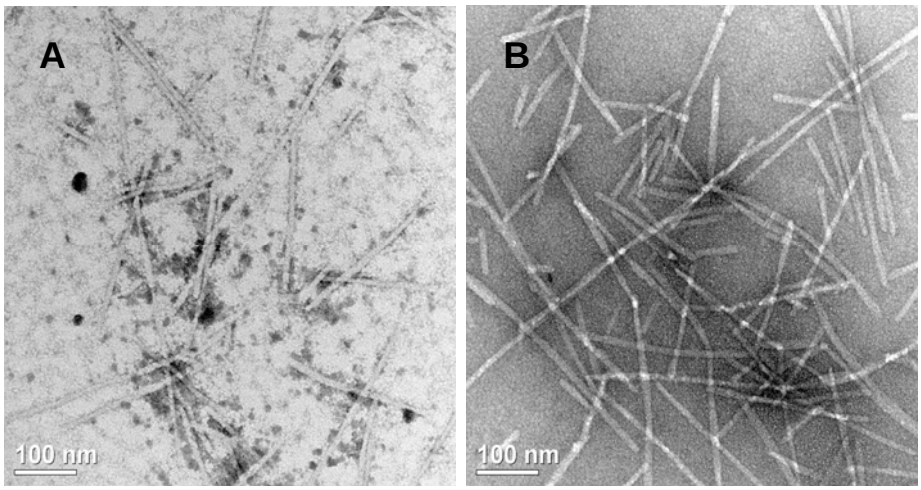

Figure 3.22. TEM micrographs of PA **16**. **A**) nonirradiated **B**) irradiated for 2 min. Samples were stained with uranyl acetate.

presence of nanofibers before and after photoirradiation was done by TEM (Figure 3.22). Measurement of the fiber diameter was found to be 8–12 nm and several hundred nanometers long. No morphological differences were observed, as expected after polymerization.

From this study, we conclude the extension of the peptide sequence by five residues causes a significant decrease in spectroscopic intensities, most likely due to reduced polymerization. The presence of blue and red phase conformations shows there are both ordered and disordered conformations present from the polymers that were able to form. Future studies regarding the fine balance between sequence length and the structure-stabilizing β-sheets can be fine tuned using diacetylene as an internal structural probe.

3.4 Mechanical Testing

The mechanical analysis of PA gels is challenging because oftentimes the materials are either too stiff or inhomogeneous for microrheology, which measures the thermal motion of small particles embedded in the material of interest, or too soft and below the detection limits for indentation experiments. The materials characterization of the diacetylene PAs was complicated by the need to shield the light sensitive material until the photoirradiation step. Three methods being drop shape analysis, mechanical indentation, and oscillatory rheology were attempted with the objective of obtaining consistent storage and loss moduli while using the least amount of sample. Oscillatory rheology appears to be the most promising methodology, currently, having the capability of measuring within the viscoelastic range of the diacetylene PAs. Along with oscillatory rheology, the two other methods will be briefly discussed.

In the attempt to characterize the mechanical behavior of the diacetylene PAs, a collaboration was forged with the Shull lab for drop shape analysis[150, 151] with Daniel Carvajal. The drop shape analysis involved monitoring the change in the PA droplet shape when brought into contact with a PEO polymer–chloroform mixture while immersed in a solution of water. The changes in drop shape allow measurement of the interfacial pressure changes as well as stiffness of the drop, as long as the polymer–chloroform stiffness value is known. Unfortunately, both nonphotoirradiated and photoirradiated PA drops of PA **12** were too stiff for the polymer–chloroform mixture. It is worth noting that the polydiacetylene PA after irradiation seems more hydrophobic based upon its semi-adherent interaction with the polymer–chloroform layer. This behavior, however, was not observed in the nonirradiated PA drops.

The second mechanical method involved indentation tests[152] in collaboration with Michelle Seitz also in the Shull lab. Indentation tests were done using a flat cylindrical indenter lowered into contact with the gel using a piezoelectric motor.[153] The load and displacement data were collected simultaneously using a load transducer and an optical displacement sensor. The gels were prepared in a teflon mold that had diameters ranging from 4–6 mm with a height of 2.5 mm, which were subsequently compressed by the indenter instrument between two glass plates (Figure 3.23). Although stress and strain values were obtained, the data was not consistent between molds of the same PA sample. This could be attributed to several factors, particularly variations in sample preparation and possible drying affects despite our best attempts to reduce evaporation by keeping the molds in damp containers before measurements. Due to the softness of the gels, detaching the gel from the teflon mold resulted in minor surface defects. Because the conversion calculations assume full radial contact between the gel sample and the cylindrical

punch, these minor defects could have contributed towards the inconsistent results. Once the PA solutions were placed in to the molds ranging from 1–4 wt%, they were gelled by exposing the samples to ammonium hydroxide vapors followed by photoirradiation. Incomplete diffusion of the vapors through the gel and the potential lack of UV irradiation exposure while the gel was in the mold may also have caused inhomogenity within the gel. Although this technique is highly useful for stiff materials and requires little sample, it was not able to yield a consistent mechanical response from the PDA PAs.

The third mechanical testing method attempted with the best results was oscillatory rheology. Oscillation rheology measurements were done to monitor the mechanical response of PAs using a Paar Physica Modular Compact Rheometer provided by the Burghardt laboratory.

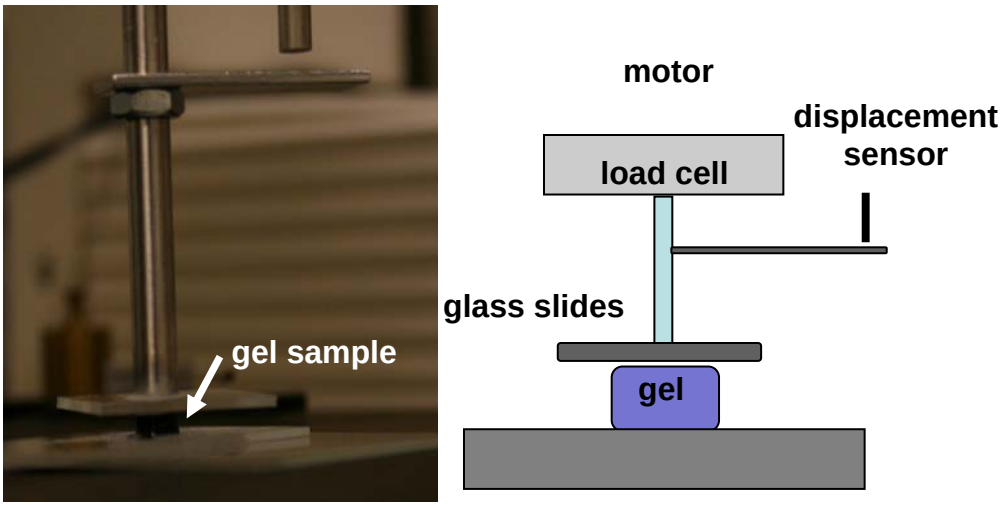

Figure 3.23. Indentation instrument used to measure the mechanical response of diacetylene PAs. (*Images were provided by Michelle Seitz in the Shull laboratory and modified.*)

Sample preparation was optimized by determining: the best gelation reagent, preventative steps to reduce evaporation, and the most convenient method for polymerization. Gels are typically prepared using vapors from a solution of ammonium hydroxide, but the corrosive vapors combined with the inability to transfer the PA gel on to the rheometer plate required a different gelator. Sodium phosphate was found to be best suited in forming PA gels for rheology experiments compared to other salts such as hydroxide salts. Mixing the PA solution with the

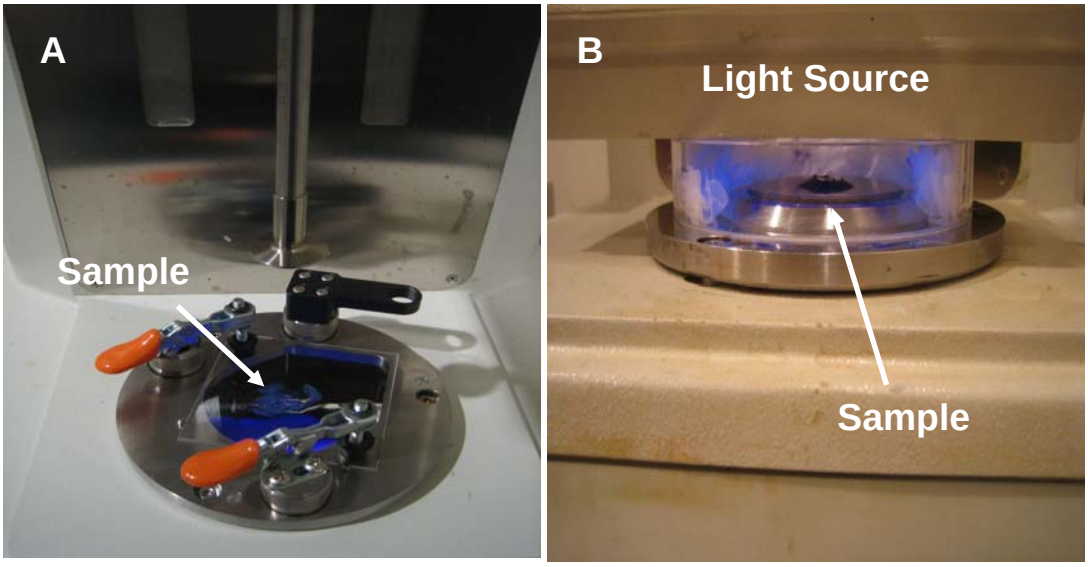

Figure 3.24. Rheology instrument set-up for UV irradiation. **A**) Light source is placed below the parallel plates. **B**) Light source is sandwiched between the parallel plates on top of the water chamber and the samples are irradiated prior to the mechanical measurements.

buffer solution on the rheometer plate resulted in rapid gelation. To prevent evaporation, either a water chamber or mineral oil placed around the sample were tried. Rheology experiments using oil showed no differences before and after photoirradiation of the materials, due to slippage of the bulk material between the plates. The water chamber seemed the best suited to reduce evaporation, when using the stainless steel rheometer plate. Two instrumental set-ups to

incorporate a UV source for photoirradiation were attempted (Figure 3.24). The first method involved replacing the stainless steel base with a transparent quartz plate, and positioning the UV lamp under the plates. The second set-up had the light source placed inbetween the plates, permitting UV irradiation before rheology measurements. This latter set-up appeared to be optimal, based upon the closer distance of the UV source and the usage of the water chamber, which could not fit on to the first set-up. All irradiated samples were exposed for 2 min followed immediately by the rheology experiment.

The rheology results of photoirradiated and nonphotoirradiated linear PA **12** are shown in Figure 3.25 displaying both storage and loss moduli at a sweep from 0.1–100 s^{-1} in angular frequency. Both PA samples display their storage modulus (G') to be greater than their loss modulus (G") with little change throughout all the observed data points, indicating its gel-like behavior until the angular frequency drops below 50 s^{-1} for the non-irradiated sample. If G" ≥ G', the loss in the elastic modulus suggests the material as more liquid-like. This appears to only occur in non-irradiated samples for PA **12** and not polymerized samples, which suggests the polymer does play a role in stiffening the gel material. This loss in gel character does not occur for all diacetylene PAs, unsurprisingly, since the stiffness of PA gels also depends on its amino acid sequence. An arbitrary point was chosen (50 s^{-1}) to compared the moduli results from both non-irradiated and irradiated samples of the 3 PA, PA **12**, **14**, and **16** (Figure 3.26). Comparison of the G' values of the 3 PAs shows the storage moduli data to be greater after polymerization while the G" values are always less than G', showing the materials maintain their elastic behavior. The material with the greatest G' value, PA **14**, contains the Val-Val-Ala β-sheet segment unlike PA **12** and **16**, which have the Leu-Leu-Ala sequence. This suggests that PAs

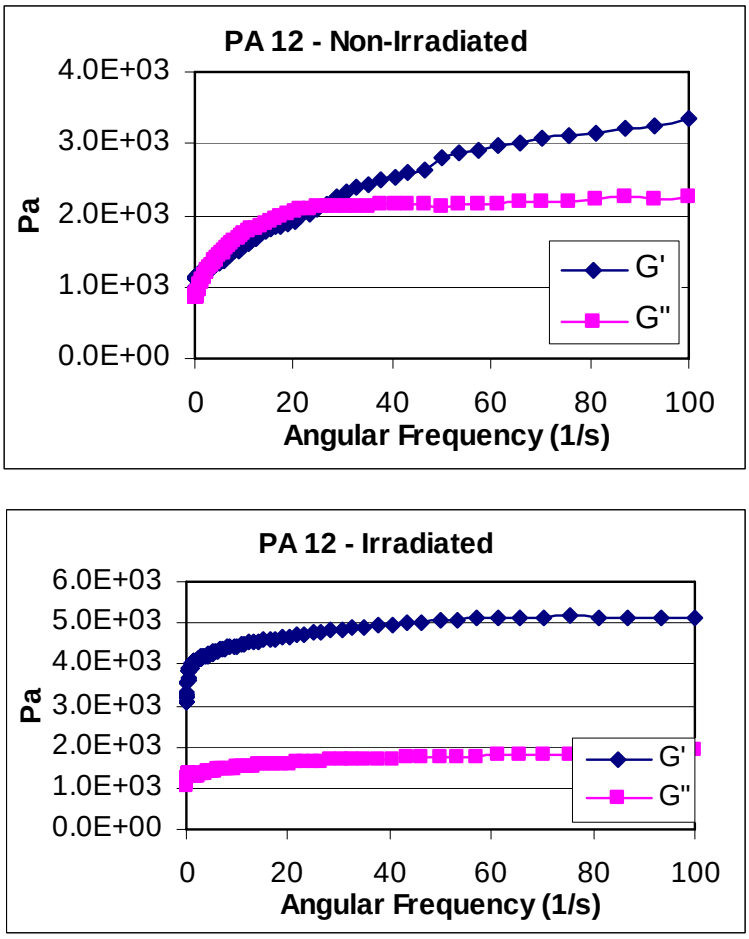

Figure 3.25. Rheology measurements of PA **12** nonirradiated (**top**) or irradiated (**bottom**). G' > G" through the frequency range reflects typical gel mechanics. The constant strain was held at 0.8%. The irradiated sample shows a greater storage modulus (G') value than the nonirradiated sample, demonstrating enhanced mechanical stiffness. For the *y*-axis, 'Pa' refers to Pascals.

containing sequential valine residues, which have a strong propensity to form β-sheets, also yields in potentially stiffer materials. A longer peptide sequence such as PA **16**, may interfere with the formation of a stiff gel by weakening the β-sheet secondary structure. The storage modulus of PA **16** is observed to be less than its shorter length counterpart, PA **12**.

The mechanical testing of several diacetylene PAs showed the correlation between sequence and material stiffness and more importantly, that diacetylene polymerization leads to stiffer materials. In this study, both the drop analysis and indentation tests did not work for characterizing the diacetylene material, but they could be potential alternatives for the mechanical measurements of other PAs.

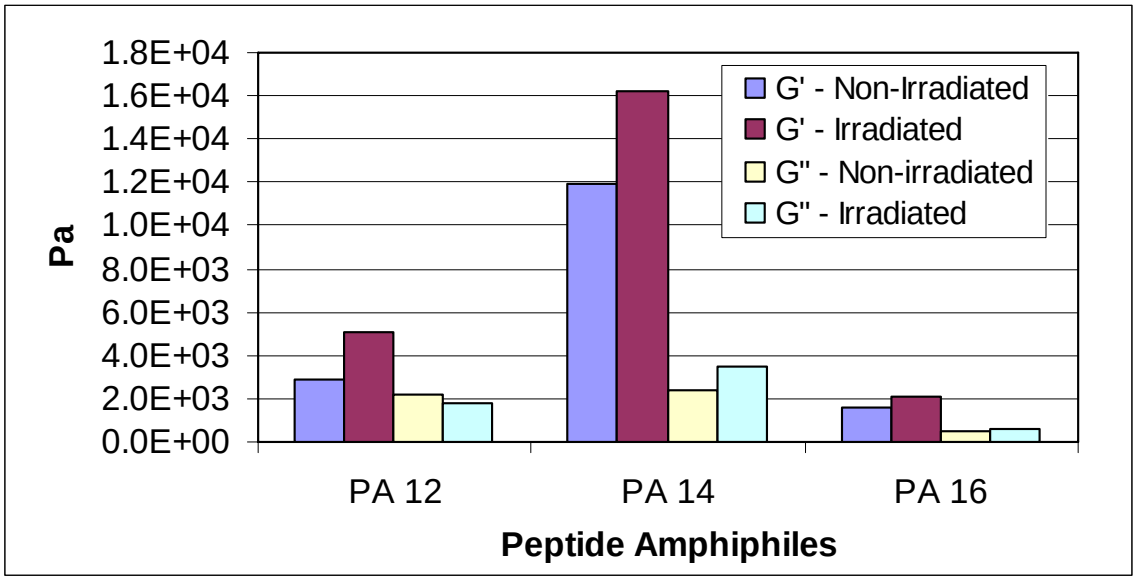

Figure 3.26. Rheology summary of linear PA data. PA **12** is 6-mer containing the Leu-Leu-Ala segment. PA **14** is a 6-mer containing the Val-Val-Ala segment. PA **16** is an 11-mer containing the Leu-Leu-Ala segment. The graph includes G' and G" moduli of both irradiated and non-irradiated samples. For the *y*-axis, 'Pa' refers to Pascals.

3.5 Micropatterning and Biological Applications

The synthesis and characterization of these materials led to applications as biomaterials. The patterning of these bioactive materials holds great interest because of the abundant *in vivo* and *in vitro* studies already done using gel solutions. By controlling both micro- and nanotextures, this offers the possibility of further controlling cellular behavior and its directionality. Previous peptide amphiphiles did not yield materials robust enough for 3D micropatterning. However, the creation of diacetylene PAs enabled the first successful 3D patterning of PA substrates for cellular-growth applications.

3.5.1 Sonication-Assisted Solution Embossing (SASE)

Soft lithography is relatively inexpensive and can be done over large areas under milder conditions compared to other patterning methods such as electron-beam lithography.[154] One method of soft lithography attempted in this study was already proven successful in patterning noncovalently linkable PAs. The SASE technique was developed in the Stupp lab by Hung et al.,[155] utilizing the combination of self-assembly, nanofiber alignment, and patterning over a large area using an elastomeric stamp. The alignment of the one-dimensional nanofibers is achieved through sonication of a solution that is confined in the stamp pattern. Once the solvent has completely evaporated, the stamp is removed to reveal the pattern. Using this technique, Hung and co-workers were able to demonstrate long-range order of PA nanofibers that were able to align in channels and even those with sharp corners.

The preparation of the elastomer stamp before attempting the SASE technique was possible with the help of Josh Goldberger. The original mask needed to create the stamp was

designed and created by photoetching the desired pattern, using a photoresist, onto a silicon wafer. All pattern dimensions and films were determined by profilometry using a Tencor P10 profilometer. The master mold was used to make patterned poly(dimethylsiloxane) (PDMS) with dimensions of approximately 1.4 μm in width by 1.2 μm in height and channel lengths several hundred microns long. A more robust stamp was prepared with the assistance of Ian Tevis, following a protocol by Odom et al.[156, 157] to make a composite stamp using a stiffer PDMS (h-PDMS) first cast upon the surface of the master mold, further supported with a thick layer on top using soft PDMS. After the PDMS stamp was separated from the master mold, it was cleaned in a mixture of isopropanol and acetone followed by a water wash. The actual PA patterning was done by placing a PA solution onto a clean glass substrate. The PDMS stamp was placed on top of the solution and a weight was placed upon the stamp to evenly distribute the pattern transfer. The set up was then sonicated to align the nanofibers. After 12 hours, the stamp was removed and the pattern was analyzed.

PA **12** was patterned into micron-sized channels and then photopolymerized (Figure 3.27). The width of the lines was measured to be approximately 1.4 μm. The samples were also placed under cross-polarized light using a Laborlux 12 Pol optical microscope attached to a Sony-XT-ST 70 CCD camera. Under the microscope, the pattern appears mostly birefringent suggesting alignment of the polydiacetylene fibers, as expected. The birefringence is caused by the anisotropic refractive index created by the alignment of the nanofibers. Figure 3.23C shows the loss of the birefringence as the cross-polarizers were turned at a 45° angle.

The patterning of diacetylene PAs using the SASE technique shows that covalently linkable PAs may be patterned from solution inside the confinement of microchannels. Future

directions for this project would be initial cell culture experiments using the PA aligned substrates with the objective of directing cell growth with bioactive substrates that are patterned across multiple length scales.

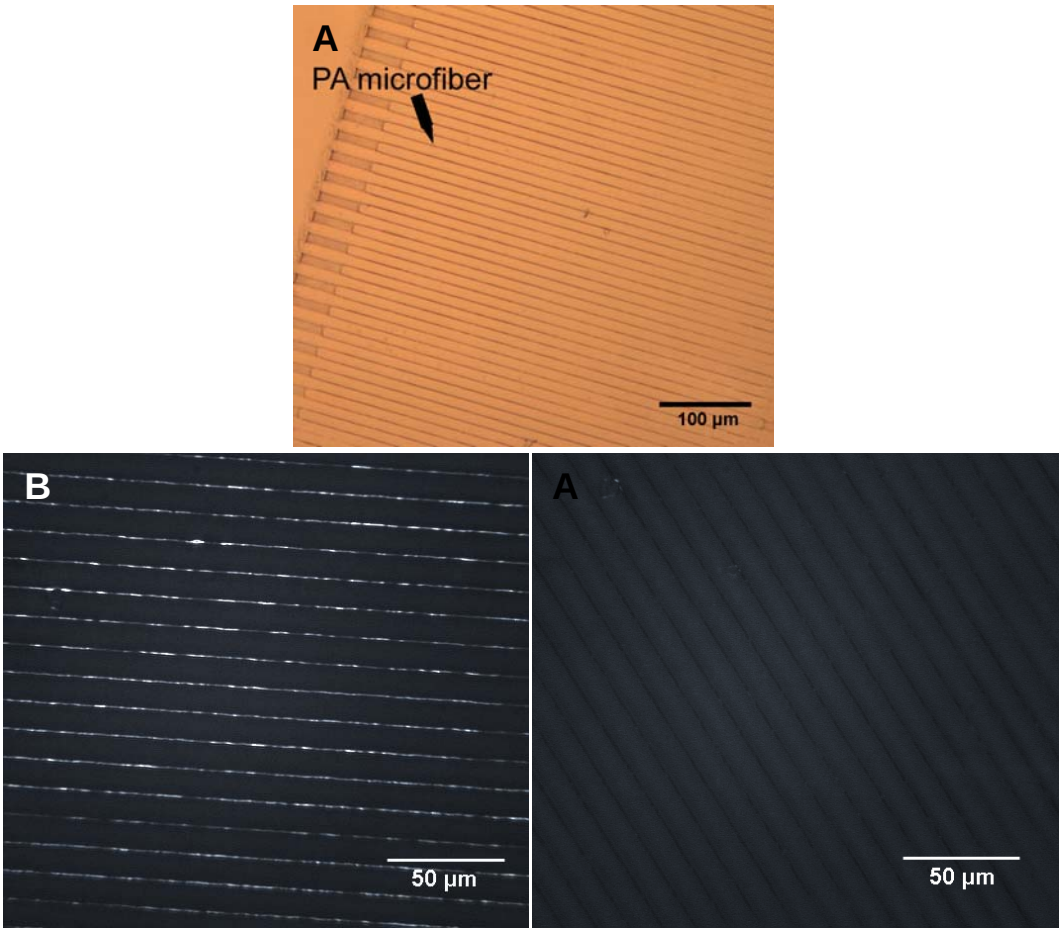

Figure 3.27. SASE stamping results with PA **12**. **A**) Normal photograph of PA lines after stamping. Lines measure to be approximately 1.4 µm. **B**) PA pattern under cross-polarized light. **C**) PA pattern under cross-polarized light turned 45°.

3.5.2 3D Micropatterning

The design and synthesis of a mechanically robust, polymerized PA system enabled the microfabrication of hierarchical structures using diacetylene PA materials. This type of top-down patterning has not been possible with previous generations of peptide amphiphiles. This is especially important in the field of tissue engineering and regenerative medicine, since the biomaterials play a key role influencing growth and programming desired cellular behavior. It is well known that cellular behavior is affected by the confines of its environment, including surface stiffness and surface topography.[158] The ability to control topographical features within nano- and microlength scales and the incorporation of specific bioactive chemistry could add another level of control over cellular activity.

PA **12** and PA **17** were incorporated into the microfabrication process (Figure 3.28). PA **12** was used in this application as a filler molecule containing no bioactive epitope in order to increase the accessibility of PA **17**, which contains the RGDS epitope but is otherwise the same sequence as PA **12**. The microfabrication and cellular studies were done by Alvaro Mata, also in

17

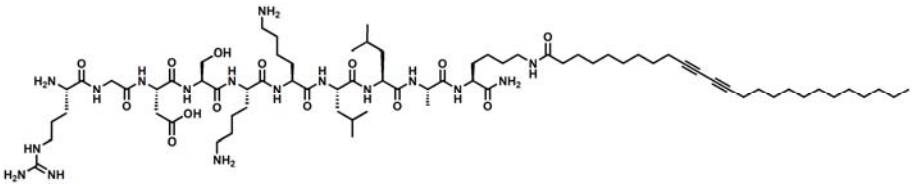

Figure 3.28. Diacetylene PA **17** containing the bioactive epitope, RGDS.

the Stupp laboratory. The microfabrication was done using ~1 mm thick PDMS molds of different patterns. Compared to the SASE technique, this method of fabrication is not limited to

2D PA patterning but can generate three dimensional up to micron-sized topographical features.[159] Cellular studies were done by A. Mata to investigate the effects of varying topographical patterns on human mesenchymal stem cell (hMSC) differentiation into osteoblastic phenotypes. The fabricated patterns examined include 8 μm deep holes and channels 10–40 μm in diameter (Figure 3.29). Figure 3.30 shows SEM images of the cells in contact with the various microtextures. The cells cultured on the channel pattern favored alignment parallel to the

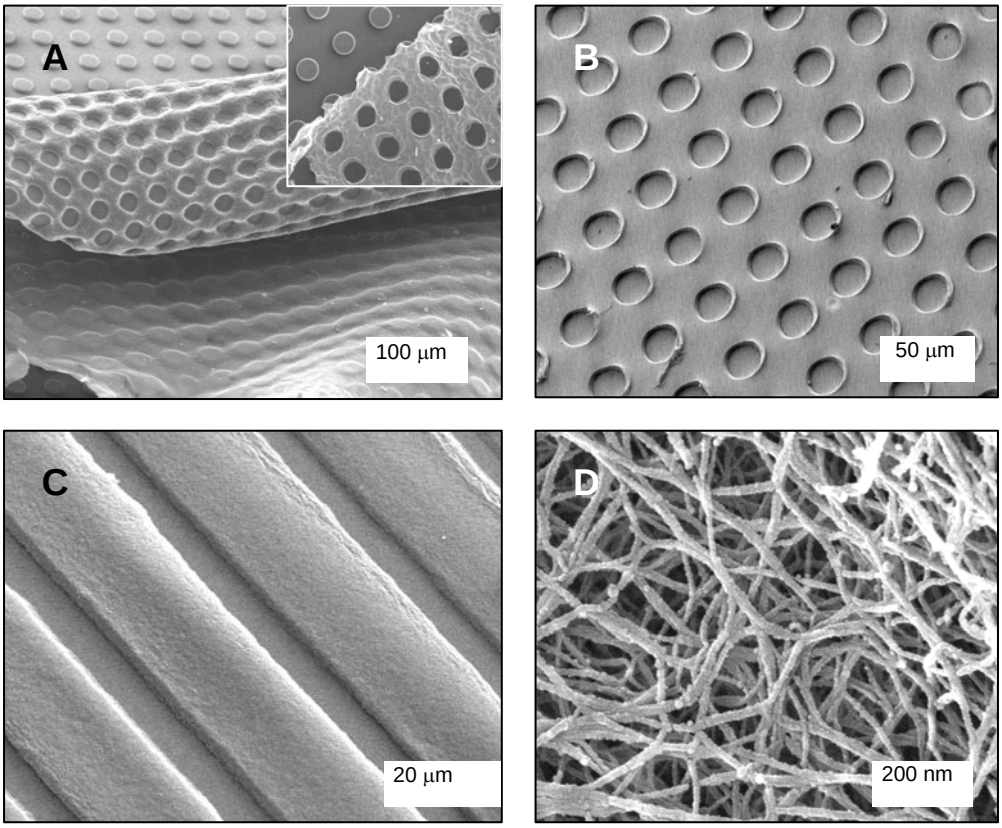

Figure 3.29. SEM images of the microfabrication of polydiacetylene PAs. **A**) A rolled, patterned sheet of PDA PA that has been lifted off its silica substrate. **B**) A pattern of wells 8 μm deep and 10 μm in diameter. **C**) A channel pattern 8 μm deep and 10 μm in diameter, separated by 20 μm. **D**) A magnified image of the fibers within the patterns showing a complex network of bundled fibers.

channel, while the cells appeared to prefer confinement within the wells. Certainly, not all cells behave may behave identically, thus similar work with these materials may be required for the optimizations of other cell types. Based upon the present work here, it has been shown that polydiacetylene PAs are the first PAs to be successfully microfabricated and cultured with hMSCs, demonstrating cell viability on such patterned substrates.

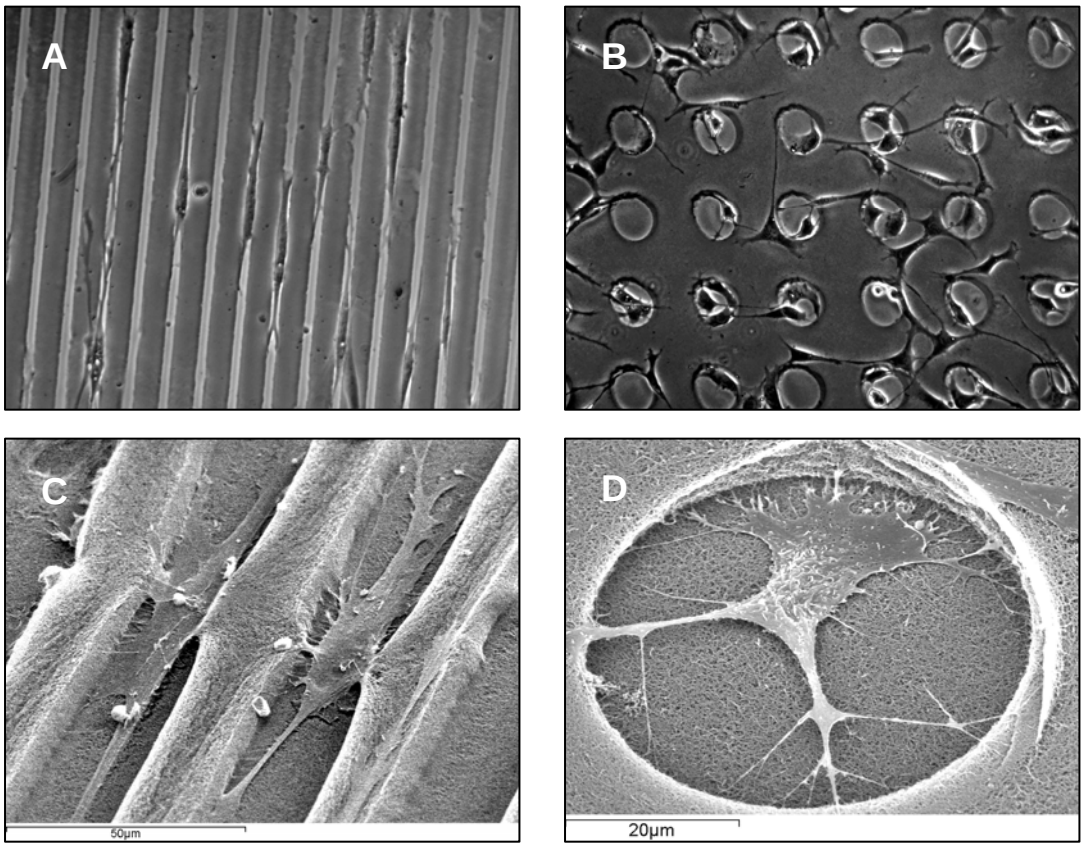

Figure 3.30. SEM images of the cultured human mesenchymal stem cells (hMSCs) on patterned polydiacetylene PA substrates. **A**) The channel pattern containing hMSCs seemingly aligned preferentially with the pattern. **B**) A pattern of 40 μm diameter wells with hMSCs. **C**) Magnification of hMSCs interacting with the channel pattern. **D**) Magnification of one of the wells containing an hMSC clearly adhered and spread out.

3.6 Conclusions

In summary, the incorporation of the diacetylene motif into the PA alkyl tail has provided both valuable structural insight of the nanofiber interior and has offered improved mechanical properties needed to create microfabricated hierarchical textures for the continued advancement in tissue engineering and regenerative medicine. A series of diacetylene PAs either with linear or branched molecular architectures showed varying degrees of polymerization from spectroscopy studies, which is correlated to the degree of the nanofiber internal ordering. The branched PAs displayed weaker polymerization efficiency, most likely due to less efficient molecular packing within the nanofiber compared to linear PAs. Interestingly, the polydiacetylene chain in linear PAs exhibited a chiral CD signal induced by the β-sheet, which was found to vary with temperature potentially due to the changes in aggregation states. A proposed model of an idealized internal structure of the nanofiber is proposed, showing the PA molecules to twist with the β-sheet. Changes in the β-sheet sequence, or sequence length of up to eleven residues still result in PDA formation; however, it appears that any disorder induced by the addition of non-β-sheet forming residues will reduce polymerization efficiency. Micrographs of the PAs before and after polymerization yield no observable morphology changes. Rheological experiments measured the mechanical response of several linear PAs, showing the storage moduli of non-polymerized and polymerized gels to be between 10^3–10^4 Pa. Polymerization of the gels resulted in slightly stiffer materials that could be handled with forceps, unlike their nonpolymerized counterparts. The mechanical improvement of PAs led to attempts in materials processing by soft lithography using the SASE technique and microfabrication. Both micropatterning methods yielded intact patterns of PAs. Additional microfabrication and cellular studies using hMSCs was

done by Alvaro Mata, demonstrating the promising results of patterning PDA PAs to control cellular responses while demonstrating cellular viability when in contact with the diacetylene PA material.

3.7 Experimental

3.7.1 Materials

All amino acids and resins were purchased from Novabiochem Corporation (San Diego, CA), AnaSpec Corporation (San Jose, CA), and Advanced ChemTech (Louisville, KY). 10, 12-Pentacosadiynoic acid was purchased from Fluka (Sigma-Aldrich, St. Louis, MO) and Alfa Aesar (Ward Hill, MA). *n*-Pentacosanoic acid was supplied by TCI America, Inc. (Portland, OR). All other reagents and solvents for peptide synthesis were purchased from Sigma-Aldrich or Mallinckrodt (Hazelwood, MO) and used as provided. For the PDMS stamp, all polymer materials were purchased from Gelest, Inc. (Morrisville, PA).

3.7.2 Synthesis

Peptide amphiphiles were manually synthesized by Fmoc SPPS using orthogonal protecting strategies as discussed in section 2.8.2. Compound purity was analyzed by an analytical reverse-phase HPLC on an Agilent 1050 system equipped with a either a Phenomenex Jupiter C_{18} column (10 μm particle size, 150 mm x 4.6 mm) or a Waters Atlantis C_{18} column (5 μm particle size, 150 mm x 4.6 mm, or 250 mm x 4.6 mm). Purification by RP-HPLC was done using a preparative Varian or Agilent HPLC system equipped with either a Waters Atlantis C_{18} preparative column (5 μm particle size, 250 mm x 30 mm) or a Phenomenex Jupiter C_{18}

preparative column (10 μm particle size, 150 mm x 30 mm). Confirmation of mass and purify included ESI (LCQ Advantage) and MALDI-TOF-MS (Voyager DE Pro).

Diacetylene Polymerization

Polymerizations of self-assembled diacetylene PAs and controls were performed by irradiation at 254 nm using a compact handheld 4-W lamp (UVP Model UVGL-25). Samples were prepared in aqueous solution and irradiated approximately 3 cm from the source for 2 min in a cuvette, unless otherwise noted. The entire mixture was cured at 60°C for 2 h followed by careful removal of the PDMS stamp.

PDMS Stamp Processing

The PDMS stamps were made by first spin-casting the master mold in h-PDMS and baking the sample at 50°C for 15 min. The h-PDMS prepolymer mixture was comprised of 0.69 g vinylmethylsiloxane, 6 μL platinum catalyst, and 0.3 g hydromethylsiloxane–dimethylsiloxane copolymer. The spin-coating parameters were 4000 RPM for 60 s. Soft PDMS was then casted over the h-PDMS film. The PDMS prepolymer mixture consisted of Sylgard 184 PDMS and the cross-linker in a 10:1 w/w ratio.

3.7.3 Instrumentation

Spectroscopy

UV-vis spectroscopy was performed using a Cary 500 Spectrometer for concentration and time-dependent irradiation experiments at room temperature. A model J-715 Jasco CD Spectrometer was used for concentration and temperature-dependent CD experiments. Before data acquisition, all CD samples were allowed to equilibrate at the set temperature for 5 min and

averaged over four runs. Data was collected from 750 to 190 nm. Concentrations for all samples unless otherwise noted were at 100 μM in water, using semi-micro 1 cm path-length quartz cuvettes. For photoirradiation experiments using spectroscopy, the samples were prepared in the cuvette, followed by irradiation.

Microscopy

AFM was performed on a DI SPM instrument using tapping mode on silicon substrates that were pre-washed with piranha cleaning solution, water, and isopropyl alcohol. Standard silicon AFM tips were purchased from Asylum Research (Santa Barbara, CA). Samples were prepared by drop casting 1 μL of a 0.1 wt% solution on to the substrate and then dried by evaporation at room temperature over time. Samples were initially prepared as 2 wt% solutions, gelled, then irradiated and diluted as necessary.

TEM was performed on a Hitachi H-8100 TEM using 200 keV accelerating voltage. Samples were prepared similarly to those described in the AFM procedure by drop casting 1 μL of 0.1 wt% PA solution on to a carbon-coated copper grid (SPI Supplies, West Chester, PA). The samples on the grid were stained for 1–5 min in PTA or 10–20 min with uranyl acetate and the excess staining solution was wicked away. The grid was gently rinsed in water, blotted dry, and allowed to further dry at room temperature.

Rheology

The storage and loss moduli of several PA gels was monitored using a Paar Physica Modular Compact Rheometer MCR) 300 (Graz, Austria). Samples were prepared by making 4 wt% PA solutions in water and diluting it 1:1 with buffer or basic solutions, yielding a final 2 wt% solution. Dilution occurred directly on the rheometer plate. A 25 mm parallel plate

configuration and a constant temperature at 20°C were used. All samples were first subjected to amplitude sweep measurements (0.01–100%) to determine the region of linear viscoelasticity. Frequency sweeps (100–0.1 s^{-1}) involved the acquisition of the storage (G') and loss (G") moduli data, using 0.8% strain for all PAs. Irradiated samples were photoirradiated for 2 min on the rheometer plate followed by immediate measuring. Non-irradiated samples were allowed to equilibrate for 2 min followed by immediate measuring.

3.7.4 Supplementary

Table 3.1. Mass spectrometry of PAs **12–17**.

PA	Mass Expected	Mass Observed
12	1055.53	1055.88
13	1183.70	1184.86
14	1027.47	1027.81
15	1055.53	1056.86
16	1527.98	1528.96
17	1470.93	1473.97

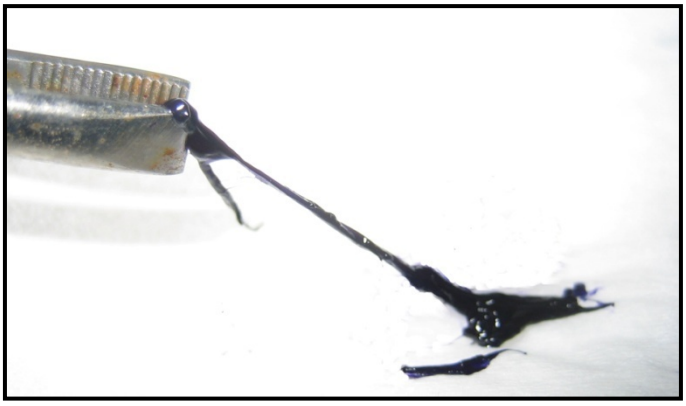

Figure 3.31. The photograph shows the mechanical properties of polymerized PA **12** gel. This degree of pulling cannot be done with the branched PA **13** gel.

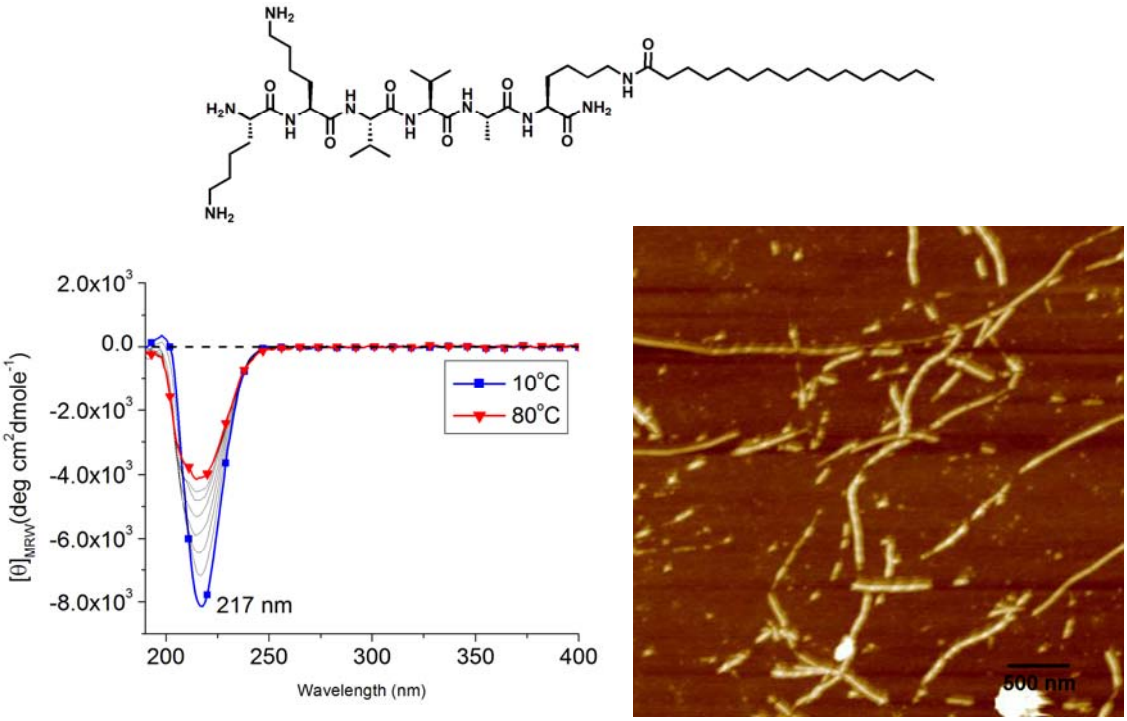

Figure 3.32. CD spectrum (**left**) and AFM image (**right**) of the control PA which has the same residue sequence as PA **14** (**top**) but with a palmitic tail instead of a diacetylene tail.

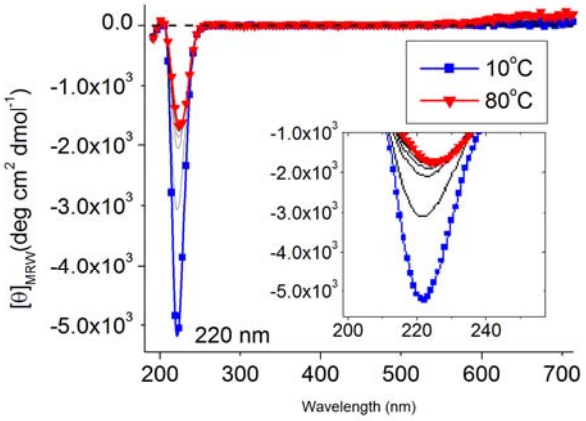

Figure 3.33. Temperature-dependent CD spectrum of non-irradiated PA **16** in water. Samples were measured at 10 degree increments from 10–80°C.

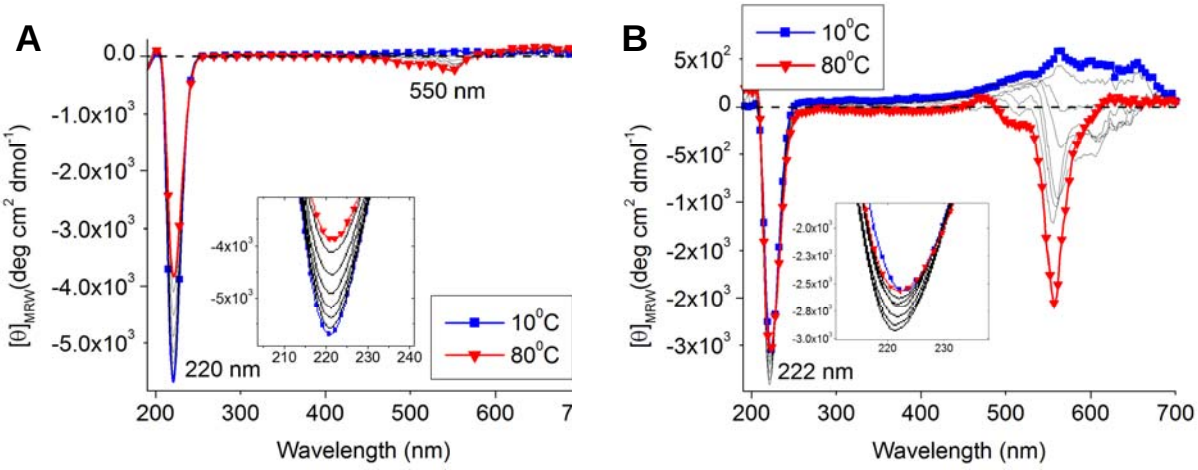

Figure 3.34. Temperature-dependent CD spectrum of photoirradiated PA **16** in **A**) water and **B**) methanol at 100 μM concentration. Samples were measured at 10 degree increments from 10–80°C.

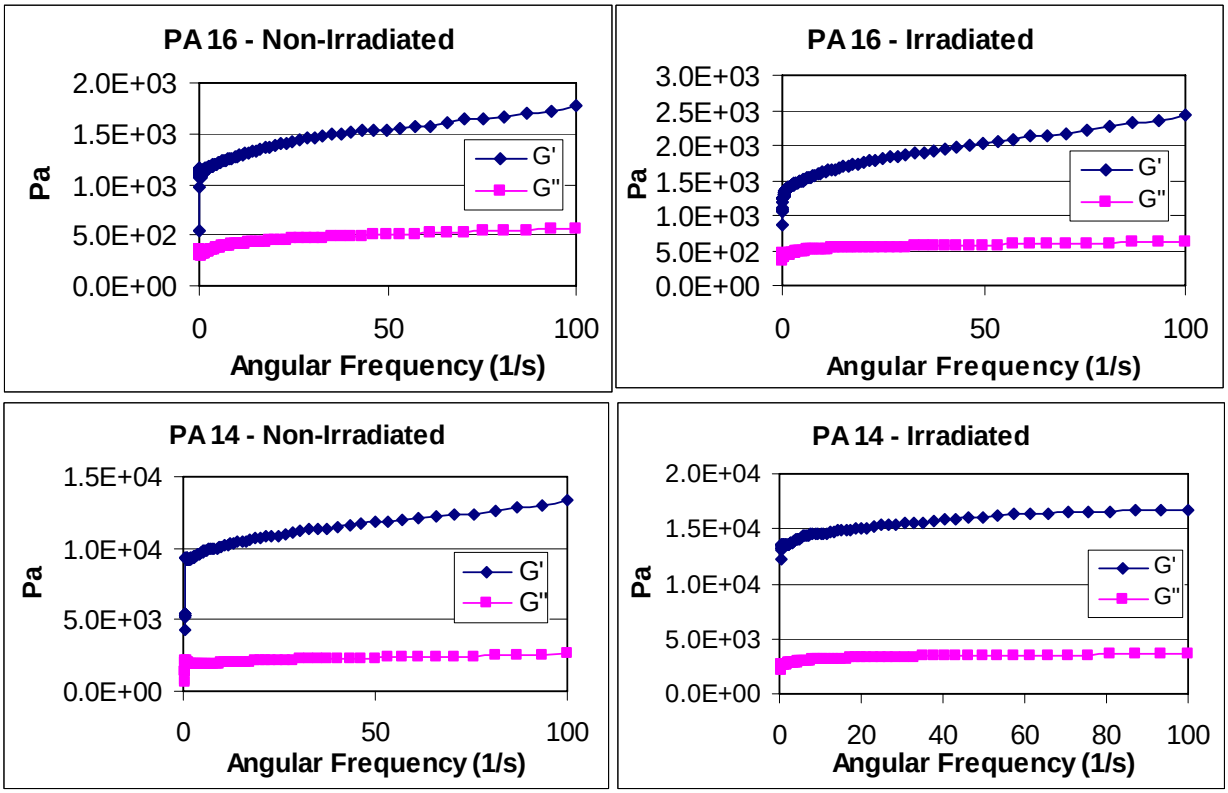

Figure 3.35. Rheology measurements of PA **14** and **16** with or without photoirradiation. As shown, G' > G" at all data points are typical of gel behavior.

Chapter 4: Coumarin Peptide Amphiphiles

Coumarin is known to form reversible dimers from a [2+2] cycloaddition reaction. In parallel with the diacetylene PA research that focused on the combining self-assembly and polymerization, the incorporation of dimer-forming crosslinkers into the PA architecture was also investigated. Peptide amphiphiles containing a coumarin moiety were analyzed as a potentially reversible sol-gel material, harnessing the reversible cycloaddition reaction to switch 'on' or 'off' the nanofiber-forming propensities of the PA.

Coumarin is also a biologically relevant substance that has shown anti-tumor and anti-proliferative activity *in vivo*, with these effects accredited to its metabolites (e.g. 7-hydroxycoumarin). From a biological perspective, a coumarin-containing PA could be applied as a potential anti-cell proliferating scaffold. The advantages of using a self-assembled PA scaffold to present the coumarin includes i) encapsulation of the bioactive molecule using biocompatible compounds and ii) solubilization of the coumarin when attached to the PA in aqueous conditions. Both cell culturing experiments for the biological application and the dimerization experiments in the attempts to create a reversible sol-gel material are discussed in this chapter.

Chapter 4.1 Introduction and Background

The coumarin is known for the ability to undergo reversible [2+2] photodimerization reactions.[160] The reversible reaction permits dimerization at UV wavelengths greater than 300 nm and breaking of the dimer at wavelengths less than 290 nm. This reaction has been an attractive crosslinker for various reasons such as its insensitivity in the presence of oxygen and

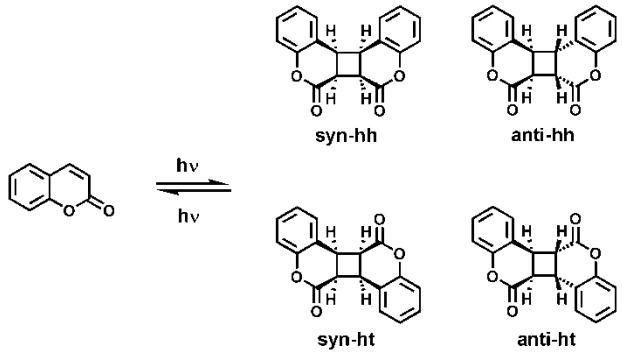

Figure 4.1. Photodimerization of coumarins yielding 4 potential dimer products.

unnecessary need for initiators. The [2+2] reaction may yield four different stereoisomers being either head-to-head (hh) or head-to-tail (ht) dimers as well as syn- or anti-dimers (Figure 4.1) depending on the coumarin substituents and the solvent, which favor different excited state pathways.[161] As a general finding, hh dimers are always the most populous and syn-hh dimers (**1**) form in polar solvents. The most applicable example comparable to our coumarin PA systems is a system of coumarin-containing micelles in aqueous solvent. The post-irradiation product distribution of the micelle system showed the majority of the dimers as syn-hh or anti-hh dimers. The simple irradiation process to crosslink coumarins has led to its application in the crosslinking of various systems, particularly polymeric systems to align molecules[162] or rigidify materials.[163] They have also been specifically used in the development of photosensitive materials such as photoresponsive photoresists, gels,[164] and adhesives,[165-168] which readily dimerize when exposed to the appropriate UV wavelength.[169]

Coumarin and its derivatives have also been utilized for their biological relevance and are naturally found in many plants and even microorganisms.[170, 171] Known historically as an herbal remedy, their physiological affects have been studied for having antibiotic,[172-174] anti-

proliferative,[175] anticoagulant,[176] and anti-inflammatory activities.[177, 178] In 2007, the coumarin derivative, warfarin, was FDA approved as an anti-coagulant drug.

Due to its interesting properties as a biological drug and crosslinker, the coumarin moiety was attached to the alkyl segment of the peptide amphiphile. The initial objective was to utilize its reversible [2+2] reaction to create novel PAs that could form reversible sol-gel materials. The secondary objective was to investigate the coumarin-PA effects, if any, on the cellular growth of SKBr-3 cancer cells.

4.2 Coumarin Synthesis

The first design of the coumarin PA has the coumarin compound located at the terminal end of the alkyl tail due to the limited solubility of the free coumarin molecule. This required the preparation of the coumarin alkyl tail. Shown in Figure 4.2, 7-hydroxycoumarin was reacted with 11-bromoundecanoic acid. The synthesis of **4.1** (Figure 4.2) was done by reacting the

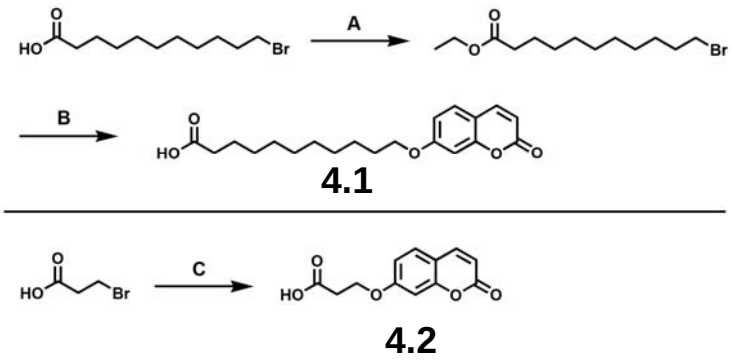

Figure 4.2. Synthesis of coumarin derivatives **4.1** and **4.2**. Synthesis conditions: **a**) H_2SO_4, EtOH, 1 h, reflux; **b**)7-hydroxycoumarin, K_2CO_3, 18-crown-6, acetonitrile, 2 h reflux; NaOH in dioxane/water (1:1); **c**) 7-hydroxycoumarin, K_2CO_3, 18-crown-6, acetonitrile, 2 h reflux.

bromoalkyl ethyl ester with coumarin using potassium carbonate with 18-crown-6 and refluxed in acetonitrile. The ethyl group was then removed using sodium hydroxide in a 1:1 mixture of dioxane and water. The product was then precipitated and recrystallized from hexanes/EtOH to afford 79% of the desired product as a white solid. The compound **4.1** was then incorporated into SPPS for PA synthesis.

A second coumarin-containing PA was synthesized to place the coumarin onto the side chain of an amino acid. This molecule was designed so that the coumarin would not be buried within the self-assembled nanofiber and the coumarin would be more bioaccessible. The synthesis of compound **4.2** was done to enable attachment of the coumarin during SPPS. This synthesis was initially performed with bromoacetic acid as a very short alkyl linker. However, significant decarboxylation of the acid was observed under the reaction conditions. Therefore, we chose to use the longer 3-bromopropionic acid to react with 7-hydroxycoumarin yielding product **4.2** at 42% yield. Compound **4.1** and **4.**2 were then used in the Fmoc solid-phase peptide synthesis of PAs **18** and **19**, respectively.

PA **18** and **19** have the β-sheet segment as Leu-Leu-Ala (Figure 4.3) which has been successfully used in previous nanofiber-forming PA molecules. All PAs were cleaved and purified under the same conditions as previously mentioned in Chapter 3. The sequence of PA **18** contains: Lys-Lys-Leu-Leu-Ala-Lys with the coumarin alkyl tail at the *C*-terminal end of the PA. The PA **19** has the coumarin-derivative coupled to the epsilon amine of a lysine residue within the sequence: Lys-Lys-Leu-Leu-Ala-Lys(Coumarin)-Lys and has a palmitic alkyl tail.

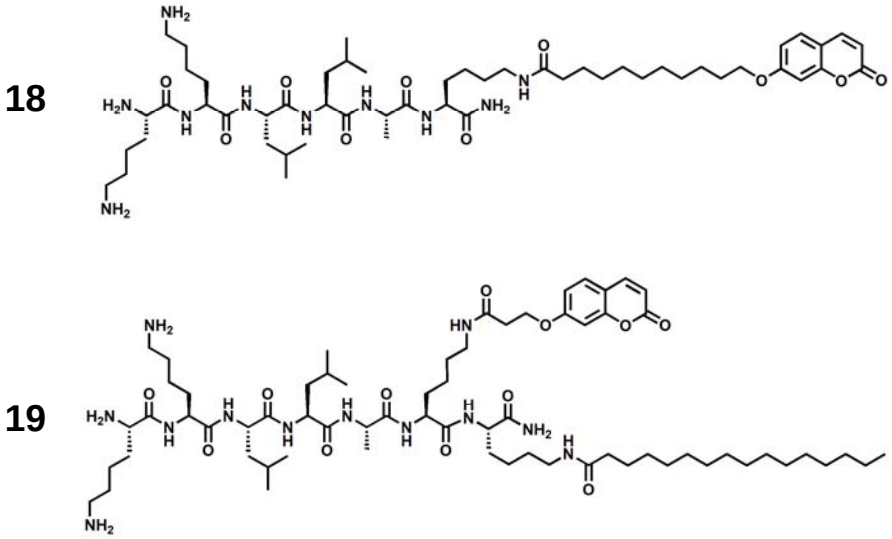

Figure 4.3. PA structures **18** and **19** containing coumarin derivatives at different positions in the molecule.

4.3 Gelation Studies

PA **18** is readily soluble in water, forming a clear solution. The gelation of PA **18** was investigated by exposing a 1 wt % solution to ammonia vapor from a solution of ammonium hydroxide. Gelation of the solution occurs within 5 min of exposure due to the neutralization of the net positive charge from the PA lysine residues, causing further aggregation. Longer exposure time (> 5 min) under the basic conditions led to a yellow color change of the solution. Under a long wavelength light source, the solution also appeared a fluorescent blue-green color only under these long exposure times (Figure 4.4). Although the UV–vis spectrum only showed a slight broadening of the 324 nm band after exposure to basic conditions, the MALDI mass spectrometry data revealed the presence of the product mass (*m/z*: 1028.97) and a peak at 884.84,

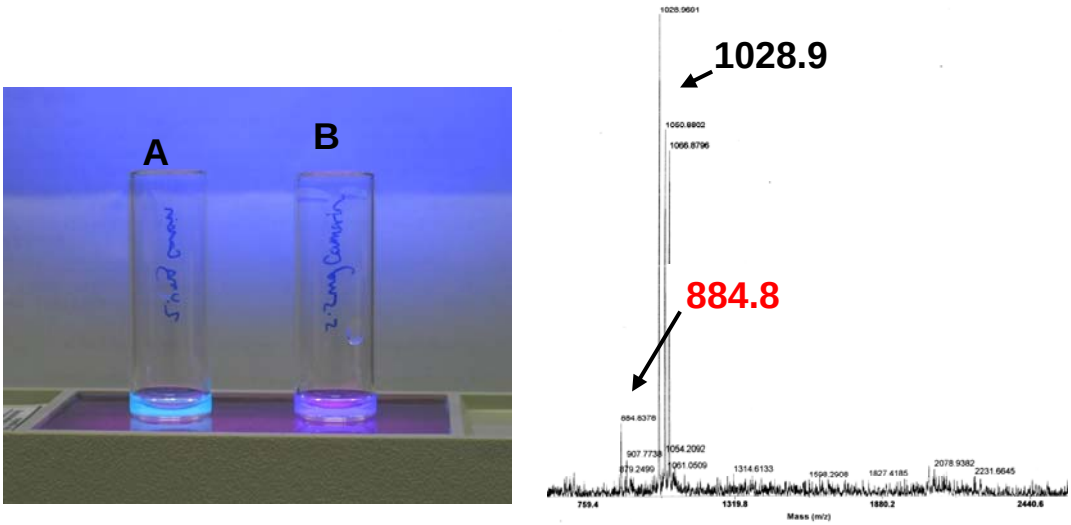

Figure 4.4. **Left**: Photo image of PA **18** with **A**) prolonged exposure to NH_4OH vapors (~ 10 min) and **B**) with no exposure to basic conditions. The fluorescent blue color indicates the presence of the free coumarin anion. **Right**: MALDI data of PA **18** with prolonged exposure to basic conditions. The mass at 884.84 is the mass of the PA without the coumarin.

which corresponds to the mass of the PA without the coumarin. This finding demonstrated the base hydrolysis cleaving of the coumarin from the PA molecule if exposure to basic vapors was longer than 5 min. Analysis with free 7-hydroxycoumarin alone showed the addition of basic solution yielded a yellow product, also appearing blue-green under long wavelength light. From previous literature, it is known that deprotonated hydroxylated coumarins are yellow colored and fluorescent.[179] These findings indicate that future gelations studies of coumarin-containing PAs should use minimal exposure to basic conditions.

As previously discussed, coumarins form [2+2] cycloaddition products when irradiated at wavelengths above 300 nm and revert back to its parent molecule when irradiated at wavelengths below 290 nm. The PA gels were exposed to both crosslinking and uncrosslinking conditions to see how this affected the material properties of the gel. Once the gel of PA **18** was formed, the

cuvette containing the gel was inverted upside down, placed in a photoreactor, and irradiated either at 350 nm with a 300 nm cut-on filter or irradiated at 254 nm. Irradiation at 350 nm should dimerize any neighboring coumarin molecules, while irradiation at 254 nm should break any [2+2] products formed. Ideally, dimerization of the material should disrupt the nanofiber network and prevent the formation of a gel, while uncrosslinking the coumarin should enable reformation of the gel over time. However, regardless of the photointensity of the reactor or irradiation time, the material remained as a self-supporting gel. Similar gelation experiments were done with PA **19**, but reduced solubility of the molecule hindered the formation of any gels. When exposed to basic conditions, PA **19** at a 1 wt% solution remained cloudy containing precipitates and no change was observed when irradiated at either wavelengths. The lack of solubility is most likely due to the coumarin placement, possibly disrupting the molecular packing of the PA molecules. As described in the following sections, the coumarin reaction within the PA nanofibers was further investigated by spectroscopy and microscopy.

4.4 Analysis of Coumarin Crosslinking by Photoirradiation

The UV–vis and CD spectroscopic analysis of the coumarin PAs were used to analyze the crosslinking and the reversibility of the reaction. The photoreaction of the PA solutions and gels for **18** and **19** was done using a Rayonet photoreactor containing 350 nm and 254 nm bulbs required for the crosslinking or uncrosslinking of the coumarin reaction. Photoirradiation at 350 nm also included the use of a home-built 300 nm cut-on band filter container, which prevented exposure to any wavelength under 300 nm. The filter container was created by using epoxy-glue to assemble 5 square-cut filters into a cube shape. No filter was used for the 254 nm irradiation.

Due to the possibility of base hydrolysis, concentrated stock solutions of the PAs were formulated in water and diluted to the desired experimental concentrations without gelation. It should be noted that even without the presence of the base, the PAs are able to form nanofibers in solution.

*4.4.1 Spectroscopy and Microscopy of PA **18***

The UV−vis spectrum of 7-hydroxycoumarin shows an absorbance maximum at 324 nm,[178, 180] which is also observed in the UV−vis spectra of PA **18**. To monitor the crosslinking reaction, the decrease of the 324 nm band is observed at different irradiation time points, indicating loss of the coumarin monomer and formation of the dimer. Irradiation at 254 nm should allow recovery of the parent molecule, observed as an increase of the 324 nm monomer band. Prior to crosslinking of the coumarin PA, every sample is irradiated at 254 nm to ensure complete uncrosslinking of any dimers that may have formed over time as shown in Figure 4.5A. Additional exposure at 254 nm for several minutes after 3 min did not change the peak intensity at 254 nm. The sample was then irradiated at 350 nm to crosslink the coumarin PAs, and a steady decrease in the monomer band is observed (Figure 4.5B). This cycle was continued once more and the monomer band was observed to follow the same trend although it should be noted that the 350 nm irradiation time was only 15 min for the second cycle. Although the reaction shows some reversibility through two crosslinking/uncrosslinking cycles, the uncrosslinking reaction is less efficient with each subsequence cycle. MALDI data showed the presence of monomer and dimer products prior to any photoirradiation. Irradiation at 254 nm showed only trace dimer

product by mass spectrometry, followed by 350 nm irradiation showing the renewed presence of the dimer product at ~1055 *m*/*z* value. The MALDI data for the second photoirradiation cycle at

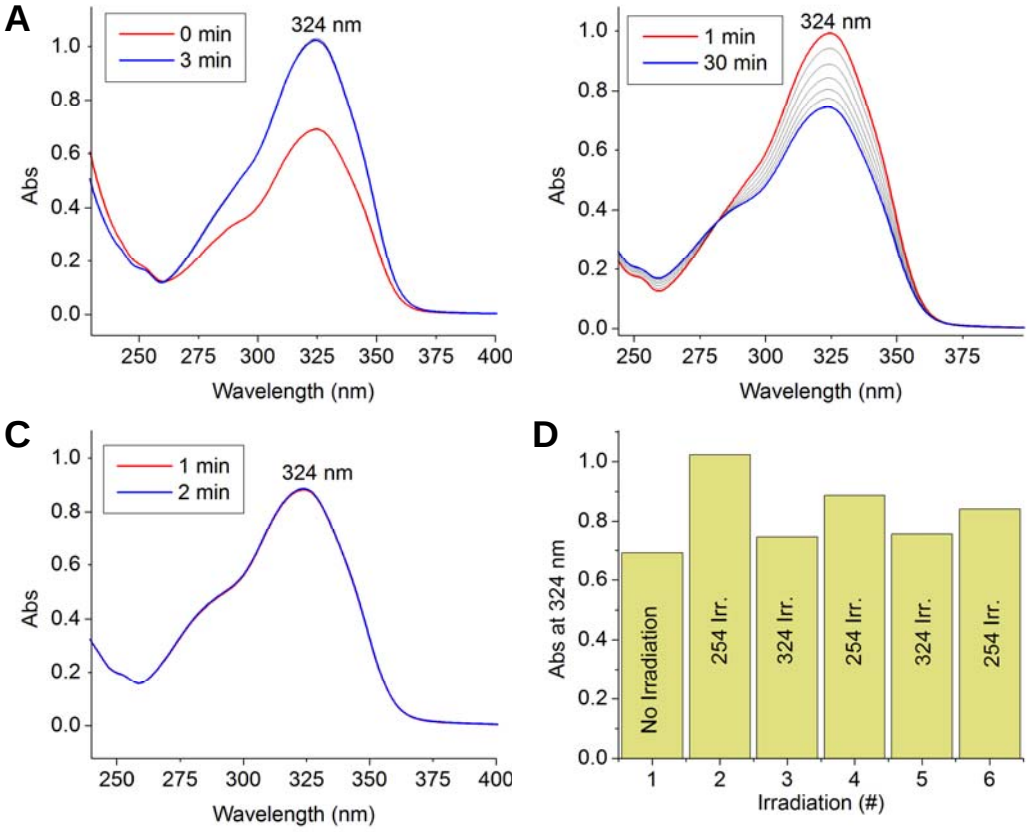

Figure 4.5. UV–vis spectroscopy of photoirradiation cycles, alternating between 254 nm and 350 nm wavelengths. Photoirradiation of PA **18** was monitored using 100 μM samples. **A**) 254 nm irradiation of PA **18** up to 3 min. The monomer coumarin band can be observed at 324 nm. **B**) 350 nm irradiation of PA **18** up to 30 min. **C**) Second cycle of irradiation at 254 nm. **D**) Bar graph of absorbance at 324 nm plotted after each irradiation phase. It should be noted that the second cycle of 324 nm irradiation (5) was only for 15 min.

254 nm still showed presence of the coumarin dimer. This lack of reversibility after dimer formation has been demonstrated in literature[181] which may be correlated to the added complication of being 'trapped' in a supramolecular system. The same UV–vis experiment was repeated in methanol to see whether destabilization of the nanofibers via weakening the β-sheet would improve the reversibility of the photoirradiation experiments. The initial irradiation at 254 nm uncrosslinked any dimerized coumarins and the UV band intensity at 324 nm increased. However all irradiation steps afterwards did not change the intensity of the 324 nm band. The inability for the crosslinking reaction to occur in methanol suggests the orientation of the coumarins to not be favorable. This may be due to the unfavorable orientation of the coumarin PA aggregates.

The CD spectra of PA **18** showed the presence of β-sheet-like signal at 230 nm (Figure 4.6). There was minimal change of the β-sheet after photoirradiating the samples at both 254 nm

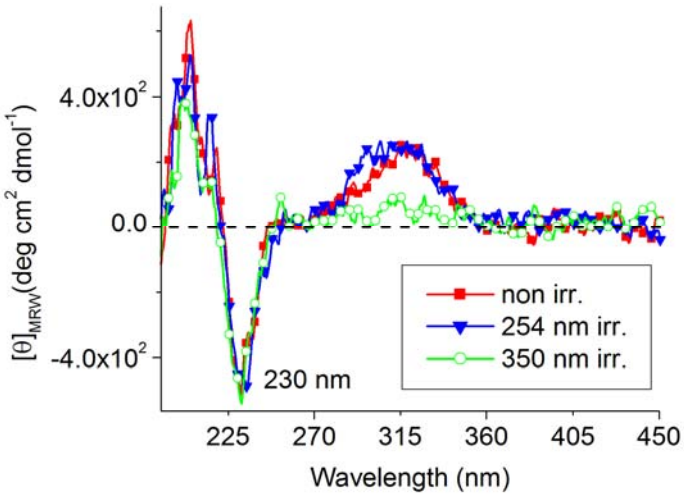

Figure 4.6. CD spectroscopy of PA **18** after different periods of irradiation exposures. The sample concentrations were 100 μM in water.

and 350 nm. The weak positive band observed at 315 nm until 350 nm irradiation is most likely due to the coumarin molecule which loses its CD signal after dimerization. From the CD data, it can be concluded that the β-sheet-like secondary structure persists throughout the photoirradiation reactions.

Both conventional TEM and AFM experiments were done to examine whether photoirradiation caused any significant morphology changes. This may provide insight into the gelation and spectroscopic recently described. The samples were prepared from 0.1 wt% PA solutions. Microscopy images were taken of samples with no irradiation, after 3 min of photoirradiation at 254 nm, after 30 min of irradiation at 350 nm, and after a second cycle of 254 nm irradiation for 3 min.

Figure 4.7 shows the presence of different morphologies for PA **18** after photoirradiation at either 254 nm or 350 nm. After the initial 254 nm irradiation, the fibers are still present and unchanged in diameter (6–10 nm). Irradiation at 350 nm appears to alter the morphology to include amorphous aggregates; however, there is also the occasional presence of fiber-like structures. The second cycle of uncrosslinking photoirradiation at 254 nm led to a mixture of both nanofibers and amorphous aggregates similar to what was observed at 350 nm (Figure 4.7D). This coincides with the UV–vis experimental results if we associate the amorphous aggregates with dimer formation and the nanofibers with non-dimerized PAs. PA **18** samples were also irradiated in methanol and imaged as shown in Figure 4.8. The presence of short nanofiber-like aggregates can be observed after photoirradiations at both wavelengths. This lack of morphology change after photoirradiation is in agreement with the constant intensity at 324 nm in the UV–vis spectra of PA **18** in methanol; however, amorphous aggregates (Figure

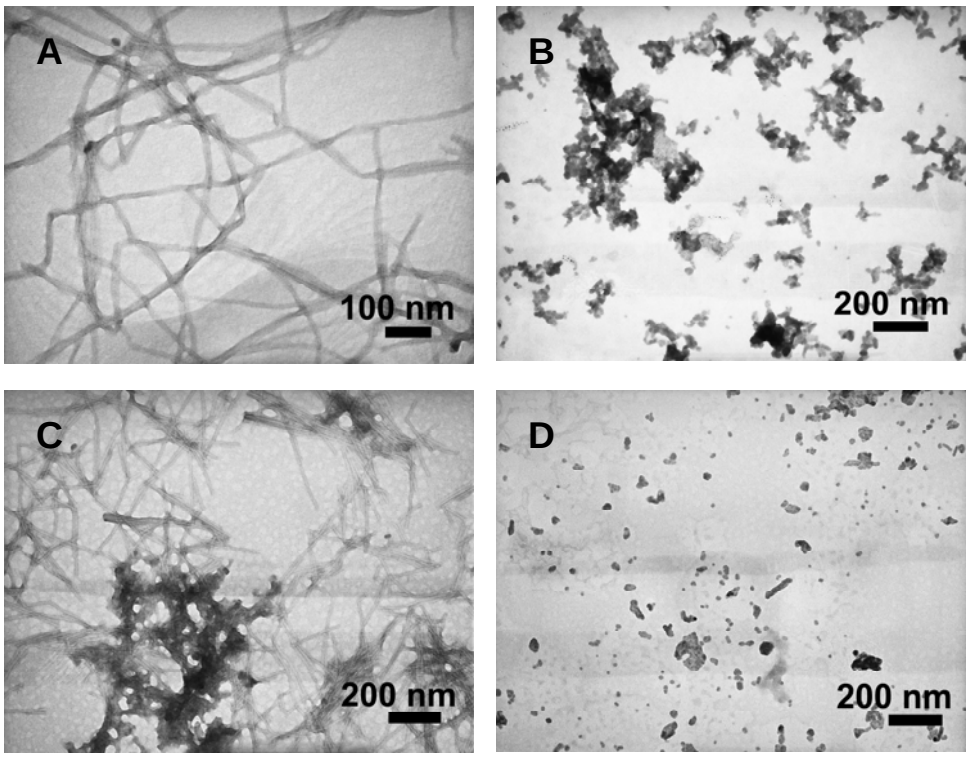

Figure 4.7. TEM micrographs of PA **18** observed after irradiation at either 254 nm or 350 nm. **A**) After irradiation at 254 nm for 3 min. **B**) After irradiation at 350 nm for 30 min, amorphous morphologies are seen. **C**) From the same TEM grid as image **B**, mixed morphologies between fibers and amorphous aggregates are seen. **D**) After a second irradiation cycle at 254 nm, both aggregates and fiber-like structures are observed.

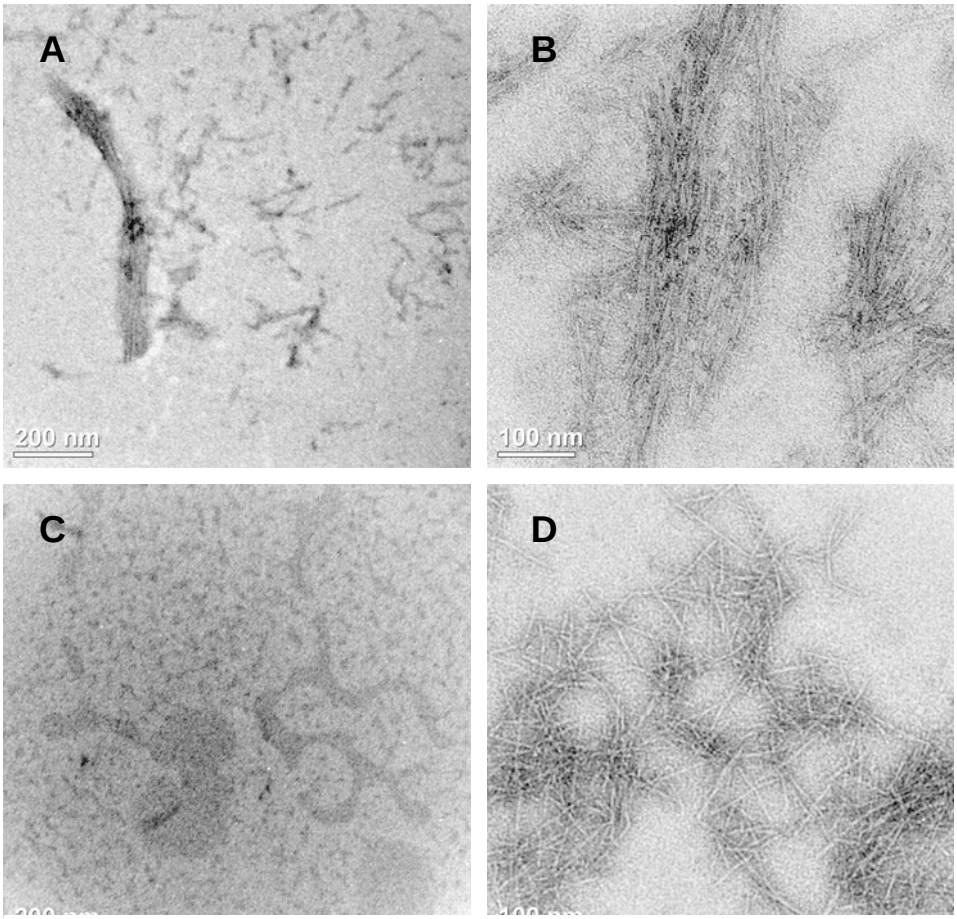

Figure 4.8. TEM micrographs of PA **18** drop-cast from methanol, observed after irradiation at either 254 nm or 350 nm. **A**) After irradiation at 254 nm for 3 min. **B**) After irradiation at 350 nm for 30 min, amorphous and fiber-like structures are seen. **C**) From the same TEM grid as image **B**, amorphous film is observed. **D**) After a second irradiation cycle at 254 nm, both aggregates and fiber-like structures are observed.

4.8C) were also observed in the methanol samples for the same samples. The presence of aggregates and shorter fibers may be attributed to the reduced organization of the PA molecules due to a weakened β-sheet in the due to weakened β-sheets in the methanol solution.

*4.4.2 Spectroscopy and Microscopy of PA **19** in Comparison with PA **18***

The solubility of PA **19**, which has the coumarin on the side chain of a lysine residue, was significantly reduced compared to PA **18**. This is most likely due to the location of the coumarin, which is not buried within the alkyl tail and has low solubility in water. Initial UV−vis experiments using 100 μM samples had significant scattering from the cloudy sample, so future experiments were done at 50 μM concentrations to reduce the scattering. The same photoirradiation experiment for PA **18** was also done for PA **19** as shown in Figure 4.9. Similar to the results from PA **18**, the samples of coumarin PA **19** also show some reversibility, but when photoirradiated at 254 nm, the maximum absorbance intensity at 324 nm is never regained and continues to decrease with each additional cycle. The dimerization reaction for PA **19** appears to require less time to achieve a significant decrease in the monomer absorbance peak, compared to PA **18**. It is difficult to compare the degree of crosslinking between the two coumarin PAs and the insolubility of PA **19** even at reduced concentrations further complicates the comparison. Interestingly, the photoirradiation of PA **19** in methanol still showed the same semi-reversible trend as observed in water (Figure 4.10). Unlike the observations from PA **18**, the solvent change does not prevent the coumarin reaction from occurring, suggesting the molecular orientation within the PA aggregate is favorable for the reaction. It is possible that

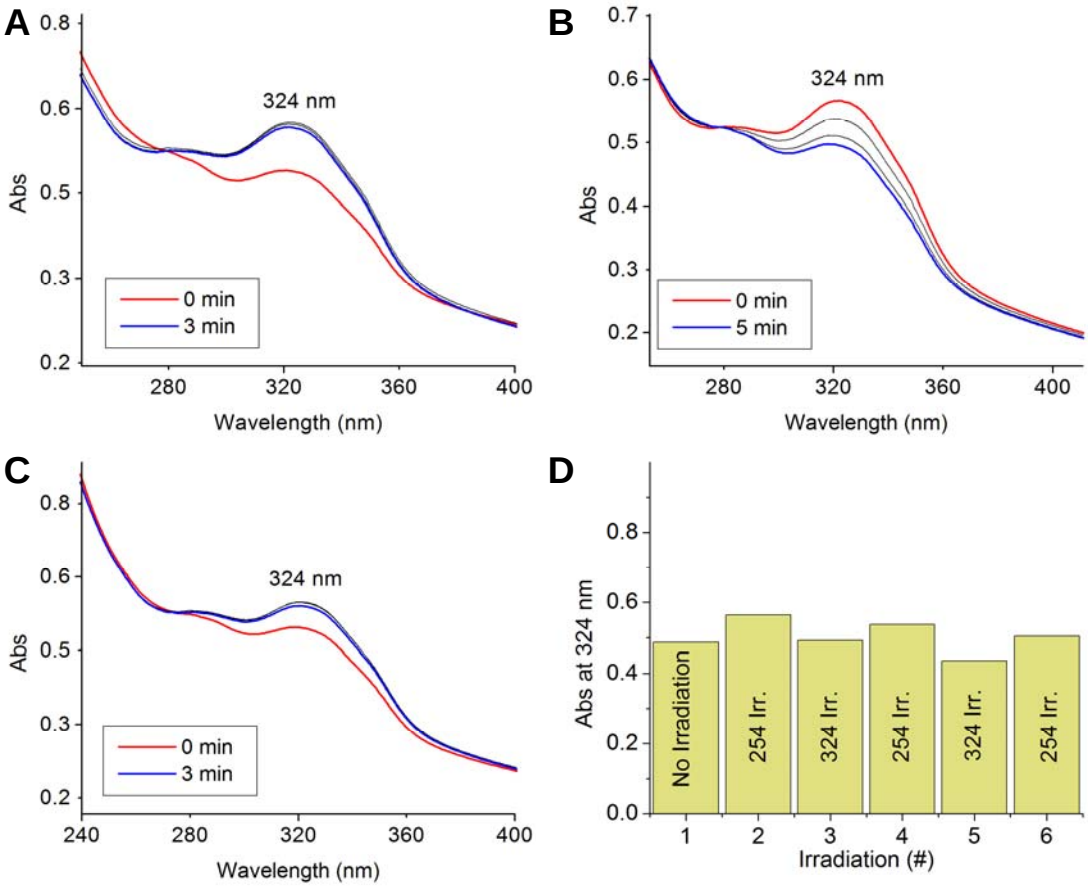

Figure 4.9. UV–vis spectroscopy of photoirradiation cycles, alternating between 254 nm and 350 nm wavelengths. Photoirradiation of PA **19** was monitored using 50 μM samples. **A**) 254 nm irradiation of PA **19** up to 3 min. The monomer coumarin band can be observed at 324 nm. **B**) 350 nm irradiation of PA **19** up to 30 min. **C**) Second cycle of irradiation at 254 nm. **D**) Bar graph of absorbance intensity at 324 nm plotted after each irradiation phase. It should be noted that the second cycle of 324 nm irradiation (5) was for 30 min also.

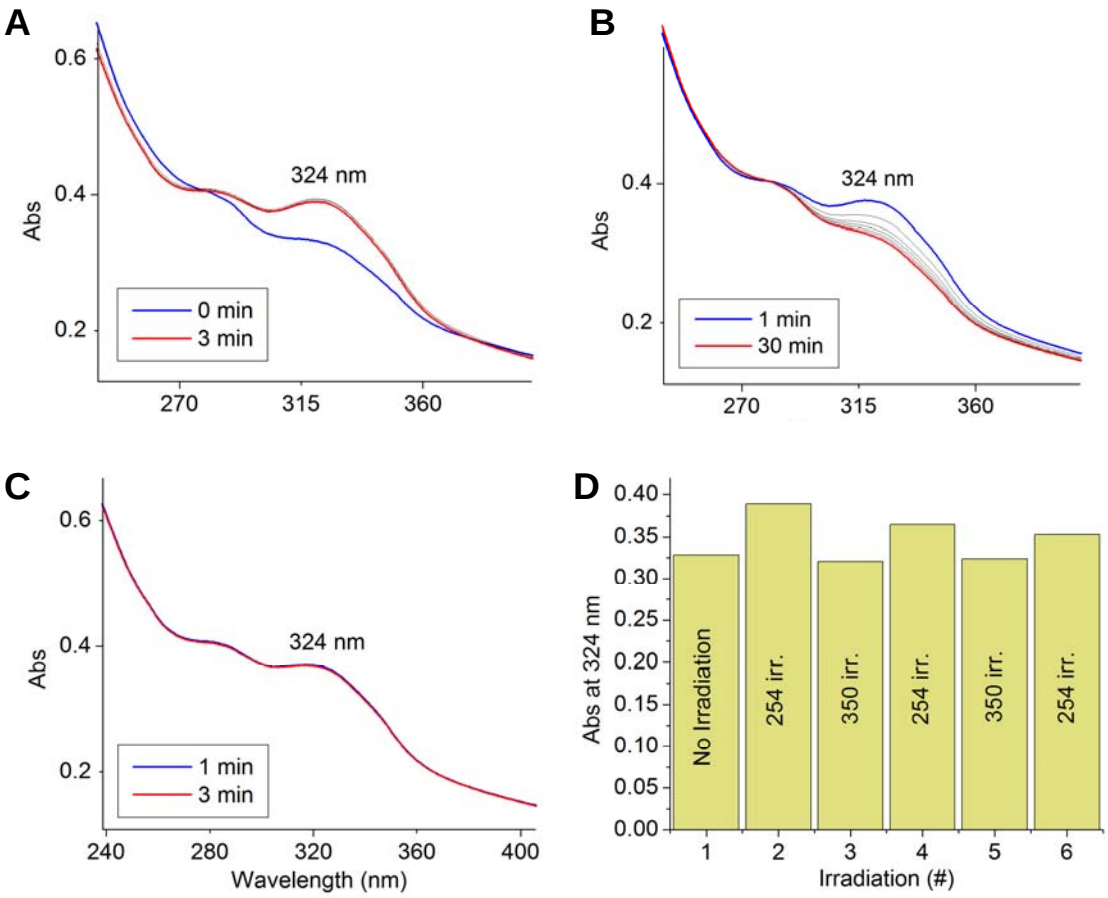

Figure 4.10. Photoirradiation of PA **19** in methanol. **A**) 254 nm irradiation of PA **19. B**) 350 nm irradiation of PA **19** up to 30 min. **C**) Second cycle of irradiation at 254 nm. **D**) Bar graph of absorbance intensity at 324 nm plotted after each irradiation phase. It should be noted that the second cycle of 324 nm irradiation (5) was for 30 min.

placement of the coumarin within PA **19** makes it more accessible for reactivity than the coumarin in PA **18**.

The CD spectra of PA **19**, like PA **18**, also showed the presence of β-sheet-like signal at 225 nm (Figure 4.10). There was minimal change in the CD spectra after photoirradiating the

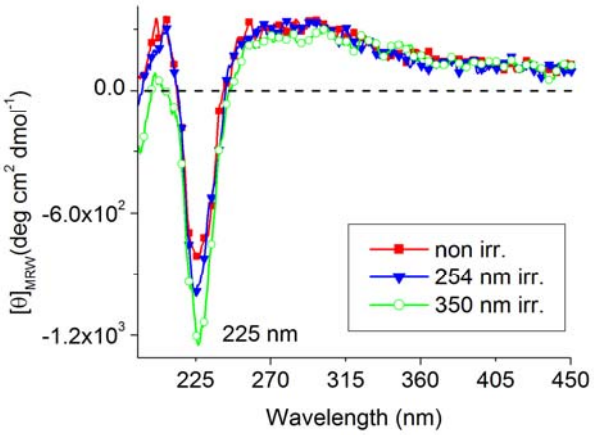

Figure 4.11. CD spectroscopy of PA **19** after different periods of irradiation exposures. The sample concentration was 100 μM in water.

samples at both 254 nm and 350 nm. There is a also a broad positive signal between 270 and 315 nm, which may be attributed to the coumarin molecule; however, this broad signal does not change with irradiation. From the CD data, it can be concluded that the β-sheet-like secondary structure persists throughout the photoirradiation reactions

The reduced solubility of PA **19** required filtering of the samples before imaging which may remove some of the larger aggregates, biasing the observed results. For samples irradiated at 254 nm, short cylindrical nanofiber-like aggregates were observed in both TEM and AFM with a diameter of 5–9 nm and a height of 4–6 nm, respectively (Figure 4.12). Photoirradiating at 350

nm, showed the presence of both cylindrical nanofiber-like aggregates and more amorphous aggregates which also coincides with the observed UV–vis results as discussed with PA **18**.

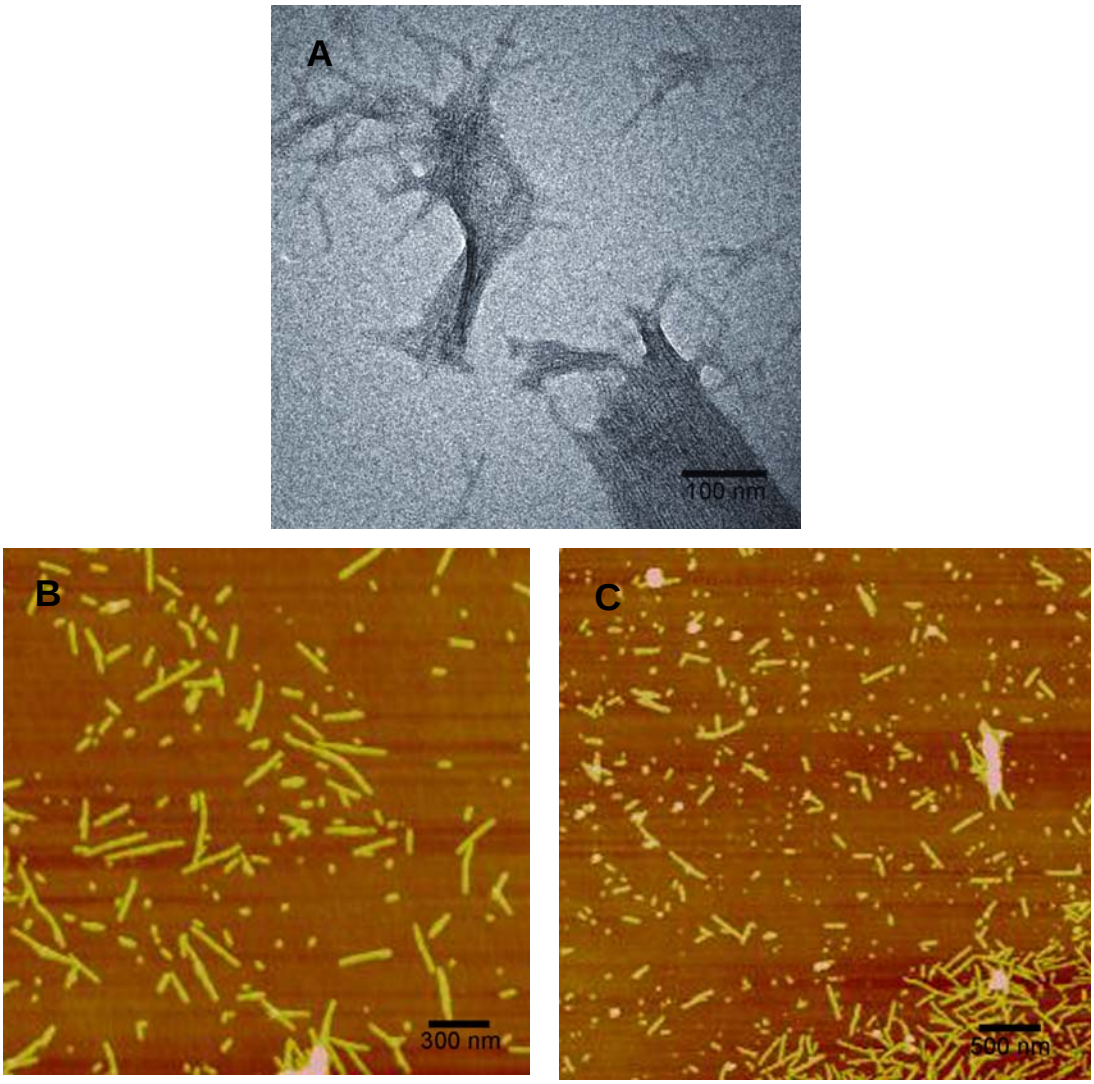

Figure 4.12. TEM and AFM micrographs of PA **19** observed after irradiation at either 254 nm or 350 nm. **A**) TEM micrograph after irradiation at 254 nm for 3 min. **B–C**) AFM image after irradiaton at 350 nm for 30 min. Short fiber-like structures are seen as well as small amorphous structures from the same samples.

In conclusion, both PA **18** and **19** showed crosslinking based upon observations in microscopy and spectroscopy, but a reversible sol-gel material was not achieved due to the incomplete crosslinking/uncrosslinking reaction. Microscopy images showed significant morphology changes for PA **18** showing nanofibers until the initial irradiation at 350 nm resulting in the observation of amorphous aggregates. Prolonged irradiation at 254 nm continued to show a mixture of nanofibers and amorphous aggregates, also supporting the UV–vis data suggesting incomplete reformation of the parent coumarin molecule. The difference in morphology after irradiation for PA **19** was more difficult to discern, partly due to the insolubility of the material which required filtering before imaging. Very short nanofiber-like aggregates are observed in all conditions, however there appears to be more amorphous particulates after 350 nm photoirradiation also suggesting dimerization of PA **19** disrupts the formation of the nanofiber-like aggregates. From this set of experiments, we have learned that i) supramolecular constructs may be a factor in preventing the completion of reactions by 'trapping' the reactive group in a non-reactive position, ii) a mixture of amorphous and nanofiber structure can still remain a self-supporting gel, and iii) placement of the crosslinker within the tail or on the side chain of a peptide residue will affect both solubility and the crosslinker's spatial orientation which may affect the probability of it reacting with an adjacent crosslinker.

4.5 Cellular Behavior on Coumarin PA Substrates

There have been extensive studies using coumarin and its derivatives as anti-proliferation and anti-cancer reagents. A number of cancer cell lines have been exposed to coumarin molecules such as lung[182, 183] and breast cancer cells[184] to investigate the efficacy of coumarin as

an anti-cancer drug. Based upon previous research in literature, the cytotoxicity of the coumarin molecule depends on the cell line and on the coumarin derivative. It is believed that that its anti-cancer activity is due to the metabolites formed from the hydroxylation of coumarin such as 7-hydroxycoumarin. Although the mechanism of 7-hydroxycoumarin is still being investigated, a study on the effects of 7-hydroxycoumarin in the presence of human adenocarcinoma (cell line A427) showed the chemical to inhibit the cell-cycle at the G_1/S transition.[185-188] In the following *in vitro* study, the cytotoxicity and potential anti-proliferation properties of coumarin PA **18** were investigated using SKBr-3 breast cancer cells. PA **19** was not used due to its poor solubility.

These coumarin PA-cell studies were performed in collaboration with Chung-Yan Koh, a graduate student in the Stupp lab. The cells were cultured in a 24-well plate pre-coated with a layer of the coumarin PA that had been irradiated at either 254 nm or 350 nm in solution prior to drying. The film was made by drop casting concentrated PA solutions and letting it dry under sterile conditions. Two other controls in the experiment included media-only wells and a control non-coumarin PA which was identical to PA **18** minus the coumarin. All of the experiments were repeated in 2 sets of triplicates using a 1 mg/mL concentration of all PAs (~ 974 μM). After 2 days of culturing, a proliferation assay was performed to determine the ratio of live/dead cells. The cells in both the media-only (Figure 4.13A) and non-coumarin PA (Figure 4.13B) wells were viable (> 95%) as observed from the green fluorescence of Calcein AM using a Nikon TE200 Eclipse confocal microscope. Interestingly, the cells exposed to the coumarin PA **18** showed significant cell death at regardless of the photoirradiation wavelength used (~66%), indicated by red color from ethidium homodimer-1. The bright field images comparing the

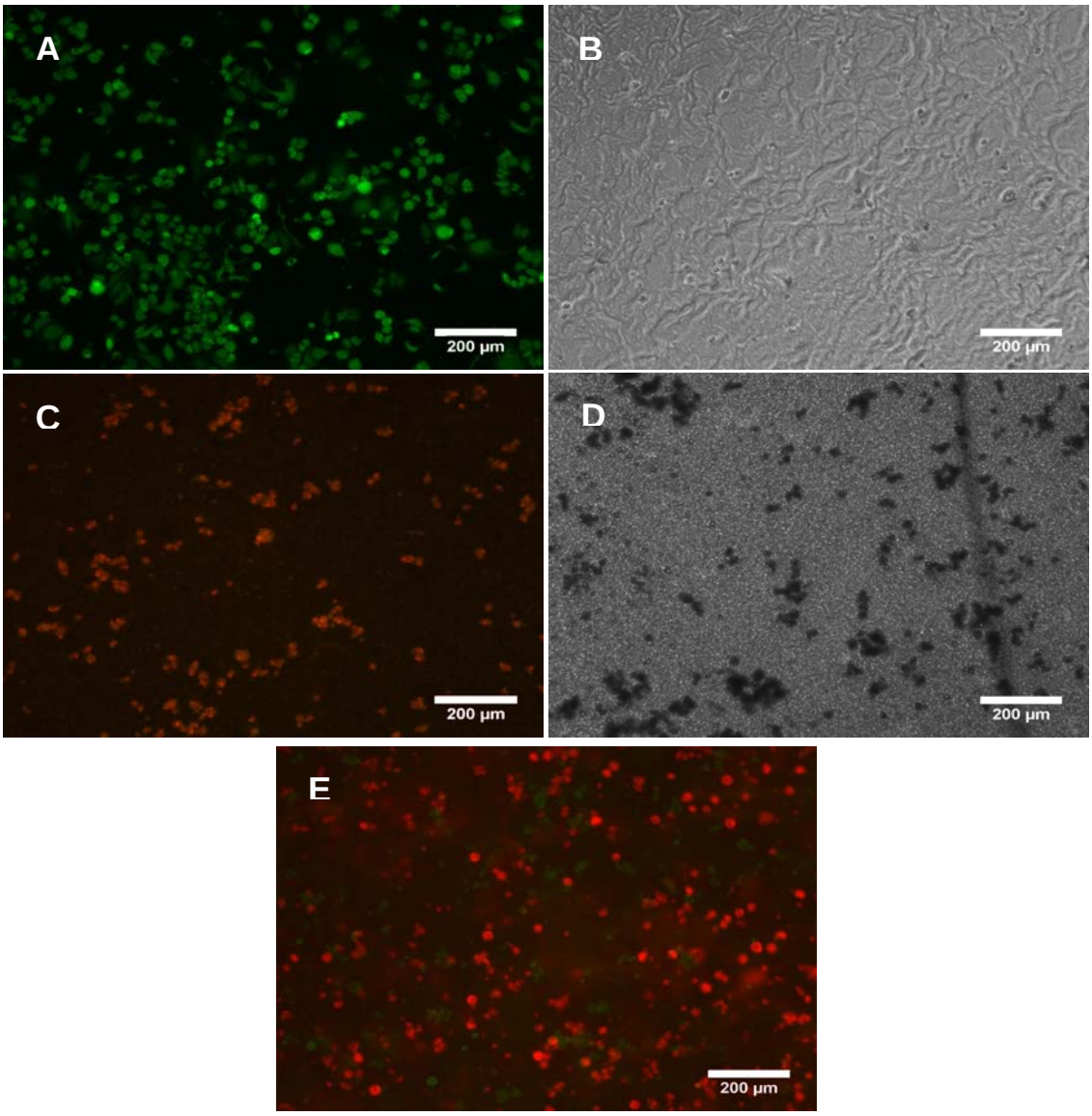

Figure 4.13. Live/dead or bright field images of SKBr-3 cells: **A**) in media only.(live/dead) **B**) with non-coumarin PA. (bright field) **C–D**) with 350 nm irradiated coumarin PA. **E**) with 254 nm irradiated coumarin PA. 1 mg/mL of PA were used for all experiments.

morphologies of healthy and dead cells (Figure 4.13B and 4.13D, respectively) show healthy cells to spread and adhere on the substrate while the dead cells appear darkened and spherical.

The minimum inhibitory concentration (MIC) of free 7-hydroxycoumarin cultured with SKBr-3 cells was also done to compare its cytotoxic efficacy with coumarin PA. MIC is defined as the minimum concentration required to inhibit the growth of, in this case, SKBr-3. Coumarin concentrations ranging from 0–20 mM was cultured with SKBr-3 cells and imaged after 2 days. The MIC from the concentrations investigated was 5 mM, where no cell growth is apparent. At even higher concentrations, the free coumarin eventually crystallized in the well (Figure 4.14F). A tentative comparison between the cytotoxic efficacy of free coumarin (5 mM) versus the coumarin PA shows the coumarin PA (974 μM) to be more effective approximately 5-fold. Future MIC experiments of 7-hydroxycoumarin are needed to also include additional data points between 1 mM and 5 mM for a more accurate estimation.

The reason for the enhanced cytotoxicity of the PA compared to the free-coumarin is not known yet. One hypothesis is that the cellular uptake of the coumarin PA occurs, causing the cell to ingest a locally concentrated amount of coumarin resulting in cell death. Because the coumarin is buried with the PA nanofiber, the cell is not aware of the coumarin molecule until the peptidic segment becomes disassembled or is consumed by the cell. In the presence of free coumarin, the cell does not immediately ingest the molecule and the uptake is significantly reduced. In literature, it is known cells will uptake constructs on the nano-scale regime by endocytosis which may be the uptake mechanism in this case.[189] Future experiments will also include cell proliferation assays of other cells types to see whether the cytotoxicity extends beyond breast cancer cells.

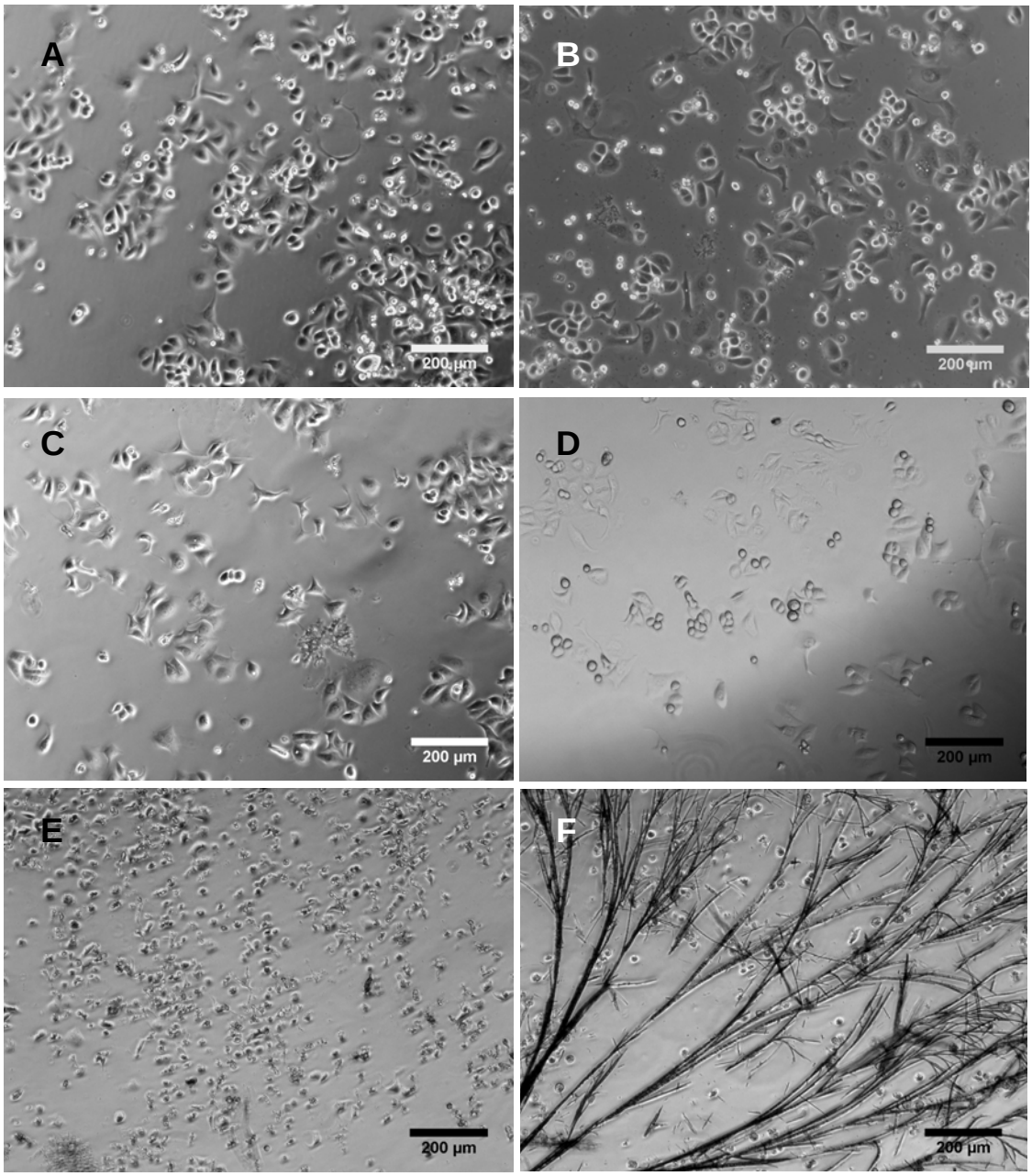

Figure 4.14. An MIC experiment free 7-hydroxycoumarin in the presence of SKBr-3 cells. Bright field confocal images are shown. Coumarin concentrations: **A**) 0 µM **B**) 50 µM **C**) 500 µM **D**) 1 mM **E**) 5 mM **F**) 10 mM.

4.6 Conclusions

The original objective of this project was to create a reversible sol–gel system using coumarin as the crosslinker that would enable the gel to liquid transition by disrupting nanofiber formation. Based on micrographs, the coumarin crosslinking was able to achieve nanofiber disruption forming amorphous aggregates. However, the conversion of some nanofibers to aggregates was not enough to disrupt the bulk gel, which remained self-supporting. The other complication involved the incomplete reversal of the crosslinked dimers after irradiation at 254 nm and as observed by spectroscopy and microscopy, this resulted in a mixture of nanofiber and amorphous morphologies. It is currently not obvious why the system is not completely reversible; however, the supramolecular aggregate may be trapping the coumarin dimers, hindering the uncrosslinking reaction. The solubility of PA **19** with the coumarin group located on a lysine side chain instead of the alkyl tail was significantly lower most likely due to the coumarin located outside of the hydrophobic region of the alkyl tail. Inefficient molecular packing from the coumarin stemming off the lysine chain may prevent the coumarin from being buried within the nanofiber, resulting in its unfavorable exposure to water. Because of its reduced solubility, the PA was not able to gel (1 wt %) and instead formed precipitates.

The cellular experiments using coumarin as an anti-cancer scaffold in the presence of SKBr-3 breast cancer cells was more promising. Proliferation assays of coumarin PA **18** showed significant cell death (66% dead) while control media and the non-coumarin PA showed good viability (> 95% live). An MIC experiment using free 7-hydroxycoumarin showed 5 mM was the approximate minimum concentration to stop SKBr-3 cell growth. This suggests a several-fold increase in the efficacy of coumarin PA toxicity compared to free coumarin. Although the

reasons for this are not known yet, it may be due to the initial cellular uptake of the coumarin PA, resulting in eventual disassembly and/or digestion of the PA, followed by the locally concentrated release of the coumarin causing cell death. Future work of this project involves culturing coumarin PAs on other cell types to see whether its cytotoxicity is universal as well as attempting to determine the mechanism of cell death.

4.7 Experimental

4.7.1 Materials

All amino acids and resins were purchased from Novabiochem Corporation (San Diego, CA), AnaSpec Corporation (San Jose, CA), and Advanced ChemTech (Louisville, KY). All other reagents and solvents for peptide synthesis were purchased from Sigma-Aldrich (St. Louis, MO) or Mallinckrodt (Hazelwood, MO) and used as provided. 7-hydroxycoumarin was purchased from Alfa Aesar (Ward Hill, MA). All other reagents for the synthesis of coumarin derivatives were purchased from Sigma-Aldrich. 11-bromoundecanoic acid was recrystallized in hexanes prior to usage. All deuterated solvents were purchased from Cambridge Isotope Laboratories (Andover, MA).

4.7.2 Synthesis

All PAs were manually synthesized by Fmoc solid-phase peptide synthesis using orthogonal protecting strategies in 0.25 mmol scales. All PAs contain a *C*-terminal amide group using Rink Amide MBHA resin. The coupling conditions with coumarin derivates are the same when coupling on a standard amino acid using a 4:4:6 equivalency of the coumarin molecule,

HBTU, and DIEA, respectively in DMF. Detailed synthesis protocols for peptide amphiphiles including RP-HPLC purification conditions may be found in the experimental section of Chapter 2.

Ethyl 11-bromoundecanoate. 11-bromoundecanoic (1.00 g, 3.77 mmol) was added to sulfuric acid (5 equiv, 1.84 mL) in ethanol and refluxed for 1 h. The pH of the solution was adjusted to 7 using NaOH, washed with a brine solution and extracted with DCM. The organic phase was dried with $MgSO_4$ and concentrated to dryness by rotary evaporation to give the desired product in quantitative yield. ^{1}H NMR (500 MHz, $CDCl_3$): δ 4.09 (q, *J* = 7.0 Hz, 2H), 3.37 (t, *J* = 6.5 Hz, 2), 2.26 (t, *J* = 7.5 Hz, 2H), 1.82 (qn, *J* = 7.5 Hz, 2H), 1.60 (at, *J* = 6.5 Hz, 2H), 1.39 (at, *J* = 7.0 Hz), 1.26 (br s, 10 H), 1.22 (t, *J* = 8.0 Hz, 3H).

Ethyl 11-(2-oxo-2*H*-chromen-7-yloxy)undecanoate. Ethyl 11-bromoundecanoate (1.00 g, 3.77 mmol) was added to 7-hydroxycoumarin (0.61 g, 3.77 mmol), K_2CO_2 (3 equiv, 3.65 g), 18-crown-6 (0.10 equiv, 0.10 g), and refluxed for 2 h in acetonitrile. The solution was washed with NaCl solution and extracted with ether. The extractions were rotovapped dry and purified using silica gel chromatography (1% MeOH in DCM). The yield was 1.16 g, 82%. ^{1}H NMR (500 MHz, $CDCl_3$): δ 7.64 (d, *J* = 9.5 Hz, 1H), 7.37 (d, *J* = 8.5 Hz, 1H), 6.84 (d, *J* = 8.5 Hz, 1H), 6.81 (s, 1H), 6.25 (d, *J* = 9.5 Hz, 1H), 4.13 (q, *J* = 7.0 Hz, 2H), 4.02 (t, *J* = 6.5 Hz, 2H), 2.30 (t, *J* = 7.5 Hz, 2H), 1.82 (qn, *J* = 7.5 Hz, 2H), 1.63 (at, *J* = 6.5 Hz, 2H), 1.47 (m, 2H), 1.31 (br s, 10), 1.26 (t, *J* = 7.5 Hz, 3H).

11-(2-oxo-2*H*-chromen-7-yloxy)undecanoic acid. (4.1) Ethyl 11-(2-oxo-2*H*-chromen-7-yloxy)undecanoate (1.16 g, 3.08 mmol) was added to NaOH (1.23g, 10 equiv) in a solvent mixture (1:1) of dioxane and water. The reaction was allowed to go for 12 h at room temperature. The solvent volume was reduced by rotatory evaporation followed by the addition of water. The pH was adjusted to 3 using 1 M HCl to precipitate the crude product. The resulting precipitate was recrystallized from an EtOH/hexanes mixture (0.844 g, 79%). ^{1}H NMR (500 MHz, CD_3OD): δ 7.89 (d, *J* = 9.5 Hz, 1H), 7.54 (d, *J* = 8.5 Hz, 1H), 6.93 (d, *J* = 8.5 Hz, 1H), 6.91 (s, 1H), 6.25 (d, *J* = 9.5 Hz, 1H), 4.08 (t, *J* = 6.0 Hz, 2H), 2.28 (t, *J* = 7.5 Hz, 2H), 1.83 (qn, *J* = 6.5 Hz, 2H), 1.61 (at, *J* = 7.0 Hz, 2H), 1.51 (qn, *J* = 7.5 Hz, 2H), 1.35 (br s, 10H). ^{13}C NMR (100 MHz, $CDCl_3$): δ 179.8, 162.6, 161.6, 156.1, 143.7, 128.9, 113.2, 113.1, 112.6, 101.5, 68.8, 34.2, 29.5, 29.1, 26.1, 24.9.

3-(2-oxo-2*H*-chromen-7-yloxy)propanoic acid. (4.2) **3-**Bromopropionic acid (2.0 g, 13 mmol) was added to 7-hydroxycoumarin (2.06 g, 1 equiv), K_2CO_3 (5.42 g, 3 equiv), 18-crown-6 (0.35 g, 0.1 equiv) and refluxed for 2 h in acetonitrile. The solution was washed with ethyl acetate and the aqueous fraction was collected and precipitated with 1 M HCl. (1.28 g, 41.6%) ^{1}H NMR (500 MHz, CD_3OD): δ 7.89 (d, *J* = 9.5 Hz, 1H), 7.54 (d, *J* = 8.5 Hz, 1H), 6.96 (d, *J* = 2.5 Hz, 1H), 6.94 (s, 1H), 6.26 (d, *J* = 10 Hz, 1H), 4.34 (t, *J* = 6.0 Hz, 2H), 2.82 (t, *J* = 6.0 Hz, 2H). ^{13}C NMR (125 MHz, CD_3OD): δ 173.4, 162.5, 162.2, 155.9, 144.6, 129.3, 113.0, 113.0, 112.3, 101.2, 64.4, 33.8.

4.7.3 Instrumentation

Photoirradiation

All photoirradiations were conducted using a Model RPR-200 Rayonet photoreactor (The Southern New England Ultraviolet Company, Branford, Connecticut) fitted with ten 24 watt bulbs at 350 nm wavelength and six 35 watt bulbs at 254 nm wavelength. Samples were irradiated in quartz cuvettes with either of the two types of bulb sources.

Spectroscopy

UV-vis spectroscopy was performed using a Cary 500 Spectrometer for concentration and time-dependent irradiation experiments at room temperature. For photoirradiated experiments that involve cycling between 254 nm and 350 nm irradiation, the spectra were acquired using the same sample solution. A model J-715 Jasco CD Spectrometer was used for temperature-dependent CD experiments. Before data acquisition, all CD samples were allowed to equilibrate at the set temperature for 5 min and averaged over four runs. Data was collected from 400 to 190 nm. Concentrations for all samples unless otherwise noted were at 100 μM in water, using semi-micro 1 cm path-length quartz cuvettes. For photoirradiation experiments using spectroscopy, the samples were prepared in the cuvette, followed by irradiation.

Microscopy

AFM was performed on a DI SPM instrument using tapping mode on silicon substrates that were pre-washed with piranha cleaning solution, water, and isopropyl alcohol. Standard silicon AFM tips were purchased from Asylum Research (Santa Barbara, CA). Samples were prepared by drop casting 1 μL of a 0.1 wt% solution on to the substrate and then dried by evaporation at room temperature.

TEM was performed on a Hitachi H-8100 TEM using 200 keV accelerating voltage. Samples were prepared similarly to those described in the AFM procedure by drop-casting 1 μL of 0.1 wt% PA solution on to a carbon-coated copper grid (SPI Supplies, West Chester, PA). The samples on the grid were stained for 1–5 min in a 2% PTA solution or 30 min using a 2% uranyl acetate solution and the excess staining solution was wicked away. The grid was gently rinsed in water, blotted dry, and allowed to further dry at room temperature.

4.7.4 Cell Experiments

SKBr-3 cells were generously provided by Stephen Soukasene and grown through three passages using McCoy's media (Lonza, Allendale, NJ). Cells were counted using a hemacytometer, strained with trypan blue (Gibco, Invitrogen, Carlsbad, CA). For experimental preparation, cells were trypsinized and plated on a 24-well culture dish either coated or not with filtered (0.2 μm) peptide amphiphile substrates. Each well contained was calculated to contain approximately 20,000 cells. Experimental controls included media only samples, free 7-hydroxycoumarin, and a non-coumarin PA of a similar molecular structure. Proliferation assays were done after 2 days using a Live/Dead kit (Molecular Probes, Carlsbad, CA) and observed under a Nikon TE200 Eclipse microscope.

4.7.5 Supplementary

Table 4.1. Mass spectrometry of PA **18** and **19**.

PA	Mass Expected	Mass Observed
18	1027.43	1028.86
19	1281.71	1282.32

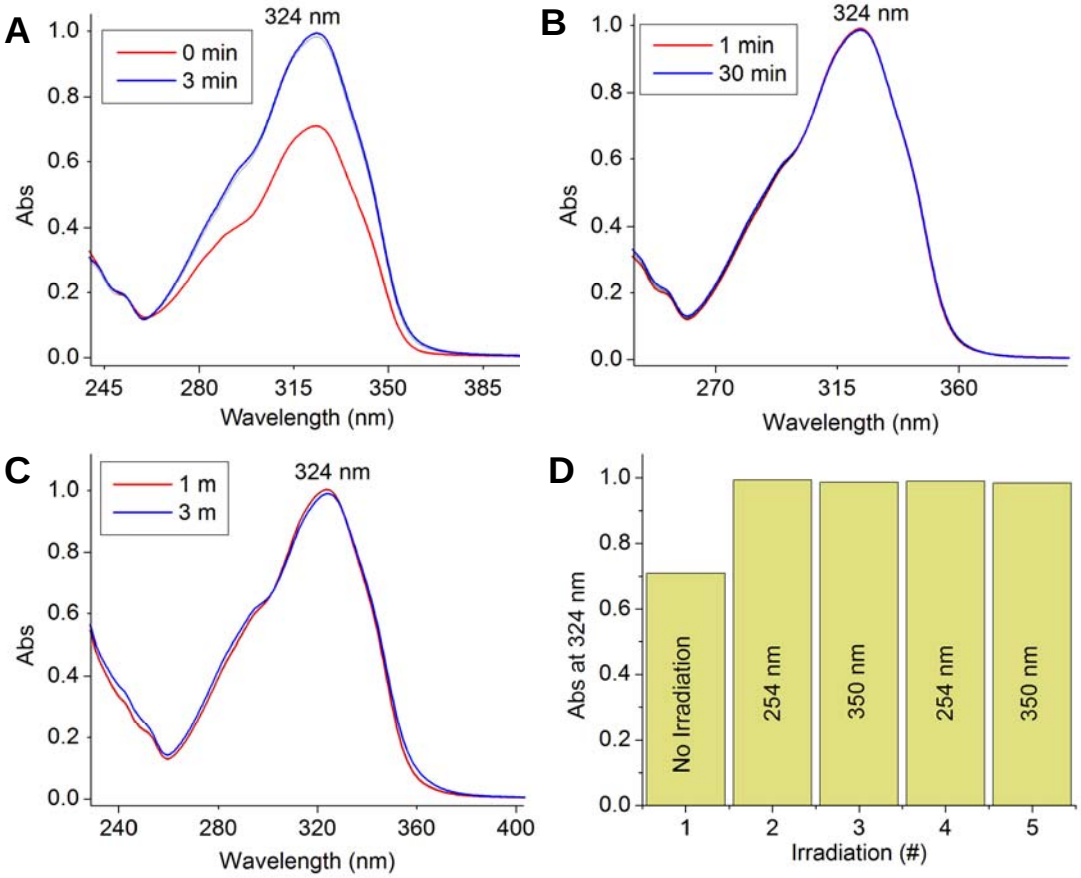

Figure 4.15. Photoirradiation of PA **18** in methanol. **A**) 254 nm irradiation of PA **18. B**) 350 nm irradiation of PA **18** up to 30 min. **C**) Second cycle of irradiation at 254 nm. **D**) Bar graph of absorbance intensity at 324 nm plotted after each irradiation phase. It should be noted that the second cycle of 324 nm irradiation (5) was for 30 min.

Chapter 5: Peptide Amphiphiles with Complementary Hydrogen Bonding Motifs

The interest in synthesizing PAs containing complementary hydrogen-bonding motifs stems from the objective of controlling hierarchical ordering of supramolecular structures. From a materials perspective, the addition of complementary hydrogen-bonding groups on to the PA molecule may be a useful strategy for the development of more robust materials with potential biofunctionality as DNA binding agents. These types of complementary PAs have not been synthesized before, and these hydrogen-bonding subunits will be incorporated to see whether this adds to our bottom-up strategy of using self-assembly towards the engineering of larger, robust, and functional constructs.

5.1 Introduction and Background

Complementary hydrogen bonds have been highly utilized for specific molecular recognition and its relatively strong binding forces in order to achieve and maintain robust supramolecular self-assemblies with potential functionalities involving chemical information storage and processing.[190-192] Much of the inspiration behind the design of synthetic hydrogen-bonding motifs originated from mimicking Nature's use of purines and pyrimidines as well as amino acids and glycogen derivatives for generating hierarchical, functional structures. High selectivity and complementarity occurs by incorporating an array of hydrogen-bond donors and acceptors on to a molecule. The organization of these arrays influences which complementary molecule it will most favorably bind to it.[193] In a purely hydrogen-bonded, self-assembled system, the interaction between two complementary molecules would obviously increase by

strategically adding another hydrogen bond between the two. However, the potential for hydrogen bonding mismatches depending on solvent type and concentration requires the inclusion of other noncovalent interactions in order create highly ordered, robust macromolecular assemblies.

Nucleoamphiphiles are amphiphilic molecules containing nucleobases on to the terminal end of a phosphoalkyl tail. Variations of these molecules include changing the placement and length of the alkyl tail. Doubly branched alkyl segments containing nucleobases typically form large vesicles[194] or worm-like micelles[53, 195] which show interesting applications as DNA delivery vehicles. Nucleoamphiphiles containing a single alkyl tail and a single nucleotide have been observed to form nanofibers, ribbons, helical cylinders, as well as vesicles.[53] Vernille et al. have recently described the synthesis and molecular recognition of DNA strands using peptide nucleic acid (PNA) amphiphiles.[196] Although these PNA amphiphiles by themselves form micellular aggregates, hybridization between the PNA nucleotides and the complementary DNA strand in solution still occurs. Nucleobase-glycosyl amphiphiles have also been examined and found to bind to double-stranded DNA.[197, 198] Research of nucleobase-peptide amphiphiles, which relies on the secondary structures formed by amino acids to define the self-assembled morphology, is still relatively new. This chapter will be discuss the effects of mixing complementary nucleobase-PAs (NPAs).

In this chapter, the synthesis and investigation of NPAs will be discussed, investigating the molecular and supramolecular interactions between two complementary NPA molecules as well as investigating any binding interactions between oligonucleotides and an NPA system. The surface of a nanofiber densely covered with nucleobases should favor hydrogen-bonding

interaction with its complementary molecule. This could yield novel, robust materials as well as have potential applications as a DNA or RNA binding agent.

5.2 Synthesis: Adenine- and Thymine-Peptide Amphiphiles

Before the synthesis of the nucleobase PAs, the synthesis of sulfamide- and urea-containing peptide amphiphiles was the first attempt at making complementary H-bonding PAs. In literature, sulfamide–urea interactions have been harnessed to for macromolecule capsules[199] and was initially chosen for this project due to their high binding affinity (K_a = 50 M^{-1} in CD_2Cl_2)[200] to its counterpart. Intermediates of the sulfamide and urea derivates were attempted for future incorporation on to a PA molecule by SPPS as shown in Figure 5.1. The synthesis of the sulfamide derivative involved coupling 3,4-diaminobenzoic acid to sulfamide. Several attempts involved solvent variation, protecting the carboxylic acid, as well as changing the

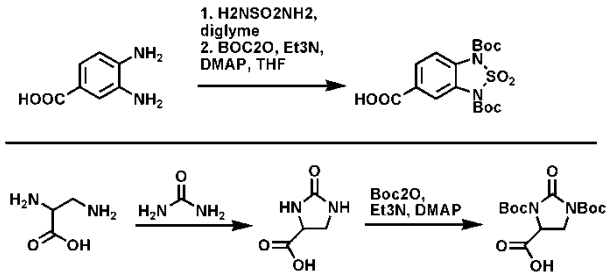

Figure 5.1. Synthetic attempts in making sulfamide (**top**) and urea (**bottom**) derivatives.

starting material to 3,4-diaminotoluene. Although crude NMR did show the potential presence of product, the poor solubility of the molecules made product isolation very challenging. The product purification was never successful. Synthesis of the urea compound containing a

carboxylic acid was also attempted by coupling 2,3-diaminopropionic acid to urea by following a literature protocol. This was also unsuccessful due to non-reactivity of the reaction and product isolation complications. The unsuccessful attempts in synthesizing urea- and sulfamide-containing resulted in the alternative choice of the currently proposed system.

Two different PAs containing either an adenine or thymine motif located at the charged terminal end of the molecule were designed and synthesized. For SPPS compatibility, commercially available thymine-1-acetic acid (**5.1** in Figure 5.2) used following the same Fmoc SPPS coupling strategy discussed previously in this thesis. The adenine molecule required additional derivatization for SPPS compatibility before being coupled on to the resin as the last residue.

For the adenine intermediate (**5.3**), the first reaction involved the addition of a carboxylic

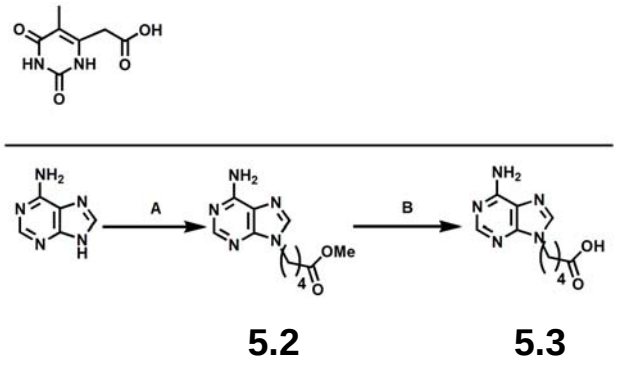

Figure 5.2. **Top**: Thymine derivative used for SPPS synthesis. **Bottom**: Adenine synthesis for SPPS usage. **A**) methyl 5-bromovalerate (1 equiv), NaH (1.2 equiv), DMF, 30 min at 60°C; **B**) KOH, EtOH, reflux 1 h.

handle for SPPS coupling, requiring deprotonation of the adenine at the *N*9 position and reacting it with methyl 5-bromopentanoate giving a 22% crude yield (**5.2**) as shown in Figure 5.2. This was followed by deprotection of the methyl group by refluxing in 1 M potassium hydroxide yielding the desired product (**5.3**, 15%). The low yields are most likely due to the low solubility

of the adenine molecule during the reactions. The product was precipitated by adjusting the pH to 1, deemed pure by NMR, and used for SPPS of the PA molecule. It should be noted that the original adenine synthesis scheme involved the attachment of a shorter carboxylic acid linker, methyl 2-bromoacetate. Although the adenine reaction was successful, the solubility was too low in polar aprotic solvents to provide efficient coupling to the resin during SPPS synthesis.

The selected PA sequence was Lys-Lys-Leu-Leu-Ala-Lys, with a palmitic alkyl tail attached to the epsilon amine of the *C*-terminal lysine residue (Figure 5.3). As the final coupling

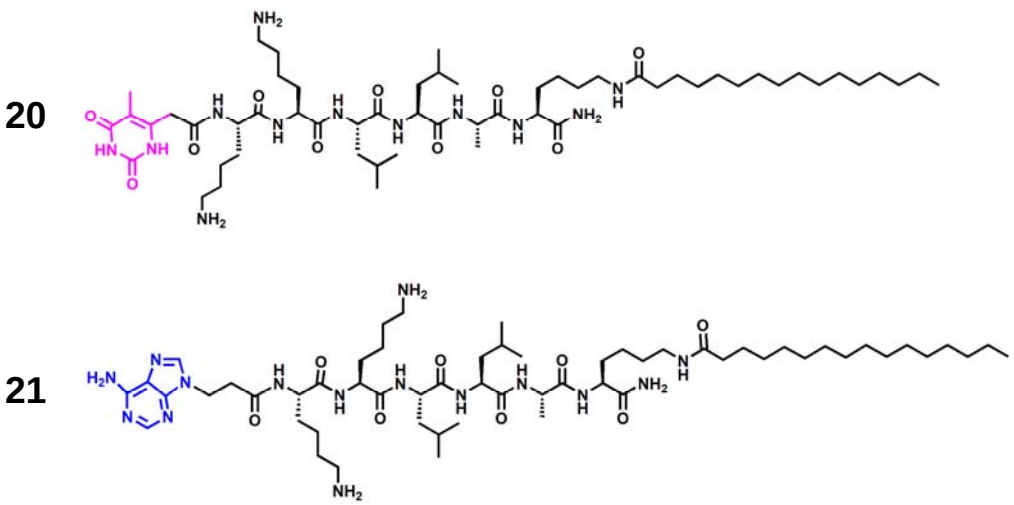

Figure 5.3. **Top**: Thymine PA (PA **20**) containing the peptide sequence- KKLLAK with a palmitic tail. **Bottom**: Adenine PA (PA **21**) containing the same peptide sequence as PA **20**.

step during the solid phase peptide synthesis, the nucleobase, adenine (**5.3**) or thymine (**5.1**), was added followed by acidic cleavage. After confirmation of the product using mass spectrometry, both PAs were purified by HPLC. The poor solubility of the thymine PA **20** required the HPLC diluent to include a 1:3 mixture of acetonitrile and water and approximately 5% trifluoroethanol (TFE). The crude solution of thymine PA was very viscous, which was most likely attributed to

the thymine-thymine hydrogen bonding between PA molecules. PA **21**, containing the adenine derivative, was purified under the typical methodology for PA purification. The HPLC fractions containing the product were confirmed by mass spectrometry, combined to a single fraction, lyophilized, and stored at -20°C until usage.

5.3 Investigating PA Nanofiber Interactions: Hydrogen Bonded?

Various spectroscopy, microscopy, mechanical, and gelation experiments were performed on PA **20** and **21** to determine any intra- or interfiber interactions, particularly hydrogen bonding. Experiments were done monitoring PA **20** alone, PA **21** alone, and the combination of both PAs in a 1:1 ratio. Because the orientation of the nucleotides are not limited by a typical DNA phosphate backbone, it is difficult to predict how the self-assembly of a dynamic supramolecular system would affect the nucleoside hydrogen bonding. Due to the flexibility of molecular arrangement in the PA nanofiber, the potential for different genres of base-pairing apart from the standard Watson–Crick bond, such the formation of Hoogsteen and reverse Hoogsteen bonds may also be present. The base-pairings of A:A, T:T, and A:T are known to occur with the greatest preference for the A:T base pair with a free energy of -4.3 kcal/mol[201] followed by preference for T:T then A:A base pairs. For these studies, the investigation regarding the types of hydrogen bonding and whether hydrogen bond is occurring between inter- or intrafiber molecules is very challenging due to the characterization limitations of individual molecules within a supramolecular structure; therefore, it is not within the scope of this work. With these PAs, the objective was to determine whether i) these PAs, when self-assembled, can form hydrogen bonds with other PA molecules and ii) how coassembly of the

complementary PAs would affect the supramolecular structure. Future work not discussed in this dissertation would also involve exploring the mechanical properties of the bulk material.

Gelation studies were initially done using 1 wt % solutions of PA **20**, PA **21**, and a 1:1 mixture of both in water. PA **20** and the 1:1 mixture formed clear viscous solutions while PA **21** formed a cloudy solution. No difference in the solution was observed after sonication. When heated, the solution of PA **20** became less viscous and the solution of PA **21** was less cloudy, however after allowing the solutions to cool for an hour at room temperature, the samples reverted back to the originally observed states. When exposed to a base chamber (ammonium hydroxide), all three samples became self-supporting, cloudy gels. The cloudiness from PA **21** is most likely due to the lower solubility of the adenine nucleoside located at the terminal end of the PA. The clear solution from the 1:1 mixture suggests the thymine PA (**20**) may help disperse and solubilize the adenine PA (**21**) aggregates due to the complementary hydrogen bonding.

Titration experiments by mixing two complementary PAs in solution was monitored by UV−vis spectroscopy to observe whether there was a difference between the sum of the individual PA spectra and the 1:1 mixed spectrum (Figure 5.4). The experiment involved 10 μM titrations of thymine PA into a 100 μM solution of the adenine PA (PA **21**) and vice versa. It should be noted that there was no annealing or sonication done during the titration process. The adenine PA alone displays an absorbance maximum at 262 nm and the thymine PA (PA **20**) at 270 nm. Figure 5.4 shows the final absorbances with a maximum at 265 nm when 1:1 mixtures of the two PAs are achieved. From these results, there appears to be no significant difference between the sum of the individual PA spectra and the non-annealed mixed solutions. In the case of significant base-pairing coupled with base-stacking, as typically observed during DNA

hybridization studies, one would have expected to observe a hypochromic effect where hybridized sequences absorb UV light less than single-stranded DNA. However, there was no observed decrease in the absorption maximum of the 1:1 mixed solutions compared to the sum of the individual PA spectrum. Melting profiles of the PAs from 80°C to 15°C were also done, monitoring UV absorption at 260 nm to watch for the presence of any melting transitions. Unfortunately there appeared to be no obvious melting transition with minimal change in the absorbance for all of the samples. The lack of a melting transition from these NPA nanofibers suggests reduced base-stacking compared to conventional oligonucleotide duplexes. Because there is no control regarding the type of base-pairing that can occur, this may result in multiple types of base-pairs with less than optimal base-stacking. These experiments have demonstrated

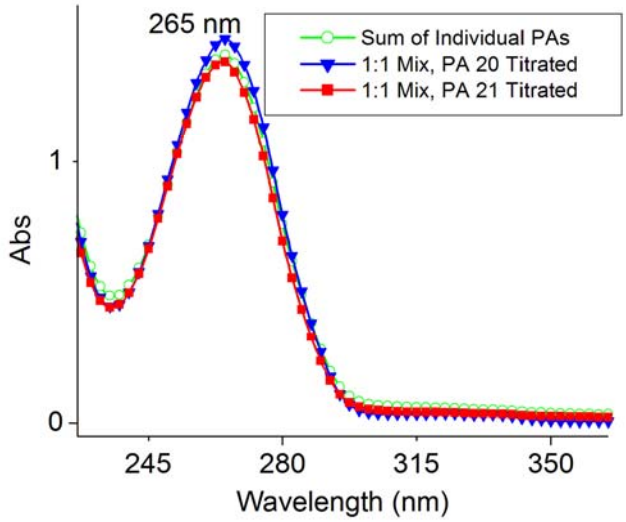

Figure 5.4. UV–vis spectrum of the final titration points of a resulting 1:1 mixture compared to the sum of the individual PA **20** and **21** spectra. The PA **21** spectrum with thymine PA titrations is represented as the blue triangle symbol. The PA **20** spectrum with adenine PA titrations is shown as the red square symbol.

the PAs do not exhibit typical hybridization with aromatic base-stacking observed for oligonucleotides.

A 5 day CD and UV–vis spectroscopic experiment was done to observe any base-pair interactions and β-sheet changes in either homogenous or mixed PA solutions. Samples of PA **20**, PA **21**, a 1:1 mixture of the 2 PAs, and a control PA (PA **22**) containing no nucleobase were initially annealed and monitored by CD followed by taking both UV and CD measurements of the samples for the next 5 days. The samples were initially heated from 10°C to 80°C and slowly cooled again to 10°C; although not shown, spectra of the samples were taken every 10°C.

After 5 days, there is some recovery of the β-sheet band. Figure 5.5A also the CD spectra of PA **21** during annealing. The slight increase in the β-sheet band at 222 nm during heating is most likely due to the improved solubility of the molecule at higher temperatures, the solubility of PA **21** is poor due to the adenine nucleobase. A broad positive band at 270 nm is attributed to the adenine base-stacking. Figure 5.5B shows the CD spectra of PA **20** at the annealing points of 10°C and 80°C. Two bands at 222 nm and 275 nm are attributed to the β-sheet and possible thymine base-stacking, respectively. During annealing there is minimal change in the thymine band, but the process appears to weaken the β-sheet structure as shown by the steady decrease in band intensity at 222 nm. The spectrum of the mixture containing 50 μM of each PA (Figure 5.5C) displays the expected β-sheet band at 225 nm and a negative band at 285 nm which does not match either CD spectra of PA **20** or PA **21**. Because the sum of the individual PA spectra does not match the observed spectrum of the 1:1 mixture, this suggests nucleobase interactions between the two PAs. Similar to the spectra observed for PA **20**, the mixed system also loses its β-sheet intensity during annealing. After the annealing process, the samples were systematically

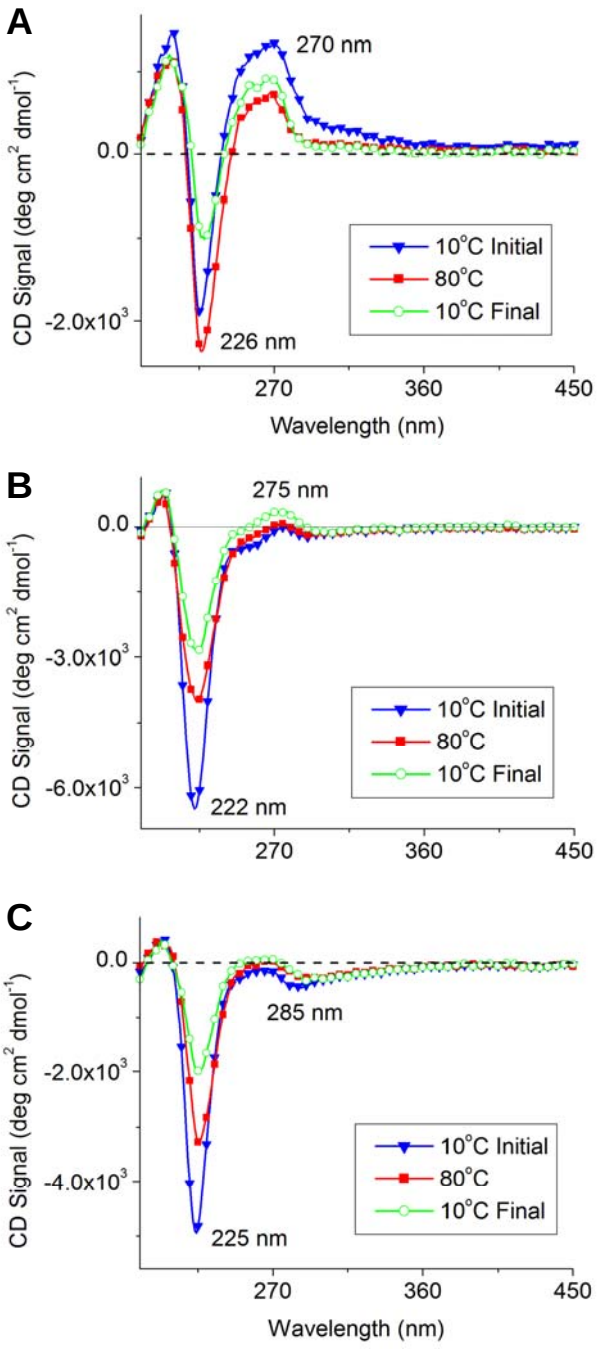

Figure 5.5. Temperature-dependent CD spectra of the PAs (**20**, **21**) and the 1:1 mixture at 10°C and 80 °C during an annealing cycle. **A**) Thymine PA (100 μM) **B**) Adenine PA (100 μM) **C**) 1:1 mixture of the two PAs (100 μM total).

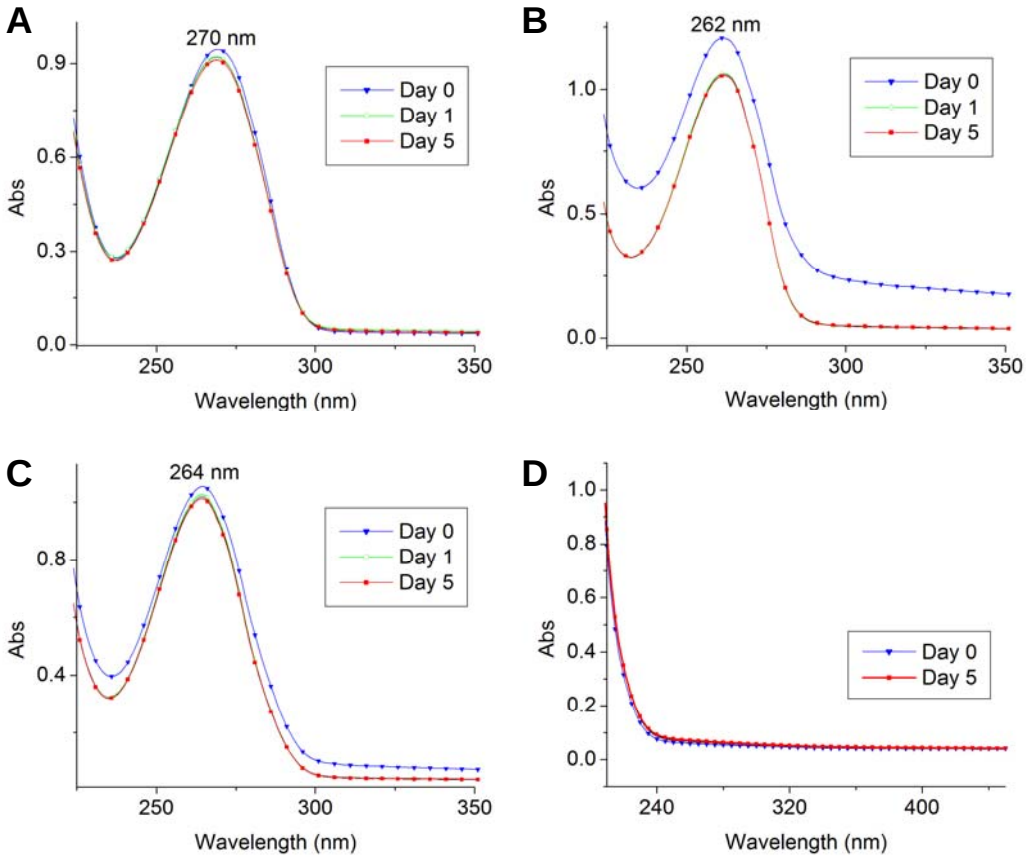

Figure 5.6. UV−vis spectra of the PAs (**20**, **21**), the 1:1 mixture, and the control PA **22** over a 5 day period. The samples were measured every 24 hours. **A**) Thymine PA (100 μM) **B**) Adenine PA (100 μM) **C**) 1:1 mixture of PA **20**:PA **21** (100 μM total). **D**) Control PA. Note that day 0 in prior to annealing, and the annealing was done once at day 0.

monitored over a 5 day period by UV and CD spectroscopy.

Over the 5 days, the UV−vis spectra monitored over a 5 day period by UV and CD spectroscopy. Over the 5 days, the UV−vis spectra f the 3 solutions all showed a small decrease in absorbance one day after annealing, suggesting some base-stacking among PAs (Figure 5.6). As previously noted, the reduced solubility of the UV−vis spectra, no change is observed after

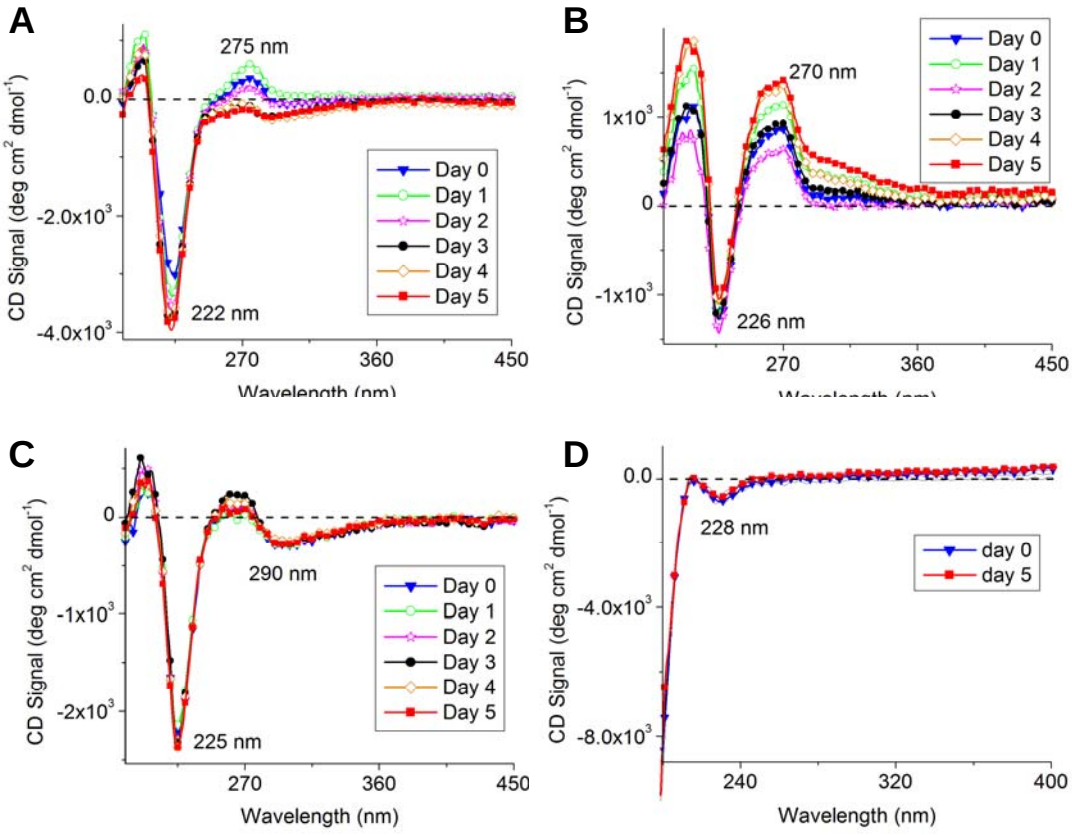

Figure 5.7. CD spectra of the PAs (**20**, **21, 22**) and the 1:1 mixture, over a 5 day period. The samples were measured every 24 hours. **A**) Thymine PA (100 μM) **B**) Adenine PA (100 μM) **C**) 1:1 mixture of PA **20**:PA **21** (100 μM total) **D**) Control PA.

day 0. The 5-day CD spectra of the each solution display the dynamic behavior of these supramolecular systems (Figure 5.7). Both spectra of PA **20** and PA **21** show spectral fluctuations of their respective nucleobase CD band throughout the 5 days, although their band signatures remain the same. Interestingly, the 1:1 mixture shows the least degree of spectral change throughout the 5 days, which could be due to improved stability of the supramolecular structures from the complementary nucleobases. The control PA **22** shows no significant CD

change as expected throughout the 5 days displaying a mixture of random coil and β-sheet structures.. Interestingly, the enhanced β-sheet intensity of the nucleobase PAs compared to the control PA must be correlated to nucleobase interactions, further stabilizing the peptidic secondary structure.

FTIR was also attempted to monitor the 1500–1800 cm^{-1} in-plane double-bond vibrations of the nucleobases to determine if hydrogen bonds were formed between the nucleobases. However, the strong presence of hydrogen bonding from the β-sheets of PA **20** and **21**, primarily exhibiting the amide I band at 1620 cm^{-1} overwhelmed any definitive signals from base-paired hydrogen bonds.

AFM and TEM micrographs of the two PAs individually and mixed 1:1 were prepared in water with no annealing at a 0.1 wt% concentration. Figure 5.8 displays the fiber formation and bundling of all three samples in AFM (left) and TEM (right). The thymine PA (PA **20**) is able to form nanofibers several microns long and often forms bundles. The bundling displays the alignment of individual nanofibers parallel to each other. This is most likely due to the favorable interaction of the thymine nucleobases between nanofibers. The heights and diameter of the fibers for thymine PA nanofibers are 6–9 nm. The adenine PA (PA **21**) also shows the formation of micron-long nanofibers with significantly more nanofiber aggregation due to the attraction between adenine nucleobases, since adenine nucleobases can base stack as well as form hydrogen bonds. Although these fibers appear to aggregate more than the thymine PA nanofibers, they appear to form shorter nanostructures. As previously mentioned, thymine PA solutions appear viscous and clear unlike the adenine PA solutions which remain liquid-like and slightly cloudy. When correlating these TEM images with viscosity observations, the extensive

nanofiber networks formed by the thymine PA correlates with the observed viscosity. The short, large bundled aggregates of the adenine PAs are less conducive to form extensive nanofiber networks, also correlating with the observed cloudy non-viscous solution. The nanofiber height by AFM and diameters by TEM are 5–8 nm. The microscopy images of the 1:1 mixture, shown in Figure 5.8E and 5.8F, were prepared without sample annealing. As previously noted, addition of the cloudy adenine PA solution into the thymine PA solution appeared to disperse the adenine PA, resulting in a clear solution. The reduced bundling can also be observed by comparing TEM micrographs between the adenine PA micrograph (Figure 5.8D) and the micrograph of the PA mixture (Figure 5.8F). By TEM, the diameter of the mixed fibers are 6–9 nm. AFM images displayed significant aggregation on the substrate, making height measurements of individual nanofibers difficult. From the images of the mixed system, there seems to be no obvious difference between the nanofiber morphologies. The system appears to form longer networks with less bundling compared to the adenine PA alone. Although the mixing of the PAs still results in PA nanofibers with similar dimensions compared to the individual PAs, the lack of bundling observed from the adenine PA solution also supplements the fact that there is an attractive interaction between the complementary PAs. Although this discussion refers to the nanofibers as homogenous constructs of either PA **20** or PA **21**, there is the possibly some degree of coassembly within a single fiber could occur. However, probing this local exchange within a supramolecular system is nontrivial and is beyond the scope of this discussion.

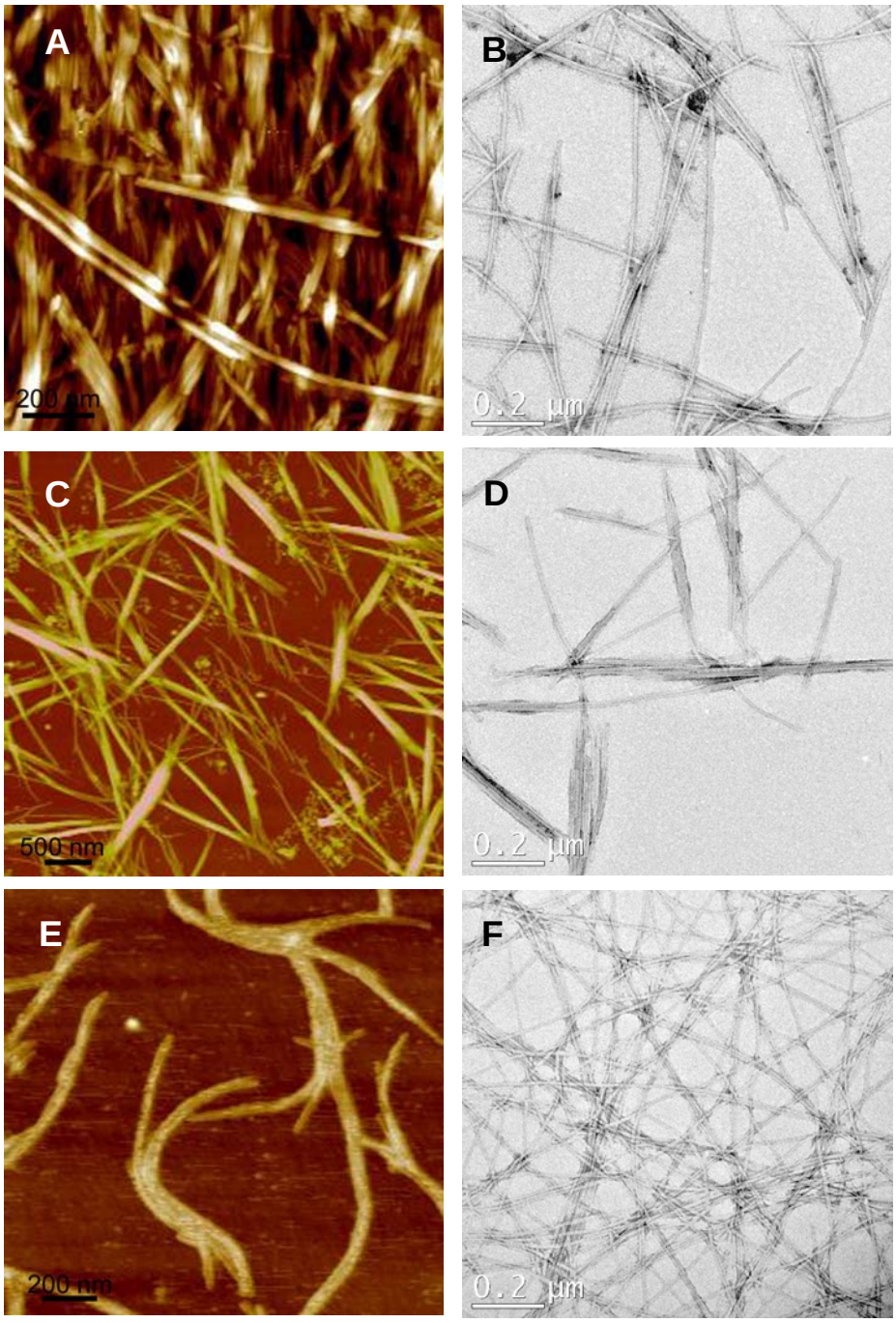

Figure 5.8. AFM (left) and TEM micrographs (right) of :**A–B**) Thymine PA (**20**), **C–D**) Adenine PA (**21**), **E–F**) 1:1 mixture of PA **20** and **21**. AFM samples were drop-casted on silicon wafers. TEM samples were stained with 2% uranyl acetate using 0.1 wt% samples in water.

5.4 PA Nanofibers in the Presence of Polymer DNA

In addition to generating larger, ordered, macromolecular systems, these nanofibers decorated with nucleobases may also be used to recognize and bind DNA or its other nucleotide derivatives. DNA-binding agents has been applied to oligonucleotide delivery, structure stabilization, and biosensing. As previously discussed, the characterization of the two PAs as individual and mixed solutions demonstrated nucleobase interactions while the nanofiber morphology was maintained throughout the various experiments. In this study, the introduction of polyadenylic acid (PolyA) to these PAs was done to examine any binding affinity between the PolyA and the nanofibers.

CD spectroscopy was initially done to characterize whether the introduction of PAs had an affect on the PolyA CD spectrum. The PolyA was dissolved in a 1 mg/mL concentration and centrifuged to remove any undissolved particulates. As shown in Figure 5.9, PolyA titration experiments were done with and without the presence of PAs (**20**, **21**, or **22**) in 20 mM NaPi solution. Without the presence any of PA, the PolyA showed strong characteristic positive CD signals at 220 and 264 nm, and negative CD signals at 207 and 247 nm. In the presence of thymine PA (Figure 5.9B), the spectra of the PA clearly dominates with very little resembling the previous CD signal of the PolyA even after the addition of 25 μL. Figure 5.10A shows the sum of the thymine PA and PolyA spectra do not match the mixed spectrum especially within the 240−265 nm region, and the loss of the PolyA signal suggests that its structure is disrupted when interacting with the thymine PA. The titration of PolyA into an adenine PA solution also shows the CD signal being dominated by the PA spectrum with little resemblance to the PolyA CD

signature. At 25 μL of PolyA, a shoulder at 247 nm and the positive CD band shift towards 270 nm may indicate the presence of some PolyA not interacting with the adenine PA. When PolyA

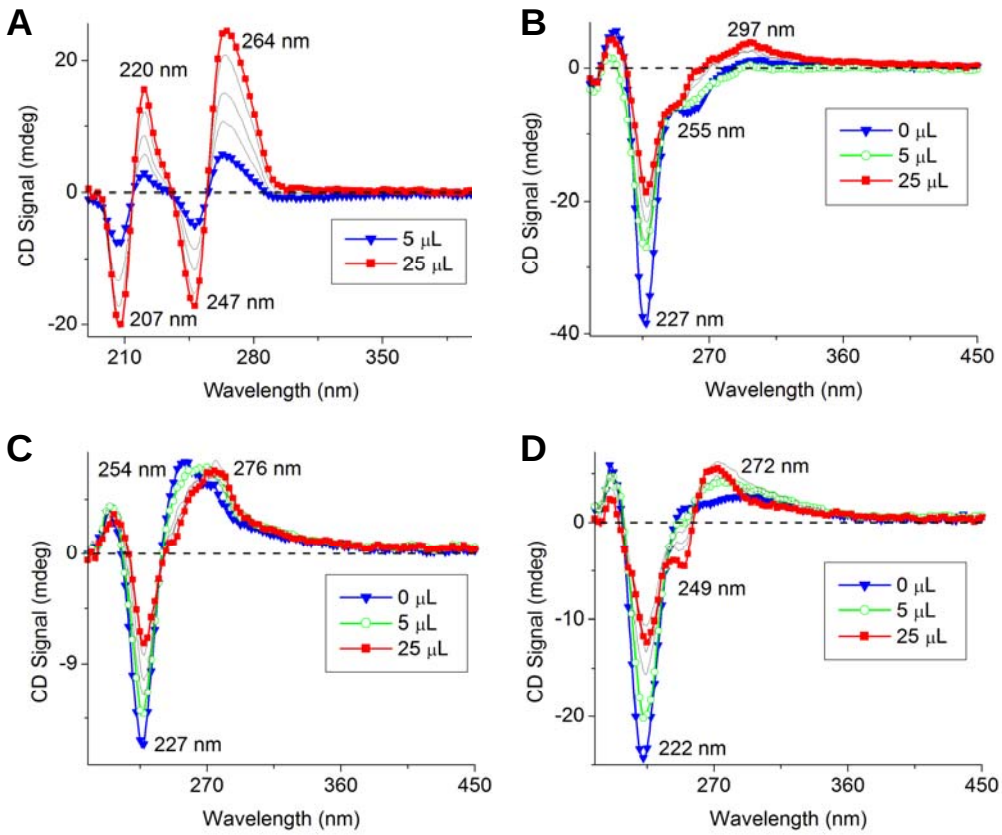

Figure 5.9. CD spectra of PolyA titrations with and without PAs. **A**) PolyA only. **B**) PolyA with Thymine PA (**20**). **C**) PolyA with Adenine PA (**21**). **D**) PolyA with Control PA (**22**). PolyA titrations were from a 1 mg/mL stock solution. CD samples were prepared 20 mM NaPi in water.

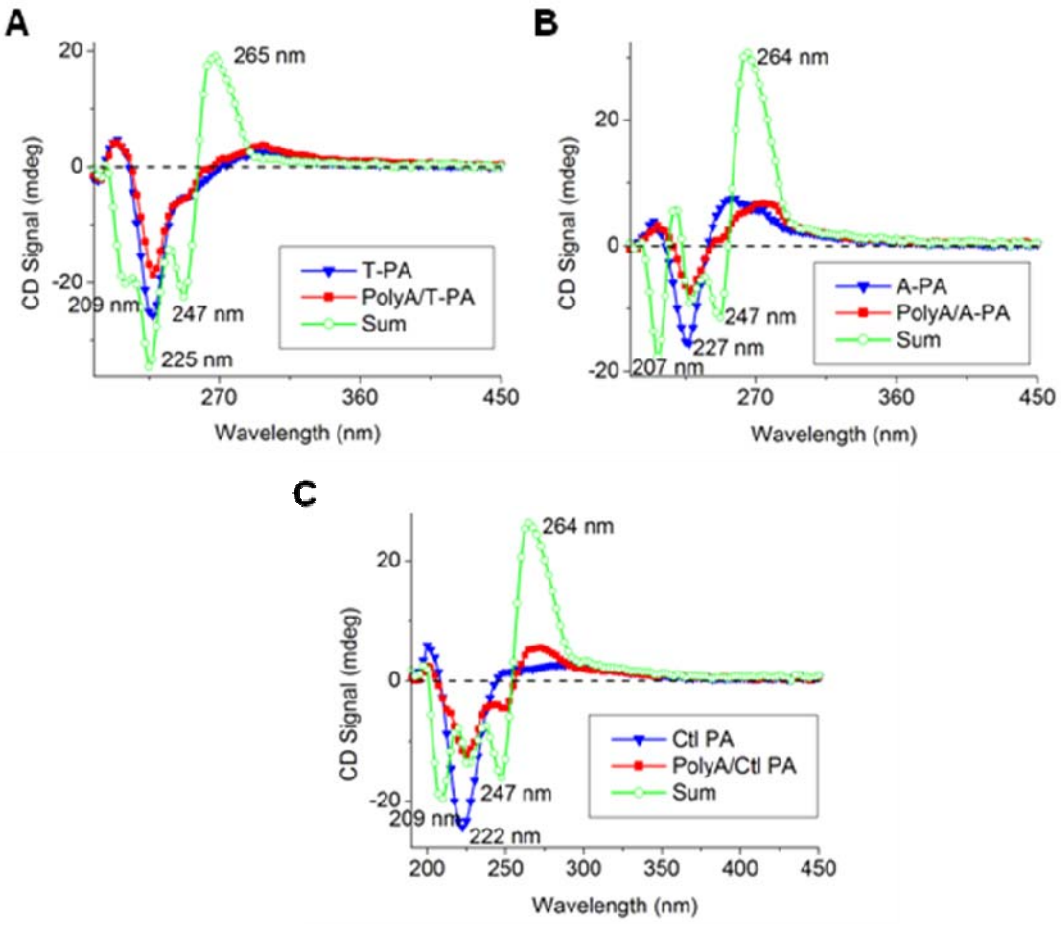

Figure 5.10. Comparing the sum of individual CD spectrum of PolyA with PA versus the CD spectrum of the mixture. **A**) PolyA with Thymine PA (**20**) **B**) PolyA with Adenine PA (**21**). **C**) PolyA with Control PA (**22**).

was titrated into the control PA solution, interestingly, the PolyA signal is not apparent until a total volume of 25 μL was titrated, showing the PolyA band at 247 nm and a broad CD band around 270 nm (Figure 5.9C). Although the control PA was originally expected to not interact with the PolyA, the CD signal of the mixture suggested some binding interaction was present. The interaction was most likely due to electrostatic attraction from the peripheral amines from the lysine side chains of the PA and the negatively charged backbone of the PolyA. Comparison of the three PAs' CD spectra with the presence of PolyA displays the loss of the PolyA CD signal, although higher concentrations of the PolyA with the control PA showed some recovery of the PolyA signal. This supports the hypothesis that NPAs interact more effectively with PolyA than by electrostatics alone.

TEM micrographs were taken to observe whether they PolyA caused any morphology changes when associated with the PAs. Each sample contained 25 μL of a 1 mg/mL PolyA solution and 100 μM of PA. It should be noted that there is a 4:1 excess of PA to PolyA by weight, so it should not be surprising to observe 'bare' PA nanofibers. The samples were stained with 2% uranyl acetate prior to imaging. PolyA, itself, did not appear to form any obvious nanostructures (Figure 5.11A), showing only dark amorphous aggregates. When mixed with the adenine PA, TEM micrographs showed typical nanofiber aggregates previously observed PA **21** alone (Figure 5.11B), but images of dark amorphous aggregates covering the nanofibers were also observed (Figure 5.11C), which could either be PolyA or excess uranyl acetate stain. It seems unlikely to be due to staining, the dark clusters only appear adhered to the nanofibers, whereas excess stain particles have no such preference and usually appear more crystalline. Figure 5.12A is a proposed model of PolyA aggregates adhering to the surface of the nanofiber

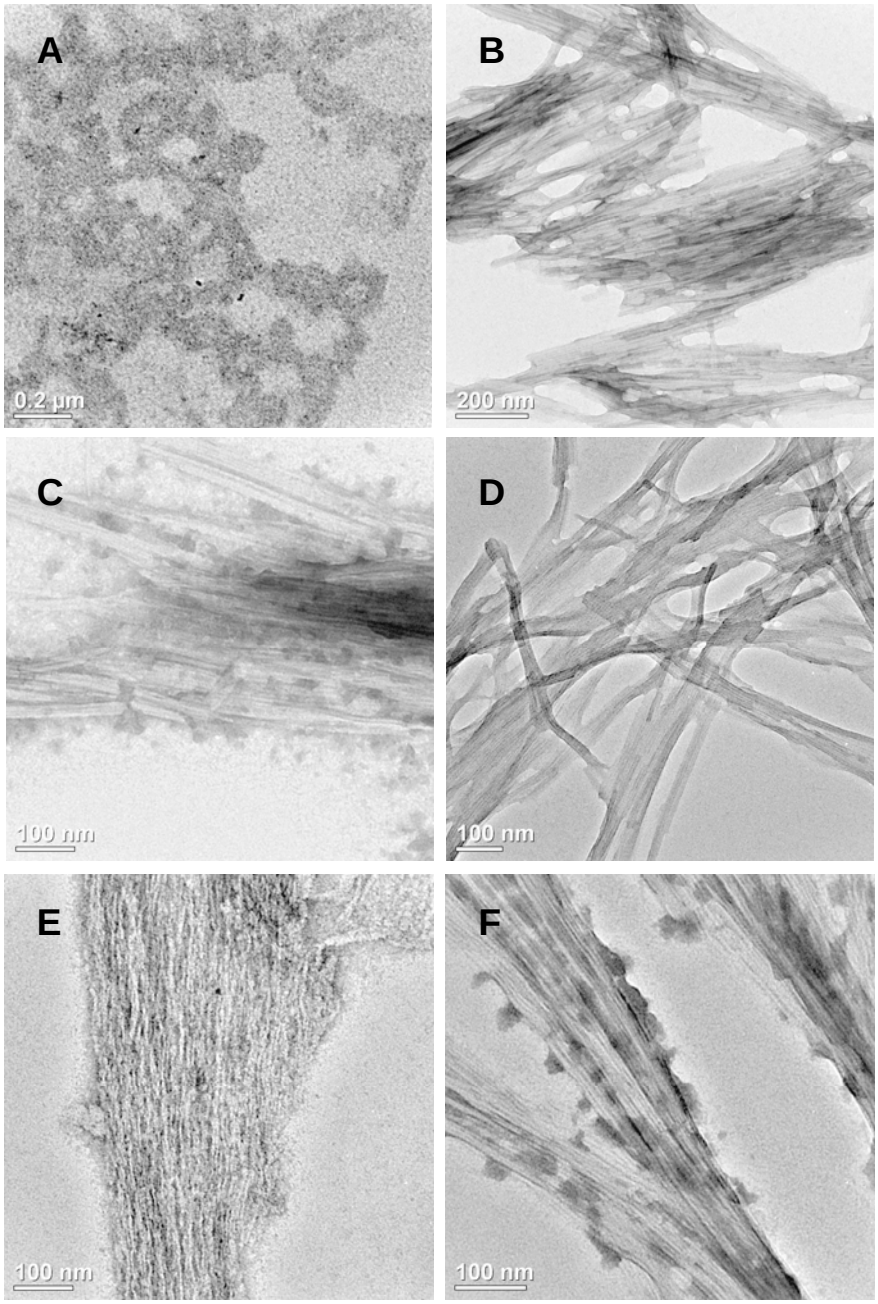

Figure 5.11. TEM micrographs of PolyA with or without PA. Samples were stained with 2% uranyl acetate. **A**) PolyA only. **B–C**) PolyA with Adenine PA (**21**). **D–E**) PolyA with Thymine PA (**20**). **F**) Poly A with Control PA (**22**).

bundles. The same observations were made with the control PA (Figure 5.11F). TEM images of thymine PA with PolyA also showed the typical thymine PAs (Figure 5.11D), but interestingly also showed non-uniform nanofiber-like structures, suggesting that the PolyA was coating the thymine PA nanofibers (Figure 5.11E). Unlike the other PAs, the PolyA appears to fully interact with the thymine PA by wrapping itself around the nanofiber as shown in the proposed schematic of Figure 5.12B. The approximate diameter of most of these nanofiber-like structures

bundles. The same observations were made with the control PA (Figure 5.11F). TEM images of thymine PA with PolyA also showed the typical thymine PAs (Figure 5.11D), but interestingly also showed non-uniform nanofiber-like structures, suggesting that the PolyA was coating the

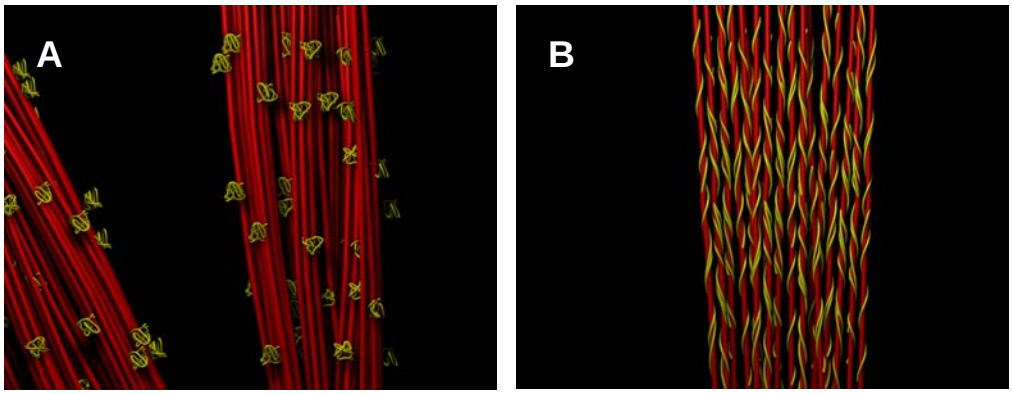

Figure 5.12. Proposed schematics of PolyA/nucleobase PA interactions. **A**) PolyA aggregates (yellow) adhere to PA nanofibers such as PA **21**. **B**) PolyA wrapping around a PA nanofiber, as observed between PolyA and PA **20**.

thymine PA nanofibers (Figure 5.11E). Unlike the other PAs, the PolyA appears to fully interact with the thymine PA by wrapping itself around the nanofiber as shown in the proposed schematic of Figure 5.12B. The approximate diameter of most of these nanofiber-like structures

is 6–7 nm. This difference may be due to the preferred interaction between the complementary nucleobases as well as the better solubility of the thymine PA compared to the adenine PA. Future work includes gel studies of the PA and PolyA mixtures to investigate the degree of DNA binding.

5.5 Conclusions

In summary, the incorporation of single nucleobases into the PA molecular structure has shown promise as another strategy to use in our bottom-up synthesis using self-assembly for the engineering of larger, robust constructs. These NPAs have also shown potential as a DNA binding agent, while still maintaining its nanostructured morphology. CD and microscopy studies showed significant interaction between these nucleobase PAs, most likely due to the hydrogen bonds formed between nanofibers. When the two complementary NPAs are combined, the thymine PA appears to disperse the adenine PA nanofiber aggregates, forming long nanofibers with extensive nanofiber networks which may improve the mechanical properties of the bulk material compared to PAs with no nucleobase functionality. In the presence of PolyA, both thymine and adenine PA bind to the polymer as shown by loss of the PolyA signature CD bands in the CD spectra. Microscopy of the thymine PA and the PolyA mixture also showed interesting ‘bumpy’ fiber morphology, suggesting that the biopolymer may be wrapping itself around the individual nanofibers. Future investigations are needed to investigate the morphologies of a mixed PolyA/PA system with an excess of the polymer. The mechanical behavior of each nucleobase PA with and without its complementary nucleobase-PA will also be included as future work. Currently, these NPAs are fundamentally interesting supramolecular

system inspired by the objective of creating controlled, functional, and well-ordered materials from the bottom-up. Further optimization of its molecular structure may also extend their applications towards being DNA binding agents.

5.6 Experimental

5.6.1 Materials

All amino acids and resins were purchased from Novabiochem Corporation (San Diego, CA), AnaSpec Corporation (San Jose, CA), and Advanced ChemTech (Louisville, KY). All other reagents and solvents for peptide synthesis were purchased from Sigma-Aldrich (St. Louis, MO) or Mallinckrodt (Hazelwood, MO) and used as provided. Sodium hydride and methyl 5-bromovalerate were purchased from Alfa Aesar. All other reagents for the synthesis of the adenine derivatives were purchased from Sigma-Aldrich and solvents were purchased from Mallinckrodt. All deuterated solvents were purchased from Cambridge Isotope Laboratories (Andover, MA). DNA was purchased from Integrated DNA Technologies, Inc. (Coralville, IA) and PolyA was purchased from Sigma-Aldrich and used as provided. The stock solution of DNA was prepared in a PBS buffer with 10 mM of EDTA and stored under frozen conditions. The polyadenylic acid (PolyA) was made into a stock solution at 1 mg/mL followed by centrifugation to remove any precipitates.

5.6.2 Synthesis

All PAs (**20** and **21**) were manually synthesized by Fmoc solid-phase peptide synthesis using orthogonal protecting strategies in 0.25 mmol scales. All PAs contain a C-terminal amide

group using Rink Amide MBHA resin. The final coupling step involved either coupling of the thymine **5.1** or adenine derivative **5.3** in the standard 4:4:6 equivalency including HBTU and DIEA, in DMF followed by standard acidic cleaving of the PA from the resin. Detailed synthesis protocols for peptide amphiphiles including RP-HPLC purification conditions may be viewed in the experimental section of Chapter 2. The RP-HPLC methodology for PA **20** was an exception, requiring a modified gradient run using an 88:12 initial solvent mixture of water to acetonitrile, both containing 0.1% TFA. The diluent for PA **20** was constituted of 5% TFE in a 3:1 mixture of water to acetonitrile.

Methyl 5-(6-amino-9*H*-purin-9-yl)pentanoate. (4.2) To adenine (2.00 g, 14.8 mmol) was slowly added NaH (0.422 g, 18 mmol) in DMF and stirred for 30 min at 60°C under nitrogen. A separate solution of methyl 5-bromovalerate was diluted in DMF and dripped into the adenine solution over 15 min. The reaction was allowed to run overnight at room temperature. The solution was washed with brine and extracted with ethyl acetate. The extracts were dried with $MgSO_4$ and rotovapped dry. The product was used without purification for the next step.

5-(6-Amino-9*H*-purin-9-yl)pentanoic acid. (4.3) To the crude reagent **4.2** was added 1 M potassium hydroxide and ethanol and refluxed for 1 h. The solution was precipitated, adjusting the pH to 2, using HCl. The white precipitate was found to be product (0.51 g, 14.7%). ^{1}H NMR (500 MHz, DMSO): δ 12.06 (s, 1H), 8.15 (s, 1H), 8.13 (s, 1H), 7.19 (s, 2H), 4.14 (t, J = 6.5 Hz, 2H), 2.25 (t, J = 7.5 Hz, 2H), 1.81 (qn, J = 8.0 Hz, 2H), 1.44 (qn, J = 8.0 Hz, 2H).

5.6.3 Instrumentation

Spectroscopy

UV-vis spectroscopy was performed using a Cary 500 Spectrometer or a 1050 Lambda Perkin Elmer Spectrometer for nucleotide monitoring. A model J-715 Jasco CD Spectrometer was used for temperature-dependent CD experiments to observe the β-sheet secondary structure and nucleobase CD signals. Before data acquisition, all CD samples were allowed to equilibrate at the set temperature for 5 min and averaged over four runs. Data was collected from 450 to 190 nm. Concentrations for all samples unless otherwise noted were at a total concentration of 100 μM in water, using semi-micro 1 cm path-length quartz cuvettes. Samples containing PAs with DNA (20 μM) and polyadenylic acid (5–25 μL from a 1 mg/mL stock solution) included 20 mM of sodium phosphate at a pH of ~7. The PolyA stock solution was divided and used from 100 μL aliquots. Concentrations of PolyA were confirmed by UV−vis spectroscopy (1027.6 ng/ 1 μL) (Nanodrop 1000, Thermo, Wilmington, DE).

Microscopy

AFM was performed on a DI SPM instrument using tapping mode on silicon substrates that were pre-washed with piranha cleaning solution, water, and isopropyl alcohol. Standard silicon AFM tips were purchased from Asylum Research (Santa Barbara, CA). Samples were prepared by drop casting 1 μL of a 0.1 wt% solution on to the substrate and then dried by evaporation at room temperature over time. Unless otherwise noted, the samples were not pre-annealed.

TEM was performed on a Hitachi H-8100 TEM using 200 keV accelerating voltage. Samples were prepared similarly to those described in the AFM procedure by drop casting 1 μL

of 0.1 wt% PA solution on to a carbon-coated copper grid (SPI Supplies, West Chester, PA). The samples on the grid were stained for 30 min using a 2% uranyl acetate solution and the excess staining solution was wicked away. The grid was gently rinsed in water, blotted dry, and allowed to further dry at room temperature. Unless otherwise noted, the samples were not pre-annealed.

5.6.4 Supplementary

Table 5.1. Mass spectrometry values of PA **20–22**.

PA	Mass Expected	Mass Observed
20	1103.48	1104.88
21	1154.58	1155.16
22	937.35	938.50

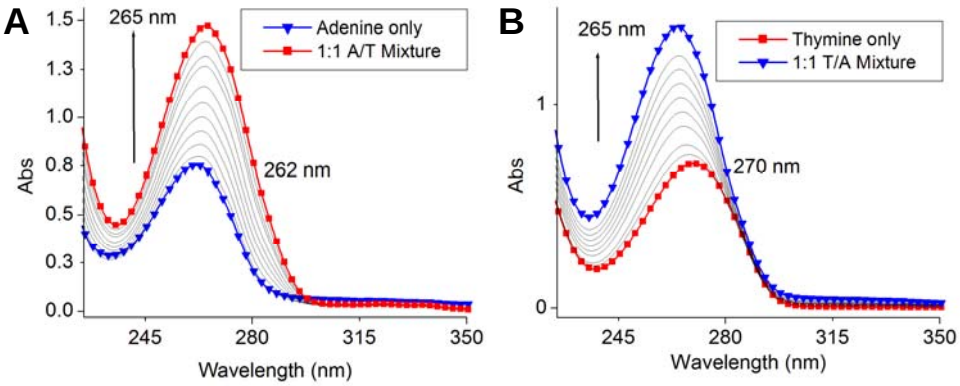

Figure 5.13. UV–vis spectroscopy of PA **20**, PA **21**, and titration of the complementary PA. **A**) Titration of PA **20** into PA **21**. **B**) Titration of PA **21** into PA **20**.

References

1. Douglas, T.; Young, M., Host-guest encapsulation of materials by assembled virus protein cages. *Nature* **1998,** 393, (6681), 152-155.

2. Lawrence, D. S.; Jiang, T.; Levett, M., Self-assembling supramolecular complexes. *Chemical Reviews* **1995,** 95, (6), 2229-2260.

3. Bong, D. T.; Clark, T. D.; Granja, J. R.; Ghadiri, M. R., Self-assembling organic nanotubes. *Angewandte Chemie-International Edition* **2001,** 40, (6), 988-1011.

4. Hoeben, F. J. M.; Jonkheijm, P.; Meijer, E. W.; Schenning, A., About supramolecular assemblies of pi-conjugated systems. *Chemical Reviews* **2005,** 105, (4), 1491-1546.

5. Turner, J. L.; Becker, M. L.; Li, X. X.; Taylor, J. S. A.; Wooley, K. L., PNA-directed solution- and surface-assembly of shell crosslinked (SCK) nanoparticle conjugates. *Soft Matter* **2005,** 1, (1), 69-78.

6. Paramonov, S. E.; Jun, H. W.; Hartgerink, J. D., Self-assembly of peptide-amphiphile nanofibers: The roles of hydrogen bonding and amphiphilic packing. *Journal of The American Chemical Society* **2006,** 128, (22), 7291-7298.

7. Martin, T.; Obst, U.; Rebek, J., Molecular assembly and encapsulation directed by hydrogen-bonding preferences and the filling of space. *Science* **1998,** 281, (5384), 1842-1845.

8. Muraoka, T.; Cui, H.; Stupp, S. I., Quadruple helix formation of a photoresponsive peptide amphiphile and its light-triggered dissociation into single fibers. *Journal of the American Chemical Society* **2008,** 130, (10), 2946-2947.

9. Hartgerink, J. D.; Beniash, E.; Stupp, S. I., Self-assembly and mineralization of peptide-amphiphile nanofibers. *Science* **2001,** 294, (5547), 1684-1688.

10. Beijer, F. H.; Sijbesma, R. P.; Kooijman, H.; Spek, A. L.; Meijer, E. W., Strong dimerization of ureidopyrimidones via quadruple hydrogen bonding. *Journal of the American Chemical Society* **1998,** 120, (27), 6761-6769.

11. Ghadiri, M. R.; Granja, J. R.; Milligan, R. A.; McRee, D. E.; Khazanovich, N., Self-assembling organic nanotubes based on a cyclic peptide architecture. *Nature* **1993,** 366, (6453), 324-327.

12. Bellomo, E. G.; Wyrsta, M. D.; Pakstis, L.; Pochan, D. J.; Deming, T. J., Stimuli-responsive polypeptide vesicles by conformation-specific assembly. *Nature Materials* **2004,** 3, (4), 244-248.

13. Hsu, L.; Cvetanovich, G. L.; Stupp, S. I., Peptide amphiphile nanofibers with conjugated polydiacetylene backbones in their core. *Journal of the American Chemical Society* **2008,** 130, (12), 3892-3899.

14. Lehn, J. M., Supramolecular Chemistry - Scope and Perspectives Molecules, Supermolecules, and Molecular Devices. *Angewandte Chemie-International Edition in English* **1988,** 27, (1), 89-112.

15. Desiraju, G. R., Chemistry beyond the molecule. *Nature* **2001,** 412, (6845), 397-400.

16. Lehn, J. M., Supramolecular Chemistry. *Science* **1993,** 260, (5115), 1762-1763.

17. Lehn, J. M., Toward self-organization and complex matter. *Science* **2002,** 295, (5564), 2400-2403.

18. Zeng, F. W.; Zimmerman, S. C., Dendrimers in supramolecular chemistry: From molecular recognition to self-assembly. *Chemical Reviews* **1997,** 97, (5), 1681-1712.

19. Alivisatos, A. P.; Barbara, P. F.; Castleman, A. W.; Chang, J.; Dixon, D. A.; Klein, M. L.; McLendon, G. L.; Miller, J. S.; Ratner, M. A.; Rossky, P. J.; Stupp, S. I.; Thompson, M. E., From molecules to materials: Current trends and future directions. *Advanced Materials* **1998,** 10, (16), 1297-1336.

20. Balzani, V.; Gomez-Lopez, M.; Stoddart, J. F., Molecular machines. *Accounts of Chemical Research* **1998,** 31, (7), 405-414.

21. van Esch, J. H.; Feringa, B. L., New functional materials based on self-assembling organogels: From serendipity towards design. *Angewandte Chemie-International Edition* **2000,** 39, (13), 2263-2266.

22. Whitesides, G. M.; Mathias, J. P.; Seto, C. T., Molecular self-assembly and nanochemistry - A chemical strategy for the synthesis of nanostructures. *Science* **1991,** 254, (5036), 1312-1319.

23. Schneider, H. J., Mechanisms of molecular recognition - Investigations of organic host guest complexes. *Angewandte Chemie-International Edition in English* **1991,** 30, (11), 1417-1436.

24. Fersht, A. R., The hydrogen-bond in molecular recognition. *Trends in Biochemical Sciences* **1987,** 12, (8), 301-304.

25. Desiraju, G. R., Hydrogen bridges in crystal engineering: Interactions without borders. *Accounts of Chemical Research* **2002,** 35, (7), 565-573.

26. Smithrud, D. B.; Sanford, E. M.; Chao, I.; Ferguson, S. B.; Carcanague, D. R.; Evanseck, J. D.; Houk, K. N.; Diederich, F., Solvent effects in molecular recognition. *Pure and Applied Chemistry* **1990,** 62, (12), 2227-2236.

27. Janiak, C., A critical account on pi-pi stacking in metal complexes with aromatic nitrogen-containing ligands. *Journal of the Chemical Society-Dalton Transactions* **2000**, (21), 3885-3896.

28. Meyer, E. A.; Castellano, R. K.; Diederich, F., Interactions with aromatic rings in chemical and biological recognition. *Angewandte Chemie-International Edition* **2003,** 42, (11), 1210-1250.

29. Fujita, M., Metal-directed self-assembly of two- and three-dimensional synthetic receptors. *Chemical Society Reviews* **1998,** 27, (6), 417-425.

30. Kramer, R.; Lehn, J. M.; Marquisrigault, A., Self-recognition in helicate self-assembly: Spontaneous formation of helical metal-complexes from mixtures of ligands and metal-ions. *Proceedings of the National Academy of Sciences of the United States of America* **1993,** 90, (12), 5394-5398.

31. Koert, U.; Harding, M. M.; Lehn, J. M., DNH Deoxyribonucleohelicates: Self-assembly of oligonucleosidic double-helical metal-complexes. *Nature* **1990,** 346, (6282), 339-342.

32. Williams, D. H.; Westwell, M. S., Aspects of weak interactions. *Chemical Society Reviews* **1998,** 27, (1), 57-63.

33. Kelly, J. W., The alternative conformations of amyloidogenic proteins and their multi-step assembly pathways. *Current Opinion in Structural Biology* **1998,** 8, (1), 101-106.

34. Wittung, P.; Nielsen, P. E.; Buchardt, O.; Egholm, M.; Norden, B., DNA-like double helix formed by peptide nucleic acid. *Nature* **1994,** 368, (6471), 561-563.

35. Jamroz-Piegza, M.; Walach, W.; Dworak, A.; Trzebicka, B., Polyether nanoparticles from covalently crosslinked copolymer micelles. *Journal of Colloid and Interface Science* **2008,** 325, (1), 141-148.

36. Hartgerink, J. D.; Beniash, E.; Stupp, S. I., Peptide-amphiphile nanofibers: A versatile scaffold for the preparation of self-assembling materials. *Proceedings of the National Academy of Sciences of the United States of America* **2002,** 99, (8), 5133-5138.

37. Zhang, S. G., Fabrication of novel biomaterials through molecular self-assembly. *Nature Biotechnology* **2003,** 21, (10), 1171-1178.

38. Aggeli, A.; Bell, M.; Boden, N.; Keen, J. N.; Knowles, P. F.; McLeish, T. C. B.; Pitkeathly, M.; Radford, S. E., Responsive gels formed by the spontaneous self-assembly of peptides into polymeric beta-sheet tapes. *Nature* **1997,** 386, (6622), 259-262.

39. Lehn, J. M., Toward complex matter: Supramolecular chemistry and self-organization. *Proceedings of the National Academy of Sciences of the United States of America* **2002,** 99, (8), 4763-4768.

40. Farrens, D. L.; Altenbach, C.; Yang, K.; Hubbell, W. L.; Khorana, H. G., Requirement of rigid-body motion of transmembrane helices for light activation of rhodopsin. *Science* **1996,** 274, (5288), 768-770.

41. Tanaka, M.; Suda, T.; Takahashi, T.; Nagata, S., Expression of the functional soluble form of human Fas ligand in activated lymphocytes. *Embo Journal* **1995,** 14, (6), 1129-1135.

42. Bragg, P. D.; Hou, C., A cross-linking study of the Ca2+, Mg2+-activated adenosine-triphosphatase of Escherichia-Coli. *European Journal of Biochemistry* **1980,** 106, (2), 495-503.

43. Denny, J. B.; Blobel, G., I-125-labeled crosslinking reagent that is hydrophilic, photoactivatable, and cleavable through an azo linkage. *Proceedings of the National Academy of Sciences of the United States of America* **1984,** 81, (17), 5286-5290.

44. Bleil, J. D.; Wassarman, P. M., Identification of a Zp3-binding protein on acrosome-intact mouse sperm by photoaffinity cross-linking. *Proceedings of the National Academy of Sciences of the United States of America* **1990,** 87, (14), 5563-5567.

45. van der Mee, M. A. J.; I'Abee, R. M. A.; Portale, G.; Goossens, J. G. P.; van Duin, M., Synthesis, structure, and properties of ionic thermoplastic elastomers based on maleated ethylene/propylene copolymers. *Macromolecules* **2008,** 41, (14), 5493-5501.

46. Schmidt, D. L.; Coburn, C. E.; Dekoven, B. M.; Potter, G. E.; Meyers, G. F.; Fischer, D. A., Water-based nonstick hydrophobic coatings. *Nature* **1994,** 368, (6466), 39-41.

47. Zhang, Q.; Remsen, E. E.; Wooley, K. L., Shell cross-linked nanoparticles containing hydrolytically degradable, crystalline core domains. *Journal of the American Chemical Society* **2000,** 122, (15), 3642-3651.

48. Yan, H.; Park, S. H.; Finkelstein, G.; Reif, J. H.; LaBean, T. H., DNA-templated self-assembly of protein arrays and highly conductive nanowires. *Science* **2003,** 301, (5641), 1882-1884.

49. Thuong, N. T.; Helene, C., Sequence-specific recognition and modification of double-helical DNA by oligonucleotides. *Angewandte Chemie-International Edition in English* **1993,** 32, (5), 666-690.

50. Niemeyer, C. M., Nanoparticles, proteins, and nucleic acids: Biotechnology meets materials science. *Angewandte Chemie-International Edition* **2001,** 40, (22), 4128-4158.

51. Seto, C. T.; Whitesides, G. M., Molecular self-assembly through hydrogen-bonding: Supramolecular aggregates based on the cyanuric acid-melamine lattice. *Journal of the American Chemical Society* **1993,** 115, (3), 905-916.

52. Murray, T. J.; Zimmerman, S. C., New triply hydrogen-bonded complxes with highly variable stabilities. *Journal of the American Chemical Society* **1992,** 114, (10), 4010-4011.

53. Johnson, D. W.; Hof, F.; Palmer, L. C.; Martin, T.; Obst, U.; Rebek, J., Glycoluril ribbons tethered by complementary hydrogen bonds. *Chemical Communications* **2003**, (14), 1638-1639.

54. Sijbesma, R. P.; Beijer, F. H.; Brunsveld, L.; Folmer, B. J. B.; Hirschberg, J.; Lange, R. F. M.; Lowe, J. K. L.; Meijer, E. W., Reversible polymers formed from self-complementary monomers using quadruple hydrogen bonding. *Science* **1997,** 278, (5343), 1601-1604.

55. Lowik, D.; van Hest, J. C. M., Peptide based amphiphiles. *Chemical Society Reviews* **2004,** 33, (4), 234-245.

56. Ghadiri, M. R.; Granja, J. R.; Buehler, L. K., Artificial Transmembrane Ion Channels from Self-Assembling Peptide Nanotubes. *Nature* **1994,** 369, (6478), 301-304.

57. Ghadiri, M. R.; Soares, C.; Choi, C., A Convergent Approach to Protein Design - Metal Ion-Assisted Spontaneous Self-Assembly of a Polypeptide into a Triple-Helix Bundle Protein. *Journal of the American Chemical Society* **1992,** 114, (3), 825-831.

58. Ghadiri, M. R.; Kobayashi, K.; Granja, J. R.; Chadha, R. K.; McRee, D. E., The Structural and Thermodynamic Basis for the Formation of Self-Assembled Peptide Nanotubes. *Angewandte Chemie-International Edition* **1995,** 34, (1), 93-95.

59. Zhang, S. G., Emerging biological materials through molecular self-assembly. *Biotechnology Advances* **2002,** 20, (5-6), 321-339.

60. Zhang, S. G.; Zhao, X. J., Design of molecular biological materials using peptide motifs. *Journal Of Materials Chemistry* **2004,** 14, (14), 2082-2086.

61. Schneider, J. P.; Pochan, D. J.; Ozbas, B.; Rajagopal, K.; Pakstis, L.; Kretsinger, J., Responsive hydrogels from the intramolecular folding and self-assembly of a designed peptide. *Journal of the American Chemical Society* **2002,** 124, (50), 15030-15037.

62. Zimenkov, Y.; Dublin, S. N.; Ni, R.; Tu, R. S.; Breedveld, V.; Apkarian, R. P.; Conticello, V. P., Rational design of a reversible pH-responsive switch for peptide self-assembly. *Journal of the American Chemical Society* **2006,** 128, (21), 6770-6771.

63. Minich, E. A.; Nowak, A. P.; Deming, T. J.; Pochan, D. J., Rod-rod and rod-coil self-assembly and phase behavior of polypeptide diblock copolymers. *Polymer* **2004,** 45, (6), 1951-1957.

64. Pochan, D. J.; Schneider, J. P.; Kretsinger, J.; Ozbas, B.; Rajagopal, K.; Haines, L., Thermally reversible hydrogels via intramolecular folding and consequent self-assembly of a de Novo designed peptide. *Journal of The American Chemical Society* **2003,** 125, (39), 11802-11803.

65. Neumann, R.; Ringsdorf, H., Peptide Liposomes From Amphiphilic Amino-Acids. *Journal of The American Chemical Society* **1986,** 108, (3), 487-490.

66. Murakami, Y.; Nakano, A.; Yoshimatsu, A.; Uchitomi, K.; Matsuda, Y., Characterization Of Molecular Aggregates Of Peptide Amphiphiles And Kinetics Of Dynamic Processes Performed By Single-Walled Vesicles. *Journal of the American Chemical Society* **1984,** 106, (12), 3613-3623.

67. Vauthey, S.; Santoso, S.; Gong, H. Y.; Watson, N.; Zhang, S. G., Molecular self-assembly of surfactant-like peptides to form nanotubes and nanovesicles. *Proceedings of the National Academy of Sciences of the United States of America* **2002,** 99, (8), 5355-5360.

68. Shimizu, T.; Masuda, M.; Minamikawa, H., Supramolecular nanotube architectures based on amphiphilic molecules. *Chemical Reviews* **2005,** 105, (4), 1401-1443.

69. Li, L.-S.; Jiang, H.; Messmore, B. W.; Bull, S. R.; Stupp, S. I., A Torsional Strain Mechanism to Tune Pitch in Supramolecular Helices. *Angewandte Chemie-International Edition* **2007,** 46, (31), 5873-5876.

70. Lear, J. D.; Wasserman, Z. R.; Degrado, W. F., Synthetic Amphiphilic Peptide Models For Protein Ion Channels. *Science* **1988,** 240, (4856), 1177-1181.

71. Lu, K.; Jacob, J.; Thiyagarajan, P.; Conticello, V. P.; Lynn, D. G., Exploiting amyloid fibril lamination for nanotube self-assembly. *Journal of the American Chemical Society* **2003,** 125, (21), 6391-6393.

72. Nowak, A. P.; Breedveld, V.; Pakstis, L.; Ozbas, B.; Pine, D. J.; Pochan, D.; Deming, T. J., Rapidly recovering hydrogel scaffolds from self-assembling diblock copolypeptide amphiphiles. *Nature* **2002,** 417, (6887), 424-428.

73. Niece, K. L.; Hartgerink, J. D.; Donners, J.; Stupp, S. I., Self-assembly combining two bioactive peptide-amphiphile molecules into nanofibers by electrostatic attraction. *Journal of the American Chemical Society* **2003,** 125, (24), 7146-7147.

74. Jiang, H. Z.; Guler, M. O.; Stupp, S. I., The internal structure of self-assembled peptide amphiphiles nanofibers. *Soft Matter* **2007,** 3, (4), 454-462.

75. Guler, M. O.; Soukasene, S.; Hulvat, J. F.; Stupp, S. I., Presentation and recognition of biotin on nanofibers formed by branched peptide amphiphiles. *Nano Letters* **2005,** 5, (2), 249-252.

76. Bull, S. R.; Guler, M. O.; Bras, R. E.; Venkatasubramanian, P. N.; Stupp, S. I.; Meade, T. J., Magnetic resonance imaging of self-assembled biomaterial scaffolds. *Bioconjugate Chemistry* **2005,** 16, (6), 1343-1348.

77. Bull, S. R.; Guler, M. O.; Bras, R. E.; Meade, T. J.; Stupp, S. I., Self-assembled peptide amphiphile nanofibers conjugated to MRI contrast agents. *Nano Letters* **2005,** 5, (1), 1-4.

78. Silva, G. A.; Czeisler, C.; Niece, K. L.; Beniash, E.; Harrington, D. A.; Kessler, J. A.; Stupp, S. I., Selective differentiation of neural progenitor cells by high-epitope density nanofibers. *Science* **2004,** 303, (5662), 1352-1355.

79. Rajangam, K.; Behanna, H. A.; Hui, M. J.; Han, X. Q.; Hulvat, J. F.; Lomasney, J. W.; Stupp, S. I., Heparin binding nanostructures to promote growth of blood vessels. *Nano Letters* **2006,** 6, (9), 2086-2090.

80. Cantow, H.-J., *Polydiacetylenes*. Springer-Verlag: Berlin, 1984; Vol. 63.

81. Kim, C. W. A.; Berg, J. M., Thermodynamic beta-sheet propensities measured using a zinc-finger host peptide. *Nature* **1993,** 362, (6417), 267-270.

82. Minor, D. L.; Kim, P. S., Measurement of the beta-sheet forming propensities of amino acids. *Nature* **1994,** 367, (6464), 660-663.

83. Tovar, J. D.; Claussen, R. C.; Stupp, S. I., Probing the interior of peptide amphiphile supramolecular aggregates. *Journal of the American Chemical Society* **2005,** 127, (20), 7337-7345.

84. Guler, M. O.; Claussen, R. C.; Stupp, S. I., Encapsulation of pyrene within self-assembled peptide amphiphile nanofibers. *Journal of Materials Chemistry* **2005,** 15, (42), 4507-4512.

85. Pytela, R.; Pierschbacher, M. D.; Ruoslahti, E., Identification and isolation of a 140-kD cell-surface glycoprotein with properties expected of a fibronectin receptor. *Cell* **1985,** 40, (1), 191-198.

86. Johnson, W. C., Protein secondary structure and circular dichroism - A practical guide. *Proteins-Structure Function and Genetics* **1990,** 7, (3), 205-214.

87. Fasman, G. D., *Prediction of Protein Structure and the Principles of Protein Conformation*. Plenum Press: New York, 1989.

88. Vetri, V.; Canale, C.; Relini, A.; Librizzi, F.; Militello, V.; Gliozzi, A.; Leone, M., Amyloid fibrils formation and amorphous aggregation in concanavalin A. *Biophysical Chemistry* **2007,** 125, (1), 184-190.

89. Imamoto, Y.; Tatsumi, S.; Harigai, M.; Yamazaki, Y.; Kamikubo, H.; Kataoka, M., Diverse roles of glycine residues conserved in photoactive yellow proteins. *Biophysical Journal* **2008,** 94, (9), 3620-3628.

90. Terpetschnig, E.; Szmacinski, H.; Lakowicz, J. R., Fluorescence polarization immunoassay of a high-molecular weight antigen based on a long-lifetime Ru-ligand complex. *Analytical Biochemistry* **1995,** 227, (1), 140-147.

91. Lo, C. M.; Wang, H. B.; Dembo, M.; Wang, Y. L., Cell movement is guided by the rigidity of the substrate. *Biophysical Journal* **2000,** 79, (1), 144-152.

92. Engler, A. J.; Sen, S.; Sweeney, H. L.; Discher, D. E., Matrix elasticity directs stem cell lineage specification. *Cell* **2006,** 126, (4), 677-689.

93. Wang, L.; Tiu, C.; Liu, T. J., Effects of nonionic surfactant and associative thickener on the rheology of polyacrylamide in aqueous glycerol solutions. *Colloid and Polymer Science* **1996,** 274, (2), 138-144.

94. Jackson, D. C.; ObrienSimpson, N.; Ede, N. J.; Brown, L. E., Free radical induced polymerization of synthetic peptides into polymeric immunogens. *Vaccine* **1997,** 15, (15), 1697-1705.

95. ObrienSimpson, N. M.; Ede, N. J.; Brown, L. E.; Swan, J.; Jackson, D. C., Polymerization of unprotected synthetic peptides: A view toward synthetic peptide vaccines. *Journal of the American Chemical Society* **1997,** 119, (6), 1183-1188.

96. Matsuda, A.; Sato, J.; Yasunaga, H.; Osada, Y., Order-disorder transition of a hydrogel conaining an N-alkyl acrylate. *Macromolecules* **1994,** 27, (26), 7695-7698.

97. Loyen, K.; Iliopoulos, I.; Audebert, R.; Olsson, U., Reversible thermal gelation in polymer surfactant systems - Control of the gelation temperature. *Langmuir* **1995,** 11, (4), 1053-1056.

98. Okano, T.; Bae, Y. H.; Jacobs, H.; Kim, S. W., Thermally on off switching polymers for drug permation and release. *Journal of Controlled Release* **1990,** 11, (1-3), 255-265.

99. Karino, T.; Masui, N.; Hiramatsu, M.; Yamaguchi, J.; Kurita, K.; Naito, S., Stabilization of hydrophobic domains in hydrogel by intermolecular hydrogen bonds between carboxylic groups at the distal end of alkyl side-chain. *Polymer* **2002,** 43, (26), 7467-7475.

100. Moore, J. S.; Stupp, S. I., Room-temperature polyesterification. *Macromolecules* **1990,** 23, (1), 65-70.

101. Solis, F. J.; Stupp, S. I.; de la Cruz, M. O., Charge induced pattern formation on surfaces: Segregation in cylindrical micelles of cationic-anionic peptide-amphiphiles. *Journal of Chemical Physics* **2005,** 122, (5), 054905.

102. Jonsson, S.; Sundell, P. E.; Hultgren, J.; Sheng, D.; Hoyle, C. E., Radiation chemistry aspects of polymerization and crosslinking. A review and future environmental trends in 'non-acrylate' chemistry. *Progress in Organic Coatings* **1996,** 27, (1-4), 107-122.

103. Morel, F.; Decker, C.; Jonsson, S.; Clark, S. C.; Hoyle, C. E., Kinetic study of the photo-induced copolymerization of N-substituted maleimides with electron donor monomers. *Polymer* **1999,** 40, (9), 2447-2454.

104. Miller, C. W.; Jonsson, E. S.; Hoyle, C. E.; Viswanathan, K.; Valente, E. J., Evaluation of N-aromatic maleimides as free radical photoinitiators: A photophysical and photopolymerization characterization. *Journal of Physical Chemistry B* **2001,** 105, (14), 2707-2717.

105. Hoyle, C. E.; Clark, S. C.; Jonsson, S.; Shimose, M., Photopolymerization using maleimides as photoinitiators. *Polymer* **1997,** 38, (22), 5695-5697.

106. Decker, C.; Morel, F.; Jonsson, S.; Clark, S.; Hoyle, C., Light-induced polymerisation of photoinitiator-free vinyl ether maleimide systems. *Macromolecular Chemistry and Physics* **1999,** 200, (5), 1005-1013.

107. Decker, C.; Bianchi, C.; Morel, F.; Jonsson, S.; Hoyle, C., Mechanistic study of the light-induced copolymerization of maleimide/vinyl ether systems. *Macromolecular Chemistry and Physics* **2000,** 201, (13), 1493-1503.

108. Jung, M. E.; Blum, R. B., Generation of enolate of acetaldehyde from non-carbonyl substances and its C-alkylation, O-alkylation, O-acylation and O-silation. *Tetrahedron Letters* **1977**, (43), 3791-3794.

109. Johnston, K. F.; Padias, A. B.; Hall, H. K., Synthesis of vinyloxy phosphorus monomers from the enolate of acetaldehyde. *Polymer Bulletin* **2000,** 45, (4-5), 359-364.

110. Kumpulainen, H.; Jarvinen, T.; Saari, R.; Lehtonen, M.; Vepsalainen, J., An efficient strategy for the synthesis of 1-chloroethyl phosphates and phosphoramidates. *Journal of Organic Chemistry* **2005,** 70, (22), 9056-9058.

111. Strekowski, L.; Lin, S. Y.; Lee, H.; Zhang, Z. Q.; Mason, J. C., Synthesis of 4-perfluoroalkylquinolines. *Tetrahedron* **1998,** 54, (28), 7947-7954.

112. Burget, D.; Mallein, C.; Fouassier, J. P., Visible light induced polymerization of maleimide-vinyl and maleimide-allyl ether based systems. *Polymer* **2003,** 44, (25), 7671-7678.

113. Tsou, K. C.; Barrnett, R. J.; Seligman, A. M., Preparation of some N-(1-naphthyl)-maleimides as sulfhydryl group reagents. *Journal of the American Chemical Society* **1955,** 77, (17), 4613-4616.

114. Percec, V.; Schlueter, D.; Ronda, J. C.; Johansson, G.; Ungar, G.; Zhou, J. P., Tubular architectures from polymers with tapered side groups. Assembly of side groups via a rigid helical

chain conformation and flexible helical chain conformation induced via assembly of side groups. *Macromolecules* **1996,** 29, (5), 1464-1472.

115. Fouassier, J. P.; Tieke, B.; Wegner, G., Photochemistry of the polymerization of diacetylenes in multilayers. *Israel Journal of Chemistry* **1979,** 18, (3-4), 227-232.

116. Tieke, B.; Lieser, G.; Wegner, G., Polymerization of diacetylenes in multilayers. *Journal of Polymer Science Part A-Polymer Chemistry* **1979,** 17, (6), 1631-1644.

117. Lauher, J. W.; Fowler, F. W.; Goroff, N. S., Single-crystal-to-single-crystal topochemical polymerizations by design. *Accounts of Chemical Research* **2008,** 41, (9), 1215-29.

118. Huo, Q.; Wang, S. P.; Pisseloup, A.; Verma, D.; Leblanc, R. M., Unusual chromatic properties observed from polymerized dipeptide diacetylenes. *Chemical Communications* **1999**, (16), 1601-1602.

119. Charych, D. H.; Nagy, J. O.; Spevak, W.; Bednarski, M. D., Direct Colorimetric Detection Of A Receptor-Ligand Interaction By A Polymerized Bilayer Assembly. *Science* **1993,** 261, (5121), 585-588.

120. Okada, S.; Peng, S.; Spevak, W.; Charych, D., Color and chromism of polydiacetylene vesicles. *Accounts of Chemical Research* **1998,** 31, (5), 229-239.

121. Reichert, A.; Nagy, J. O.; Spevak, W.; Charych, D., Polydiacetylene liposomes functionalized with sialic-acid bind and colorimetrically detect influenza-virus. *Journal of the American Chemical Society* **1995,** 117, (2), 829-830.

122. Spevak, W.; Nagy, J. O.; Charych, D. H., Molecular assemblies of functionalized polydiacetylenes. *Advanced Materials* **1995,** 7, (1), 85-89.

123. Jelinek, R., Colorimetric sensors for drug discovery and biomedical diagnostics. *Drug Development Research* **2000,** 50, (3-4), 497-501.

124. Kolusheva, S.; Boyer, L.; Jelinek, R., A colorimetric assay for rapid screening of antimicrobial peptides. *Nature Biotechnology* **2000,** 18, (2), 225-227.

125. Kolusheva, S.; Kafri, R.; Katz, M.; Jelinek, R., Rapid colorimetric detection of antibody-epitope recognition at a biomimetic membrane interface. *Journal of the American Chemical Society* **2001,** 123, (3), 417-422.

126. Kolusheva, S.; Shahal, T.; Jelinek, R., Cation-selective color sensors composed of ionophore-phospholipid-polydiacetylene mixed vesicles. *Journal of the American Chemical Society* **2000,** 122, (5), 776-780.

127. Kolusheva, S.; Zadmard, R.; Schrader, T.; Jelinek, R., Color fingerprinting of proteins by calixarenes embedded in lipid/polydiacetylene vesicles. *Journal of the American Chemical Society* **2006,** 128, (41), 13592-13598.

128. Orynbayeva, Z.; Kolusheva, S.; Livneh, E.; Lichtenshtein, A.; Nathan, I.; Jelinek, R., Visualization of membrane processes in living cells by surface-attached chromatic polymer patches. *Angewandte Chemie-International Edition* **2005,** 44, (7), 1092-1096.

129. Biesalski, M.; Tu, R.; Tirrell, M. V., Polymerized vesicles containing molecular recognition sites. *Langmuir* **2005,** 21, (13), 5663-5666.

130. Biesalski, M. A.; Knaebel, A.; Tu, R.; Tirrell, M., Cell adhesion on a polymerized peptide-amphiphile monolayer. *Biomaterials* **2006,** 27, (8), 1259-1269.

131. Ma, G. Y.; Cheng, Q., Vesicular polydiacetylene sensor for colorimetric signaling of bacterial pore-forming toxin. *Langmuir* **2005,** 21, (14), 6123-6126.

132. Cheng, Q.; Yamamoto, M.; Stevens, R. C., Amino acid terminated polydiacetylene lipid microstructures: Morphology and chromatic transition. *Langmuir* **2000,** 16, (12), 5333-5342.

133. Cheng, Q.; Stevens, R. C., Charge-induced chromatic transition of amino acid-derivatized polydiacetylene liposomes. *Langmuir* **1998,** 14, (8), 1974-1976.

134. Maynard, A. J.; Sharman, G. J.; Searle, M. S., Origin of beta-hairpin stability in solution: Structural and thermodynamic analysis of the folding of model peptide supports hydrophobic stabilization in water. *Journal of the American Chemical Society* **1998,** 120, (9), 1996-2007.

135. Huang, X.; Liu, M. H., Chirality of photopolymerized organized supramolecular polydiacetylene films. *Chemical Communications* **2003**, (1), 66-67.

136. Jahnke, E.; Lieberwirth, I.; Severin, N.; Rabe, J. P.; Frauenrath, H., Topochemical polymerization in supramolecular polymers of oligopeptide-functionalized diacetylenes. *Angewandte Chemie-International Edition* **2006,** 45, (32), 5383-5386.

137. Lee, S. J.; Kim, E.; Seo, M. L.; Do, Y.; Lee, Y. A.; Lee, S. S.; Jung, J. H.; Kogiso, M.; Shirnizu, T., Self-assembled helical ribbon and tubes of alanine-based amphiphiles induced by two different formation mechanisms. *Tetrahedron* **2008,** 64, (7), 1301-1308.

138. Lowik, D. W. P. M.; Shklyarevskiy, I. O.; Ruizendaal, L.; Christianen, P. C. M.; Maan, J. C.; van Hest, J. C. M., A highly ordered material from magnetically aligned peptide amphiphile nanofiber assemblies. *Advanced materials* **2007,** 19, 1191-1195.

139. Weiss, J.; Jahnke, E.; Severin, N.; Rabe, J. P.; Frauenrath, H., Consecutive conformational transitions and deaggregation of multiple-helical poly(diacetylene)s. *Nano Letters* **2008,** 8, (6), 1660-1666.

140. Reppy, M. A.; Pindzola, B. A., Biosensing with polydiacetylene materials: structures, optical properties and applications. *Chemical Communications* **2007**, 4317-4338.

141. Cai, M.; Mowery, M. D.; Menzel, H.; Evans, C. E., Fabrication of extended conjugation length polymers within diacetylene monolayers on Au surfaces: Influence of UV exposure time. *Langmuir* **1999,** 15, (4), 1215-1222.

142. Berrehar, J.; Lapersonne-Meyer, C.; Schott, M.; Weiser, G., A high energy exciton in polydiacetylene chains, involving electrons localized on the triple bond. *Chemical Physics* **2004,** 303, (1-3), 129-136.

143. Horvath, A.; Weiser, G.; LapersonneMeyer, C.; Schott, M.; Spagnoli, S., Wannier excitons and Franz-Keldysh effect of polydiacetylene chains diluted in their single crystal monomer matrix. *Physical Review B* **1996,** 53, (20), 13507-13514.

144. Deb, P.; Yuan, Z. Z.; Ramsey, L.; Hanks, T. W., Synthesis and optical properties of chiral polydiacetylenes. *Macromolecules* **2007,** 40, (10), 3533-3537.

145. Wilson, E. G., Electronic excitations of a conjugated polymer crystal. *Journal of Physics C-Solid State Physics* **1975,** 8, (5), 727-742.

146. Chothia, C., Conformation of twisted beta-pleated sheets in proteins. *Journal of Molecular Biology* **1973,** 75, 295-302.

147. Mori, T.; Shimoyama, K.; Fukawa, Y.; Minagawa, K.; Tanaka, M., Parallel beta-sheet as a novel template for polymerization of diacetylene. *Chemistry Letters* **2005,** 34, (1), 116-117.

148. Chao, C. Y.; Carvajal, D.; Szleifer, I.; Shull, K. R., Drop-shape analysis of receptor-ligand binding at the oil/water interface. *Langmuir* **2008,** 24, (6), 2472-2478.

149. Webber, R. E.; Creton, C.; Brown, H. R.; Gong, J. P., Large strain hysteresis and mullins effect of tough double-network hydrogels. *Macromolecules* **2007,** 40, (8), 2919-2927.

150. Shull, K. R.; Ahn, D.; Chen, W. L.; Flanigan, C. M.; Crosby, A. J., Axisymmetric adhesion tests of soft materials. *Macromolecular Chemistry and Physics* **1998,** 199, (4), 489-511.

151. Guvendiren, M.; Shull, K. R., Self-assembly of acrylic triblock hydrogels by vapor-phase solvent exchange. *Soft Matter* **2007,** 3, (5), 619-626.

152. Xia, Y. N.; Whitesides, G. M., Soft lithography. *Annual Review of Materials Science* **1998,** 28, 153-184.

153. Hung, A. M.; Stupp, S. I., Simultaneous self-assembly, orientation, and patterning of peptide-amphiphile nanofibers by soft lithography. *Nano Letters* **2007,** 7, (5), 1165-1171.

154. Odom, T. W.; Love, J. C.; Wolfe, D. B.; Paul, K. E.; Whitesides, G. M., Improved pattern transfer in soft lithography using composite stamps. *Langmuir* **2002,** 18, (13), 5314-5320.

155. Norman, J. J.; Collins, J. M.; Sharma, S.; Russell, B.; Desai, T. A., Microstructures in 3D Biological Gels Affect Cell Proliferation. *Tissue Engineering Part A* **2008**, 3, 379-390.

156. Mata, A.; Boehm, C.; Fleischman, A. J.; Muschler, G. F.; Roy, S., Connective tissue progenitor cell growth characteristics on textured substrates. *International Journal of Nanomedicine* **2007,** 2, (3), 389-406.

157. Mata, A.; Boehm, C.; Fleischman, A. J.; Muschler, G.; Roy, S., Growth of connective tissue progenitor cells on microtextured polydimethylsiloxane surfaces. *Journal of Biomedical Materials Research* **2002,** 62, (4), 499-506.

158. Yonezawa, N.; Yoshida, T.; Hasegawa, M., Symmetric and asymmetric photocleavage of the cyclobutane rings in head-to-head coumarin dimers and their lactone-opened derivatives. *Journal of the Chemical Society-Perkin Transactions 1* **1983**, (5), 1083-1086.

159. Yu, X. L.; Scheller, D.; Rademacher, O.; Wolff, T., Selectivity in the photodimerization of 6-alkylcoumarins. *Journal of Organic Chemistry* **2003,** 68, (19), 7386-7399.

160. Bergmann, G.; Jackson, P. O.; Hogg, J. H. C.; Stirner, T.; O'Neill, M.; Duffy, W. L.; Kelly, S. M.; Clark, G. F., Photoinduced changes of surface order in coumarin side-chain polymer films used for liquid crystal photoalignment. *Applied Physics Letters* **2005,** 87, (6).

161. Trenor, S. R.; Long, T. E.; Love, B. J., Development of a light-deactivatable PSA via photodimerization. *Journal of Adhesion* **2005,** 81, (2), 213-229.

162. Motoyanagi, J.; Fukushima, T.; Ishii, N.; Aida, T., Photochemical stitching of a tubularly assembled hexabenzocoronene amphiphile by dimerization of coumarin pendants. *Journal of the American Chemical Society* **2006,** 128, (13), 4220-4221.

163. Murray, R. D. H., Coumarins. *Natural Product Reports* **1989,** 6, (6), 591-624.

164. Rehman, S. U.; Chohan, Z. H.; Gulnaz, F.; Supuran, C. T., In-vitro antibacterial, antifungal and cytotoxic activities of some coumarins and their metal complexes. *Journal of Enzyme Inhibition and Medicinal Chemistry* **2005,** 20, (4), 333-340.

165. Finn, G. J.; Creaven, B. S.; Egan, D. A., Activation of mitogen activated protein kinase pathways and melanogenesis by novel nitro-derivatives of 7-hydroxycomarin in human malignant melanoma cells. *European Journal of Pharmaceutical Sciences* **2005,** 26, (1), 16-25.

166. Kostova, I., Synthetic and natural coumarins as cytotoxic agents. *Current Medicinal Chemistry - Anti-Cancer Agents* **2005,** 5, (1), 29-46.

167. Finn, G. J.; Kenealy, E.; Creaven, B. S.; Egan, D. A., In vitro cytotoxic potential and mechanism of action of selected coumarins, using human renal cell lines. *Cancer Letters* **2002,** 183, (1), 61-68.

168. Lacy, A.; O'Kennedy, R., Studies on coumarins and coumarin-related compounds to determine their therapeutic role in the treatment of cancer. *Current Pharmaceutical Design* **2004,** 10, (30), 3797-3811.

169. Liu, S. X. L.; Kapingu, M. C.; Wang, M. S.; Chiou, G. C. Y., Facilitation of retinal function recovery by coumarin derivatives. *Journal of Ocular Pharmacology and Therapeutics* **1997,** 13, (1), 69-79.

170. Fylaktakidou, K. C.; Hadjipavlou-Litina, D. J.; Litinas, K. E.; Nicolaides, D. N., Natural and synthetic coumarin derivatives with anti-inflammatory/antioxidant activities. *Current Pharmaceutical Design* **2004,** 10, (30), 3813-3833.

171. Kulkarni, M. V.; Kulkarni, G. M.; Lin, C. H.; Sun, C. M., Recent advances in coumarins and 1-azacoumarins as versatile biodynamic agents. *Current Medicinal Chemistry* **2006,** 13, (23), 2795-2818.

172. Moriya, T., Excited-state reactions of coumarins in aqueous solutions. 1. The phototautomerization of 7-hydroxycoumarin and its derivative. *Bulletin of the Chemical Society of Japan* **1983,** 56, (1), 6-14.

173. Moriya, T., Excited-state reactions of coumarins. 7. The solvent-dependent fluorescence of 7-hydroxycoumarins *Bulletin of the Chemical Society of Japan* **1988,** 61, (6), 1873-1886.

174. Fink, D. W.; Koehler, W. R., pH effects on fluorescence of umbelliferone. *Analytical Chemistry* **1970,** 42, (9), 990-&.

175. Abueittah, R. H.; Eltawil, B. A. H., The electronic absorption spectra of some coumarins - A molecular orbital treatment. *Canadian Journal of Chemistry-Revue Canadienne De Chimie* **1985,** 63, (6), 1173-1179.

176. Chen, Y.; Chou, C. F., Reversible photodimerization of coumarin derivatives dispersed in poly(vinyl acetate). *Journal of Polymer Science Part a-Polymer Chemistry* **1995,** 33, (16), 2705-2714.

177. Elinos-Baez, C. M.; Leon, F.; Santos, E., Effects of coumarin and 7OH-coumarin on bcl-2 and Bax expression in two human lung cancer cell lines in vitro. *Cell Biology International* **2005,** 29, (8), 703-708.

178. Lopez-Gonzalez, J. S.; Prado-Garcia, H.; Aguilar-Cazares, D.; Molina-Guarneros, J. A.; Morales-Fuentes, J.; Mandoki, J. J., Apoptosis and cell cycle disturbances induced by coumarin and 7-hydroxycoumarin on human lung carcinoma cell lines. *Lung Cancer* **2004,** 43, (3), 275-283.

179. Burlison, J. A.; Avila, C.; Vielhauer, G.; Lubbers, D. J.; Holzbeierlein, J.; Blagg, B. S. J., Development of novobiocin analogues that manifest anti-proliferative activity against several cancer cell lines. *Journal of Organic Chemistry* **2008,** 73, (6), 2130-2137.

180. Jimenez-Orozco, F. A.; Lopez-Gonzalez, J. S.; Nieto-Rodriguez, A.; Velasco-Velaquez, M. A.; Molina-Guarneros, J. A.; Mendoza-Patino, N.; Garcia-Mondragon, M. J.; Elizalde-Galvan, P.; Leon-Cedeno, F.; Mandoki, J. J., Decrease of cyclin D1 in the human lung adenocarcinoma cell line A-427 by 7-hydroxycoumarin. *Lung Cancer* **2001,** 34, (2), 185-194.

181. McNeil, S. E., Nanotechnology for the biologist. *Journal of Leukocyte Biology* **2005,** 78, (3), 585-594.

182. Nuckolls, C.; Hof, F.; Martin, T.; Rebek, J., Chiral microenvironments in self-assembled capsules. *Journal of the American Chemical Society* **1999,** 121, (44), 10281-10285.

183. Park, T.; Zimmerman, S. C.; Nakashima, S., A highly stable quadruply hydrogen-bonded heterocomplex useful for supramolecular polymer blends. *Journal of the American Chemical Society* **2005,** 127, (18), 6520-6521.

184. Zimmerman, S. C.; Corbin, F. S., Heteroaromatic modules for self-assembly using multiple hydrogen bonds. *Molecular Self-Assembly* **2000**, 96, 63-94.

185. Berti, D.; Barbaro, P.; Bucci, I.; Baglioni, P., Molecular recognition through H-bonding in micelles formed by dioctylphosphatidyl nucleosides. *Journal of Physical Chemistry B* **1999,** 103, (23), 4916-4922.

186. Berti, D.; Baglioni, P.; Bonaccio, S.; Barsacchi-Bo, G.; Luisi, P. L., Base complementarity and nucleoside recognition in phosphatidylnucleoside vesicles. *Journal of Physical Chemistry B* **1998,** 102, (1), 303-308.

187. Bombelli, F. B.; Berti, D.; Keiderling, U.; Baglioni, P., Giant polymerlike micelles formed by nucleoside-functionalized lipids. *Journal of Physical Chemistry B* **2002,** 106, (44), 11613-11621.

188. Banchelli, M.; Betti, F.; Berti, D.; Caminati, G.; Bombelli, F. B.; Brown, T.; Wilhelmsson, L. M.; Norden, B.; Baglioni, P., Phospholipid membranes decorated by cholesterol-based oligonucleotides as soft hybrid nanostructures. *Journal of Physical Chemistry B* **2008,** 112, (35), 10942-10952.

189. Bombelli, F. B.; Berti, D.; Pini, F.; Keiderling, U.; Baglioni, P., Flexibility of dilauroyl-phosphatidyl-nucleoside wormlike micelles in aqueous solutions. *Journal of Physical Chemistry B* **2004,** 108, (42), 16427-16434.

190. Campins, N.; Dieudonne, P.; Grinstaff, M. W.; Barthelemy, P., Nanostructured assemblies from nucleotide-based amphiphiles. *New Journal of Chemistry* **2007,** 31, 1928-1934.

191. Baglioni, P.; Berti, D., Self-assembly in micelles combining stacking and H-bonding. *Current Opinion in Colloid & Interface Science* **2003,** 8, (1), 55-61.

192. Aime, C.; Manet, S.; Satoh, T.; Ihara, H.; Park, K. Y.; Godde, F.; Oda, R., Self-assembly of nucleoamphiphiles: Investigating nucleosides effect and the mechanism of micrometric helix formation. *Langmuir* **2007,** 23, (26), 12875-12885.

193. Vernille, J. P.; Kovell, L. C.; Schneider, J. W., Peptide nucleic acid (PNA) amphiphiles: Synthesis, self-assembly, and duplex stability. *Bioconjugate Chemistry* **2004,** 15, (6), 1314-1321.

194. Arigon, J.; Prata, C. A. H.; Grinstaff, M. W.; Barthelemy, P., Nucleic acid complexing glycosyl nucleoside-based amphiphile. *Bioconjugate Chemistry* **2005,** 16, (4), 864-872.

195. Hof, F.; Nuckolls, C.; Rebek, J., Diversity and selection in self-assembled tetrameric capsules. *Journal of the American Chemical Society* **2000,** 122, (17), 4251-4252.

196. Stofer, E.; Chipot, C.; Lavery, R., Free energy calculations of Watson-Crick base pairing in aqueous solution. *Journal of the American Chemical Society* **1999,** 121, (41), 9503-9508.

197. Pranata, J.; Wierschke, S. G.; Jorgensen, W. L., OPLS potential functions for nucleotide bases - Relative associations constants of hydrogen-bonded base-pairs in chloroform. *Journal of the American Chemical Society* **1991,** 113, (8), 2810-2819.

198. Gould, I. R.; Kollman, P. A., Theoretical investigations of the hydrogen-bond srengths in guanine, cytosine, and adenine-thymine base-pairs. *Journal of the American Chemical Society* **1994,** 116, (6), 2493-2499.

199. Yan, X. H.; He, Q.; Wang, K. W.; Duan, L.; Cui, Y.; Li, J. B., Transition of cationic dipeptide nanotubes into vesicles and oligonucleotide delivery. *Angewandte Chemie-International Edition* **2007,** 46, (14), 2431-2434.

200. Bitton, R.; Schmidt, J.; Biesalski, M.; Tu, R.; Tirrell, M.; Bianco-Peled, H., Self-assembly of model DNA-binding peptide amphiphiles. *Langmuir* **2005,** 21, (25), 11888-11895.

201. Marques, B. F.; Schneider, J. W., Sequence-specific binding of DNA to liposomes containing di-alkyl peptide nucleic acid (PNA) amphiphiles. *Langmuir* **2005,** 21, (6), 2488-2494.